Dissertation

submitted to the

Combined Faculty of Natural Sciences and Mathematics

of the Ruperto Carola University Heidelberg, Germany

for the degree of

Doctor of Natural Sciences

Presented by

MSc Anne-Sophie Ernst

born in: Kassel, Germany

Oral examination: 24th of July 2018

Impact of the receptor tyrosine kinase

EphB2 on cerebral ischemia in mice

Referees: Prof. Dr. Markus Hecker

Prof. Dr. Peter Angel

Table of Content

Abbreviations

Abbreviation	
%	percent
°C	degree Celsius
µCT	micro computer tomography
µL	microliter
µM	micromolar
µm	micrometer
AAV	adeno-associated virus
ab	antibody
ADAM	a disintegrin and metalloproteinase
ADC	apparent diffusion coefficient
AF	Alexa Fluor
AMPA	α-amino-3-hydroxy-5-methyl-4-isoxazole propionic acid
ANOVA	analysis of variance
AP	action potential
APS	ammonium persulfate
APV	2-amino-5-phosphonovaleric acid
AraC	cytosine arabinoside
Arf1	ADP-ribosylation factor 1
ATP	adenosine triphosphate
AUC	area under the curve
Aβ	amyoloid beta
BBB	blood-brain barrier
Bcl-2	B-cell lymphoma-2
BDNF	brain-derived neurotrophic factor
bp	base pair
BHS	Blut-Hirn-Schranke
BSA	bovine serum albumin
CA	cornu ammonis
$Ca(CH_3COO)_2$	calcium acetate hydrate
CA1	Cornu Ammonis-1
Ca^{2+}	calcium ion
CA3	Cornu Ammonis-3
$CaCl_2$	Calcium chloride
CaM	calcium/calmodulin
CAM	cell adhesion molecule
cAMP	cyclic adenosine monophosphate
CBF	cerebral blood flow
CCA	common cerebral artery
CD31	cluster of differentiation 31/ PECAM1= Platelet endothelial cell adhesion molecule
cDNA	complementary DNA
c.e.	capillary electrophoresis
cm	centimeter
CNS	central nervous system

CO	carbon monoxide
CO_2	carbon dioxide
CREB	cAMP/calcium response element-binding protein
ctrl	control
DAPI	4',6-diamidino-2-phenylindole
DAPK1	death-associated kinase 1
DEPC	diethyl pyrocarbonate
DFO	deferoxamine
dH_2O	deionized water
DHB	3,4-dihydroxybenzoic acid
DIV	day in vitro
Dlg1	Drosophila disc large tumor suppressor
DM	dissection medium
DMEM	Dulbecco's Modified Eagle Medium
DMOG	dimethyloxalylglycine
DMSO	dimethyl sulfoxide
DNA	deoxyribonucleic acid
dNTP	2´-desoxyribonucleosid-5´-triphosphate
DTT	dithiothreitol
ECA	external carotid artery
ECM	extracellular matrix
EDTA	ethylenediaminetetraacetic acid
EGF	epidermal growth factor
eNOS	endothelial nitric oxide synthase
Eph	erythropoietin-producing human hepatocellular
EPSC	evoked excitatory postsynaptic current
ERK	extracellular regulated MAP kinase
ES	enrichment score
FAK	focal adhesion kinase
Fc	fragment, crystallizable
FCCP	carbonyl cyanide-4-(trifluoromethoxy)phenylhydrazone
FCS	fetal calf serum
FDR	false discovery rate
FGF	fibroblast growth factor
FJC	Fluoro-Jade C
FOV	field of view
FRET	Förster resonance energy transfer
g	gravitational constant
G	Gauge
GABA	γ-Aminobutyric acid
GABAaR	GABAa receptor
GABAR	γ-Aminobutyric acid receptor
GFAP	glial fibrillary acidic protein
GPI	glycosylphosphatidylinositol
Grb4	growth factor receptor-bound protein 4
GSEA	gene set enrichment analysis
GTP	guanosine triphosphate

h	hour
H_2O	water
HBS	HEPES-buffered Saline
HCl	hydrogen chloride
HEPES	4-(2-hydroxyethyl)-1-piperazineethanesulfonic
HIF	hypoxia inducible factor
HO-1	heme oxygenase-1
HRP	horseradish peroxidase
Hz	Hertz
i.v.	intravenous
I/R	ischemia/reperfusion
Iba-1	ionized calcium-binding adapter molecule-1
ICA	internal carotid artery
ICAM	intercellular adhesion molecule 1
ICC	immunocytochemistry
IF	immunofluorescence
IGF-1	insulin-like growth factor 1
IgG	immunoglobulin G
IL-1	Interleukin-1
IL-1β	interleukin-1β
inf	infarct
iNOS	inducible nitric oxide synthase
IP3	inositol trisphosphate
ITS	insulin-transferrin-sodium selenite me-dia supplement
JNK	c-Jun N-terminal kinases
Jun	jun oncogene
K_2SO_4	potassium sulfate
kb	kilo basepairs
kDa	kilodalton
KEGG	Kyoto Encyclopedia of Genes and Genomes
KH_2PO_4	potassium dihydrogen phosphate
Ky/Mg	kynurenic acid/magnesium solution
LTP	long-term potentiation
MAb	murine antibody
MAP	mitogen-activated protein
MAP2	microtubule-associated protein 2
MAPK	mitogen-activated protein kinase
MCAo	middle cererbral artery occlusion
MCP-1	monocyte chemoattractant protein-1
MEM	minimal essential medium
$MgCl_2$	magnesium chloride
MHC	major histocompatibility complex
min	minute
MLC	myosin light chain
mM	millimolar
mm	millimeter
mm^2	square millimeter

MMP	matrix metalloproteinase
MRI	magnetic resonance imaging
mRNA	messenger RNA
MSPR	macrophage-stimulating protein receptor
N	normality/equivalent concentration
n.s.	not significant
N_2O	dinitrogen monoxide, nitrous oxide, laughing gas
Na_2HPO_4	disodium hydrogen phosphate
Na_2SO_4	sodium sulfate
Na_3VO_4	sodium orthovanadate
NaCl	sodium chloride
NADPH	nicotinamide adenine dinucleotide phosphate
$NaHCO_3$	sodium hydrogen carbonate
NaOH	sodium hydroxide
NBQX	2,3-dihydroxy-6-nitro-7-sulfamoyl-benzo[f]quinoxaline-2,3-dione
NCAM	neural cell adhesion molecule
NES	normalized enrichment score
NeuN	neuronal nuclei antigen
NFκB	nuclear factor kappa B
nm	nanometer
NMDA	N-methyl-D-aspartate
NMDAR	N-methyl-D-aspartate receptor
nNOS	neuronal nitric oxide synthase
NO	nitric oxide
NOS	nitric oxide synthase
NP-40	Tergitol-type NP40, nonyl phenoxypolyethoxylethanol
NVU	neurovascular unit
O_2	oxygen
OGD	oxygen glucose deprivation
P	postnatal
p	probability value
PBS	phosphate-buffered saline
PCR	polymerase chain reaction
PDGFR	platelet-derived growth factor receptor
PDL	poly-D-lysin
PDZ	PSD95, post synaptic density protein, Dlg1, zo-1
PECAM	platelet endothelial cell adhesion molecule
PFA	paraformaldehyde
pH	potential of hydrogen
PI3K	phosphatidylinositol-4,5-bisphosphate 3-kinase
PSD95	post-synaptic density protein 95
px	pixel
qPCR	quantitative PCR
rAAV	recombinant adeno-associated virus
rCBF	regional cerebral blood flow
Rh123	Rhodamine 123
RNA	ribonuleic acid

ROCK	Rho-associated protein kinase
ROI	region of interest
ROS	reactive oxygen species
rpm	revolutions per minute
RT	room temperature
RTK	receptor tyrosine kinase
rtPA	recombinant tissue plasminogen activator
s	second
SAM	sterile motif alpha
SD	standard deviation
SEM	standard error of the mean
SGG	salt-glucose-glycone solution
SNARE	soluble N-ethylmaleimide-sensitive factor attachment protein receptor
STAT3	signal transducer and activator of transcription 3
SVZ	subventricular zone
Taq	*Thermus aquaticus*-derived
TBS	tris buffered saline
TBS-T	tris buffered saline with Tween-20
TCA	tricarboxylic acid
TEMED	tetramethylethylenediamine
TGF-β	transforming growth factor β
TM	transfection medium
TNFa	tumor necrosis factor alpha
TrkC	tyrosine-related kinase C
TSA	tyramide signal amplification
TTX	tetrodoxin
U	enzyme unit
USF	upstream stimulatory factor
V	Volt
VCAM1	vascular cell adhesion molecule 1
VEGF	vascular endothelial growth factor
VEGFR	vascular endothelial growth factor receptor
vs.	versus
WT	wild-type
$Zn(CH_3COO)_2 \cdot$	zinc acetate dihydrate
$ZnCl_2$	zinc chloride
ZO-1	zonula occludens-1 protein

Zusammenfassung

Schlaganfälle gehören zu den häufigsten Todesursachen in der westlichen Welt und verursachen in Deutschland jährlich Kosten in Höhe von etwa 6 Milliarden Euro. Etwa 80% aller Schlaganfälle sind ischämische Schlaganfälle und werden meist durch einen Verschluss einer hirnversorgenden Endarterie verursacht. Trotz intensiver Forschungsarbeit sind die molekularen pathophysiologischen Mechanismen des Schlaganfalls nur teilweise aufgeklärt und derzeit ist keine kausale Therapie vorhanden, die die Konsequenzen des ischämischen Insults behandelt.

Die Bluthirnschranke (BHS), eine Struktur bestehend aus Endothelzellen, Astrozyten und Perizyten, trennt das Gehirn von der Peripherie, ermöglicht aber den Einstrom von essentiellen Metaboliten in das Gehirn. Während eines Schlaganfalls werden die Verbindungen zwischen den Endothelzellen degradiert, was eine erhöhte Durchlässigkeit der BHS zur Folge hat und schließlich durch Wassereinstrom ein vasogenes Ödem induziert.

Die durch den Gefäßverschluss bedingte lokale Unterversorgung initiiert eine Folge von Ereignissen, die als ischämische Kaskade bekannt ist. Innerhalb weniger Minuten führen durch Hypoxie und Anoxie ausgelöste Mechanismen zu Exzitotoxizität, ein Prozess bei dem neuronaler Zelltod durch Überstimulation von Glutamatrezeptoren auf Neuronen, wie zum Beispiel den ionotropen NMDA-Rezeptor, hervorgerufen wird. Diese Überstimulation bewirkt einen massiven Ca^{2+}-Einstrom und löst weitere Signalkaskaden aus, wie beispielsweise eine Dysfunktion von Mitochondrien. An der Funktion des NMDA-Rezeptors ist u.a. die Rezeptor-Tyrosin-Kinase EphB2 beteiligt und steuert den Ca^{2+}-Einstrom durch den NMDA-Rezeptor in das Neuron. Das EphB/Ephrin-B-System ist ein Rezeptor-/Liganden-System bei dem sowohl Rezeptor als auch Ligand membranständig sind. Für eine Bindung zwischen Rezeptor und Ligand ist demzufolge direkter Zellkontakt erforderlich. So konnte bereits gezeigt werden, dass EphB2 auf Monozyten mit Ephrin-B-Liganden auf Endothelzellen interagiert und dadurch sowohl eine Transmigration der Monozyten durch die Endothelzellschicht ermöglicht als auch den proinflammatorischen Phänotyp von Endothelzellen beeinflusst.

Aus diesen Gründen war das Ziel dieser Arbeit, den Einfluss von EphB2/Ephrin-B-Liganden während zerebraler Ischämie zu untersuchen.

In *Ephb2*-defizienten Mäusen wurde durch Okklusion der mittleren zerebralen Hirnarterie (MCAo) zerebrale Ischämie erzeugt, die von einer Reperfusionsphase gefolgt war. Analysen von histologischen Färbungen, neurologischen Funktionen und des Transkriptoms ergaben, dass die Schlaganfallauswirkungen nach 12-48 h Reperfusion in *Ephb2*-defizienten Mäusen gegenüber Wildtyp (WT) Mäusen abgeschwächt waren. Wie multiple

Untersuchungen (u.a. CT-Scans, Immunfluoreszenzfärbungen, BHS-Permeabilität-Assays) zeigten, war eine Störung der vaskulären Funktion nicht die Ursache dieser Beobachtung. Weitere Untersuchungen auf Basis von MRT-Scans ergaben jedoch, dass sich in *Ephb2*-defizienten Mäusen innerhalb der ersten 6 h nach Reperfusion ein zytotoxisch bedingtes Ödem geringer ausprägte und auf eine neuronale Ursache hinwies.

Analysen von Hirnlysaten aus WT Mäusen zeigten in diesem Zusammenhang, dass EphB2 nach 6 h Reperfusion in der ischämischen Hemisphäre aktiviert wird (gemessen anhand des Phosphorylierungsstatus). Als nächstes wurde der Einfluss von EphB2 auf die NMDA-Rezeptor-Funktion getestet. Es stellte sich heraus, dass in Ephb2-defizienten Neuronen NMDA-Rezeptor-abhängiger Ca^{2+}-Einstrom in Mitochondrien sowie NMDA-Rezeptor-abhängige mitochondriale Membrandepolarisierung gegenüber WT Neuronen vermindert waren. Da mitochondriale Dysfunktionen ein entscheidendes Merkmal der Schlaganfallpathogenese ist und einen Mechanismus im Rahmen der Induktion von Exzitotoxizität darstellt, wurde eine Zelltodanalyse durchgeführt. Breitgefächerte Exzitotoxizität führte jedoch nicht zu unterschiedlichen Anteilen toter Zellen zwischen WT und *Ephb2*-defizienter Neuronen.

Zusammenfassend zeigt diese Arbeit erstmals, dass EphB2 innerhalb von 6 h nach Schlaganfall aktiviert wird und entscheidend zur zytotoxischen Ödembildung beiträgt, wohingegen die BHS-Permeabilität nicht durch EphB2 verändert wird. Bei Abwesenheit von EphB2 sind die Auswirkungen eines Schlaganfalls wir Infarkt- und Ödemvolumen oder neurologische Defizite abgeschwächt. In *Ephb2*-defizienten Neuronen sind NMDA-Rezeptor-gesteuerte mitochondriale Antworten vermindert, was die Wichtigkeit von EphB2 in Bezug auf die NMDA-Rezeptor-Funktion betont. EphB2-gesteuerte Mechanismen tragen demnach zu Signalprozessen bei, die schließlich zum neuronalen Zelltod führen.

Abstract

Stroke is the number two cause of death in the western world and responsible for about 6 billion euros economic costs caused by illness in Germany annually. Approx. 80% of all strokes are ischemic strokes and often develop from a focal cerebral hypoperfusion caused by an occlusion of a major cerebral artery. Despite intensive research, the pathophysiological and regenerative molecular mechanisms of stroke are only partially understood and no causative therapy dealing with the consequences of the ischemic insult is available.

The blood-brain barrier (BBB) is a structure built up by endothelial cells, astrocytes and perizytes. It separates the brain from the periphery while still allowing essential metabolites to cross. During cerebral ischemia transendothelial connections are degraded and the BBB permeability increases. This eventually causes vasogenic edema formation.

The vessel occlusion-induced local hypoperfusion unleashes a series of events called ischemic cascade. Within minutes, hypoxia- and anoxia-induced intracellular mechanisms lead to excitotoxicity, a process which describes neuronal cell death induction caused by overstimulation of ionotropic glutamate receptors, such as NMDA receptors. Overactivation of NMDA receptors leads to massive Ca^{2+} influx into neurons and triggers signaling cascades, which among others cause mitochondrial dysfunction and eventually cell death. Among others, the receptor tyrosine kinase EphB2 interacts with the NMDA receptor and regulates NMDA receptor functions which lead to increased Ca^{2+} influx through the NMDA receptor in the neuron.

The EphB/ephrin-B system is a receptor/ligand system, in which both, receptor and ligands are membrane-bound requiring direct cell-to-cell contact in order to induce signaling processes. Additionally, it had been shown that interaction of monocytic EphB2 with endothelial ephrin-B ligands influences transendothelial migration and induces a pro-inflammatory phenotype in endothelial cells. Therefore, this study aims to unravel the involvement of EphB2/ephrin-B signaling during cerebral ischemia.

Cerebral ischemia was induced in *Ephb2*-deficient mice by transient middle cerebral artery occlusion (MCAo) followed by different times of reperfusion. Histological, neurofunctional and transcriptome analyses demonstrated that progression of stroke after 12-48 h of reperfusion is attenuated in *Ephb2*-deficient mice as compared to wild-type (WT) mice. However, multiple analyses (CT scans, immunofluorescence staining techniques, BBB permeability assays) showed that this observation was not caused by an impact on vascular function.

On the other hand, further evaluations based on magnetic resonance imaging revealed that cytotoxic edema formation during the first 6 h after reperfusion was diminished in *Ephb2*-deficient mice as compared to WT mice pointing towards a neuronal cause.

In this context, analysis of brain lysates from WT animals revealed that activation (shown by phosphorylation) of EphB2 was increased after 6 h of reperfusion in the ischemic hemisphere. Next, the influence of EphB2 on neuronal NMDA receptor function was investigated. It turned out that NMDA receptor-mediated Ca^{2+} transients and mitochondrial membrane depolarization was decreased in *Ephb2*-deficient neurons as compared to WT neurons. As mitochondrial dysfunction is a hallmark of stroke pathogenesis and a crucial step during induction of excitotoxicity, cell death assays were performed. Widespread exposure to excitotoxic stimuli did not reveal differences in the fraction of dead cells between WT and *Ephb2*-deficient mice though.

Collectively, this is the first study to show that EphB2 is activated within 6 h after stroke and decisively contributes to cytotoxic edema formation while BBB permeability is not influenced by EphB2. In the absence of EphB2, progression of stroke is attenuated with respect to infarct and edema volume as well as neurological function. NMDA receptor-mediated mitochondrial responses are decreased in *Ephb2*-deficient neurons highlighting its importance for the function of the NMDA receptor. Hence, EphB2-dependent mechanisms contribute to signaling events that eventually worsen stroke progression.

1 Introduction

1.1 Cells of the central nervous system

The cells of the vertebrate central nervous system (CNS) can be classified into neurons and glial cells (glia from Greek γλία, "glue"). Nerve cells process and transmit information through the CNS supported by the glial cells, which outnumber the neurons in the brain. Glial cells can be further subdivided into different classes, such as astrocytes, oligodendrocytes, and microglia (Purves and Williams, 2001). Astrocytes, the most abundant glial cells, have several functions, such as modulating synaptic transmission, providing nutrients to the nervous tissue and in maintaining extracellular homeostasis. Additionally, they contribute to the formation of the blood-brain barrier (BBB) (Sofroniew and Vinters, 2010). Oligodendrocytes mainly contribute to the enhancement of signal conduction speed by enwrapping axons with a myelin sheath (Nave, 2010). Microglia are the resident macrophages of the CNS and in addition to their function as immune defense of the CNS, they play a crucial role in maintenance of functional and structural integrity (Aloisi, 2001; Ginhoux *et al*., 2013). Neurons are responsible for receiving, processing and transmission of information through the nervous system (Purves and Williams, 2001).

1.2 Neuronal synapses

The principle steps during neuronal development are proliferation, migration, and differentiation (Jin, 2016; Shimada and Langman, 1970). Among others, the formation of synaptic structures in neurons is crucial in order to establish a functional network of signal transmission. Synapses are contact sites between a neuron and another cell. Between two neurons, contacts usually form between the axon of the signal-passing neuron and a dendrite of the receptive neuron. Though formation of synapses pre-dominantly occurs during embryogenesis and early postnatal life, also in the adult brain new connections are constantly formed and reorganized, for instance during learning and memory formation. The complex process of synaptogenesis comprises structural and cell morphological changes and is mediated by proteins that affect time and place of synapse formation, and further influence stability and specificity of the contact site. Known molecules and proteins include soluble factors as well as membrane-bound molecules (Gerrow, 2006; Waites *et al*., 2005).

Synapses can be subdivided into two major classes: chemical and electrical synapses. At the axon-terminal (presynaptic side) of chemical synapses, highly specialized proteins build up a machinery complex optimized to release neurotransmitters. Those are stored in vesicles located within the presynapse and are released into the synaptic cleft by membrane fusion of the vesicles with the active zone of the presynapse (Purves and Williams, 2001). The fusion process is mediated by proteins of the so-called SNARE complex (Jahn and

Scheller, 2006). Neurotransmitters interact with receptors located on the receptive cell at the postsynapse. Usually, the release of neurotransmitters is triggered by activation of voltage-gated calcium channels due to changes in electrical activity. Changes in electrical activity rise at the axon hill, a specialized site in a neuron, by generation of an action potential (AP), which propagates along the axon and finally depolarizes the axon terminal. Once the released neurotransmitters bind to postsynaptic receptors, the chemical signal originating from an electrical signal, is converted back into an electrical one thereby propagating signal transmission through the whole network. Chemical synapses are further subdivided according to the neurotransmitter they release, e.g. glutamatergic (release of glutamate, interaction with NMDA and AMPA receptors, mainly propagating excitatory signals) or GABAergic (release of GABA, interaction with GABA receptors, mainly propagating inhibitory signals) (Purves and Williams, 2001).

In an electrical synapse, electric currents are transmitted through gap junctions. Gap junctions are built up by specialized protein cluster, which form a pore, and enable direct exchange of electrical impulses as well as ions and small molecules between pre- and postsynaptic cell (Purves and Williams, 2001).

1.2.1 Synaptogenesis

Formation of chemical synapses involves several signaling pathways which regulate the different steps from initiation to stabilization and finally function. First, axons are guided by secreted factors, such as semaphorins or netrins, to their respective target site (Gerrow, 2006; Waites *et al*., 2005). Semaphorins act as inhibitory signal because their signaling induces remodeling of the actin cytoskeleton leading to growth cone collapse of the axon (Meyer *et al*., 2017). Axonal and dendritic maturation is driven by priming factors including fibroblast growth factor (FGF) or Wnts released by neurons or cholesterol and thrombospondin released by glial cells (Waites *et al*., 2005). Wnts interact with the membranous receptor Frizzle and induce remodeling and spreading of growth cones (Lucas and Salinas, 1997). Initial contacts between an axon and a dendrite are mediated by cell adhesion molecules (CAMs) belonging to the family of cadherins and protocadherins. Once adhered, neuroligins and neurexins, as well as EphB receptors and ephrin-B ligands, promote synaptic differentiation by the recruitment of proteins belonging to the presynaptic active zone, the postsynaptic density as well as glutamate receptors. Synaptic maturation primarily comprises morphological changes of the premature synaptic sites. Spine morphogenesis is induced by interaction of cell adhesion proteins regulating small GTPases such as Ras and Rho (Scheiffele, 2003; Waites *et al*., 2005). After recruitment of glutamate receptors, calcium transients can signal into the postsynaptic site and drive gene expression further

modulating growth of dendrites, synapse maturation and finally neuronal plasticity (Greer and Greenberg, 2008).

1.3 Cerebral circulation

Though the human brain makes up only approx. 2-3% of total body weight, it requires 15% of the cardiac output and up to 20% of the energy produced in the whole body (Jain *et al*., 2010). Due to the lack of energy storages, neurons are more vulnerable to changes in oxygen and glucose levels than any other cell which requires a tight regulation of cerebral blood flow (CBF) and extravasation of blood components (Cipolla, 2009).

Three kinds of regulatory mechanisms supposedly contribute to cerebral autoregulation which enables adequate and relatively constant CBF despite changes in the peripheral blood pressure. Firstly, cerebral pressure autoregulation involves endothelial mechanoproperties that respond to shear stress and transmural pressure, and myogenic activity of cerebral vascular smooth muscle cells. Secondly, cerebral metabolism influences CBF, such as release of adenosine, a by-product of neuronal activity that is known to act as a vasodilator. Thirdly, neurogenic regulation is mediated by the functional unit of endothelial cell, astrocytes and perivascular nerves (Paulson *et al*., 1990).

The blood-brain barrier (BBB) is a selective membrane that separates the brain and the circulating blood. Thereby it shields the brain from fluctuations in the composition of the blood or toxins, while still allowing the passage of essential metabolites. The BBB is formed by endothelial cells which are surrounded by a basement membrane, astrocytic endfeet, and pericytes. Together with neurons and the extracellular matrix, they form the so-called neurovascular unit (NVU). Within this unit, each component fulfills individual tasks thereby contributing to the regulation of microvascular permeability, cerebral hemodynamics, nutrient uptake and toxin removal.

The endothelial cells in the BBB are distinct from other endothelial cells as they lack fenestration, have minimal pinocytic activity, low rate of transcytosis and are interconnected by tight junctions, which are a barrier to paracellular diffusion. Tight junctions are formed by transmembranous proteins like claudins and occludins and cytoplasmic adaptor molecules such as Zona occludens 1 (ZO-1). Adherens junctions, which usually are strictly separated from tight junctions, are intermingled with tight junctions in the endothelial cells of the BBB and formed by VE-cadherin and CD31 (PECAM1). The junctional units interact with the actin cytoskeleton enabling rapid morphological changes (Sandoval and Witt, 2008).

The abluminal site od endothelial cells is surrounded by pericytes, which are also involved in the development of the BBB. Further, pericytes are important regulators of microvascular permeability and stability of microvessels as they secrete inhibitory signals which reduce the rate of endothelial transcytosis. The perivascular endfeet of astrocytic glial cells provide

a cellular link to the neurons and express, among others, channels involved in ion and volume regulation. Further, astrocytes secrete a range of molecules with angiogenic characteristics such as angiopoietin 1 or vascular endothelial growth factor (VEGF) thereby influencing and modulating BBB permeability. Structural proteins of the extracellular matrix provide support and anchorage for EC, pericytes, and astrocytes which adhere among others through integrins to the ECM (Sandoval and Witt, 2008).

1.4 Cerebral ischemia

In the year 2015, more than 6 million people died from stroke worldwide and therefore, stroke is considered as the second most common cause of death. Approximately 80% of all strokes are ischemic stroke. Ischemic strokes mostly result from an occlusion of a major cerebral end artery initiating a series of events called ischemic cascade which often develops from a focal cerebral hypoperfusion. Hypoperfusion leads to the first step of the ischemic cascade: depletion of adenosine triphosphate (ATP), the main energy source. Subsequently, energy-dependent ion pumps fail thereby causing depolarization of glial cells and neurons. Voltage-dependent Ca^{2+} channels are activated, excitatory neurotransmitters like glutamate are released and accumulate in the extracellular space as the re-uptake by astrocytes is also impaired. Excessive glutamate leads to overstimulation of *N*-methyl-D-aspartate (NMDA) receptors, α-amino-3-hydroxy-5-methyl-4-isoxazolepropionic acid (AMPA) receptors and kainate receptors which causes massive Ca^{2+} influx into neurons inducing mitochondrial dysfunction. Subsequently, more glutamate is released unleashing the ischemic cascade. Together with Ca^{2+}, water follows passively, thereby causing cytotoxic edema. Ca^{2+}-induced signaling processes lead to formation of reactive oxygen species (ROS) and activation of degradative enzymes (Brouns and De Deyn, 2009).

Both, extrasynaptically and synaptically located NMDA receptors are activated by glutamate inducing Ca^{2+} influx into the postsynaptic cell, which is important for synaptic plasticity and learning but can also induce excitotoxic cell death. Ca^{2+} influx drives gene expression involved in long-term potentiation and depression as well as cell survival. Among others, the transcription factor cAMP-response element-binding protein (CREB) is activated during cerebral ischemia and induces a neuroprotective response through CRE-mediated gene induction (Mabuchi *et al*., 2001). Surviving neurons exposed to ischemia show sustained CREB activation and expression of neurotrophic factors such as brain-derived neurotrophic factor (BDNF). However, activation of extrasynaptic NMDA receptors does not induce expression of BDNF but suppresses CREB activity (Hardingham and Bading, 2010). Further, Ca^{2+} entering through especially extrasynaptic NMDA receptors accumulates largely in mitochondria which finally results in breakdown of the mitochondrial membrane potential, ATP synthesis and formation of ROS (Dugan *et al*., 1995; Hardingham *et al*., 2002; Stanika *et al*.,

2009a). In addition to the localization of NMDA receptor, the composition of subunits of NMDA receptors influences responses to ischemia-induced glutamate excess. NMDA receptors are built up of an essential NR1 subunit encoded by the gene GRIN1, regulatory NR2 (NR2A-D) subunits encoded by GRIN2x genes, and partially an NR3 subunit (GRIN3). Most functional NMDA receptors in the CNS consist of two NR1 subunits, and at least one NR2 subunit, which are in the majority of cases the subunits NR2A and/or NR2B. Together they form a channel pore which only opens if the two agonists glycine and glutamate bind to their binding-sites at the NR1 and NR2 subunit, respectively (Kalia *et al*., 2008b). NR2B-containing NMDA receptors are predominantly located at extrasynaptic sites and NR2B interacts upon ischemia among others with death-associated protein kinase 1 (DAPK1). The NR2B-DAPK1 interaction mediates induction of neuronal cell death (Shu *et al*., 2014; Tu *et al*., 2010). In general, NMDA receptor function depends on phosphorylation at different tyrosine residues within the different subunits. For example, the Src-family tyrosine kinase Fyn phosphorylates Y1472 in NR2B (Nakazawa *et al*., 2001) which contributes to neuronal cell death upon ischemia (Knox and Jiang, 2015).

The dysbalance in ion-homeostasis induces additional signaling cascades, which do not lead to vasodilation but to further hypoperfusion as well as changes in the electrical activity. This together triggers propagation of ischemia, a process called spreading depolarization (Dirnagl *et al*., 1999). Mechanisms inducing cell death comprise caspase-dependent apoptosis as well as caspase-independent processes, such as neuronal necrosis or autophagy-like cell death (Fujikawa, 2015; Sattler and Tymianski, 2001).

Neuronal cell death triggers a secondary, inflammatory response in which both parenchymal cells of the brain (microglia, astrocytes) as well as invading leukocytes (monocytes/macrophages, lymphocytes, dendritic cells) are involved. Interaction of resident microglia, astrocytes and cerebrovascular endothelial cells with dying neurons and further, the ischemic environment induce up-regulation of pro-inflammatory cytokine and chemokine production. Resident microglia in the brain are rapidly activated and release various kinds of cytotoxic mediators, like tumor necrosis factor alpha (TNFa) or interleukin 1β (IL-1β), but also cytoprotective mediators like BDNF or insulin-like growth factor I (IGF-I) (Guruswamy and ElAli, 2017). Additionally, ischemic conditions promote formation of ROS which are also released into the brain parenchyma. Astrocytes can be activated by ROS and subsequently release further cytokines and chemokines. Additionally, expression of inducible nitric oxide synthase (iNOS) is increased. Furthermore, astrocytic glutamate uptake is impaired due to energetic failure triggering excitotoxicity as mentioned above. Peripheral leukocytes adhere to the endothelium within several hours upon stroke, eventually transmigrate through the BBB and contribute to the inflammatory environment in the brain parenchyma. Cytokines induce up-regulation of adhesion molecules in endothelial cells like intercellular adhesion molecule 1

(ICAM-1) or E-selectin (Brouns and De Deyn, 2009). Together with chemokines like monocyte chemoattractant protein 1 (MCP1), peripheral immune cells are recruited and transmigrate through the BBB and finally, migrate into the infarct area (Dirnagl *et al*., 1999; Gelderblom *et al*., 2009).

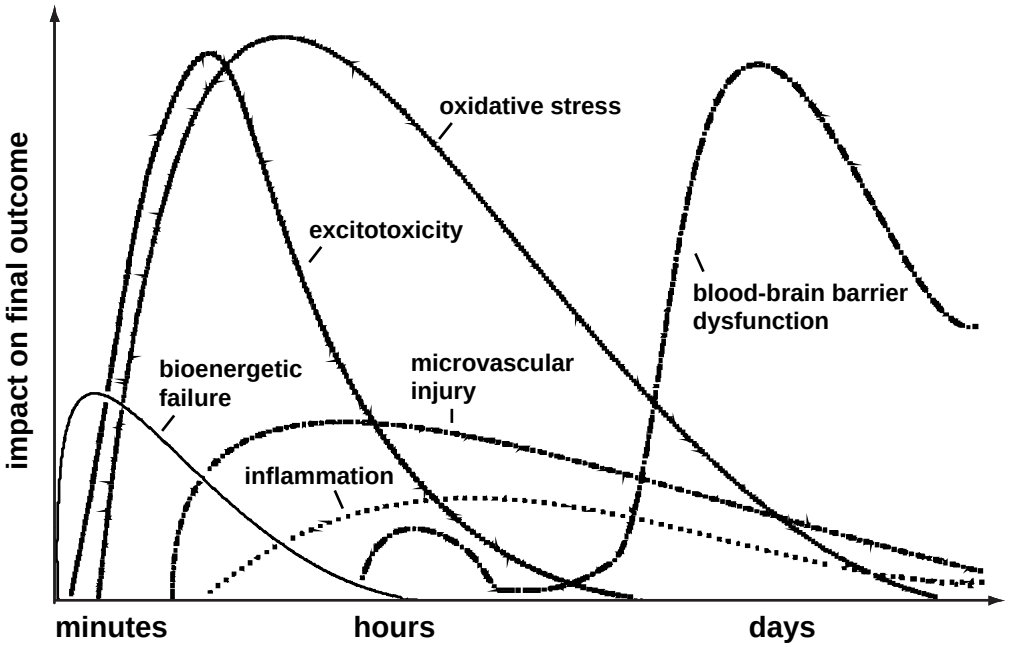

Figure 1: Graph depicting time course of processes in the ischemic cascade and their impact on the final damage. Adapted and modified from Brouns and Deyn (Brouns and De Deyn, 2009).

Importantly, tissue damage upon cerebral ischemia can be divided into two zones: the infarct core and the penumbra. The infarct core is defined by a reduction in cerebral blood flow below 20% which almost immediately triggers the ischemic cascade and necrotic cell death (Dirnagl *et al*., 1999). The collateral arteries in the surrounding tissue of the core region (periinfarct) are still perfused supplying the tissue with oxygen and glucose. However, as blood flow is reduced, this area is defined as the penumbra, a tissue undergoing mild ischemia. Cells within the penumbra are still viable for several hours and can be rescued. Though infarct sizes can be reduced by quick restoration of blood flow, reperfusion conversely contributes to brain injury itself, a process called ischemic reperfusion (I/R) injury, as it increases the risk of cerebral hemorrhage (Nour *et al*., 2013). Figure 1 illustrates the different signaling cascades contributing to tissue damage during and after cerebral ischemia (Figure 1).

1.5 Eph/ephrin system

1.5.1 Classification and structure

Erythropoietin-producing human hepatocellular receptors, short Eph, represent the largest family of receptor tyrosine kinases (RTK). Eph receptors interact with ephrin ligands, which are also membrane-bound, requiring direct cell-to-cell contact in order to induce signaling processes. Eph receptors can be further subdivided into two subclasses based on their binding affinity and similarities of the extracellular sequences (Nomenclature and Ligands, 1997). There are 10 EphA receptors which preferably bind to the GPI-anchored ephrin-A molecules and 6 EphB receptors which preferably bind to transmembranous ephrin-B molecules. While interaction between EphA and ephrin-A often triggers signaling processes in the receptor cell only, interaction of EphB receptors and ephrin-B ligands triggers bidirectional signaling in both cells. The signaling process in the receptor-cell is called forward signaling while in the ligand-bearing cell reverse signaling is induced. The extracellular domain of an Eph receptor includes a ligand-binding globular domain, a cysteine-rich region, and two fibronectin type III repeats. The cytoplasmic part of an Eph receptor consists of 4 different regions, a short juxtamembrane domain with several conserved tyrosine residues, the tyrosine kinase domain, a sterile α motif (SAM) protein-protein interaction domain and a PDZ-binding motif at the C-terminus. Ephrin-A ligands lack a cytoplasmic domain but some of them have been shown to induce downstream-signaling processes by activation of further kinases, possibly by acting as coreceptors or clustering microdomains (Holen *et al*., 2008). In contrast, ephrin-B ligands have a cytoplasmic tail with conserved tyrosine phosphorylation sites and a C-terminal PDZ-binding motif. Receptor and ligand are often expressed on the same cell enabling cis-signaling within the same cell, while interaction between two different cells is called trans-activation. However, cis binding does not trigger signaling processes itself but seems to inhibit the responsiveness of Eph receptors (Pitulescu and Adams, 2010). Figure 2 represents the structure of Eph receptors and ephrin ligands (Figure 2).

Eph receptor-ephrin ligand interaction is disrupted by endocytosis of the Eph/ephrin complex into either the receptor- or the ligand-bearing cell. Noteworthy, surrounding membrane compartments including other proteins such as VEGF receptors are also internalized (Pitulescu and Adams, 2010; Sawamiphak *et al*., 2010; Wang *et al*., 2010). Additionally, the interaction can be eliminated through proteolytic cleavage by gamma-secretases or ADAM family metalloproteases (Klein, 2012; Pitulescu and Adams, 2010).

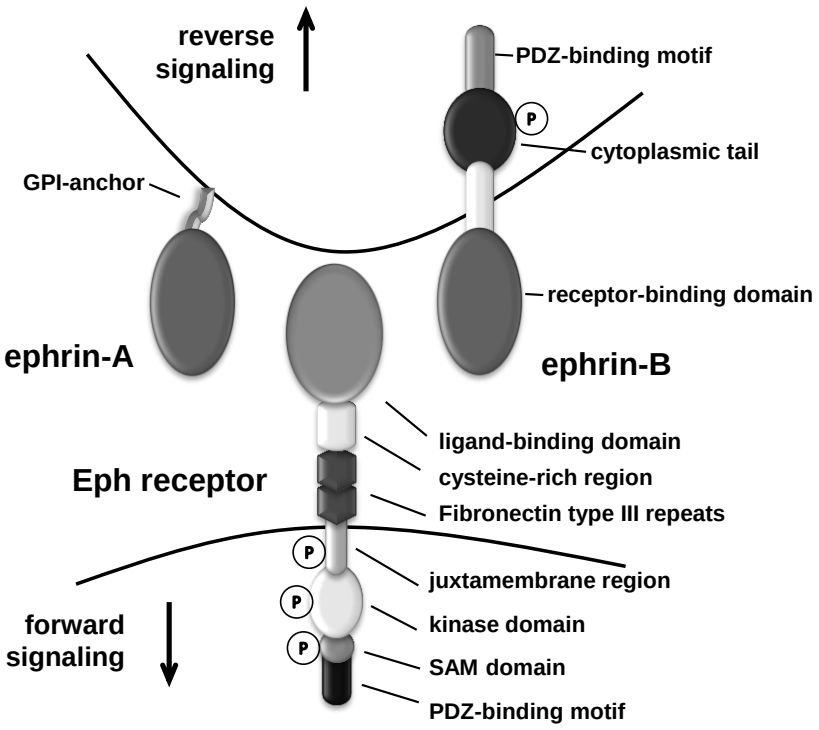

Figure 2: Scheme depicting structural features of Eph receptors and ephrin ligands.

1.5.2 Signaling events

As many different cell types express a plethora of proteins of the Eph/ephrin family, the Eph/ephrin receptor-ligand system controls various biological processes during embryogenesis and adult life by influencing cellular behavior. Eph/ephrin signaling plays an important role during embryogenesis such as vasculogenesis and neurogenesis by induction of attraction and repulsion, attachment and de-attachment, as many signaling processes triggered by this receptor-ligand-system regulate the cytoskeleton.

Eph receptors are activated by phosphorylation upon interaction with ephrin ligands through autophosphorylation at several tyrosine residues and further by Src-family kinases (Lisabeth *et al*., 2013). The phosphorylated kinase domain mostly interacts with SH2 domain-containing proteins such as Rho and Ras or the focal adhesion kinase FAK (Brückner and Klein, 1998).

Similar to Eph receptor activation, ephrin-B ligands are phosphorylated at their cytoplasmic tyrosine residues upon activation. Eph receptor binding induces recruitment and activation of Src family kinases to ephrin clusters which mediate ephrin-B phosphorylation (Palmer *et al*., 2002). The phosphorylated tyrosine residues can then be recognized by SH2-domain proteins, for example, growth-factor-receptor-bound protein 4 (Grb4). Interaction of Grb4 with ephrin-B induces disassembly of stress fibers and increase in FAK activity (Cowan and Henkemeyer, 2001). In addition, ephrin-B ligands can also be (co-)activated by growth

factor receptors such as Tie2 or cell membrane proteins such as claudins (Daar, 2012) and ephrin-B reverse signaling is further involved in Src-, ROCK-, JNK- and PI3K-dependent signaling processes (Bochenek *et al*., 2010; Palmer *et al*., 2002; San Miguel *et al*., 2011; Xu *et al*., 2003).

1.5.3 EphB/ephrin-B in the vascular system

The embryonic development of the (cardio-)vascular system includes initiation of formation of the vascular network (vasculogenesis) and remodeling and expansion processes of such (angiogenesis). The EphB/ephrin-B system plays a crucial role in this process since expression of EphB4 on endothelial cells identifies those as veins while ephrin-B2-positive structures are arteries. Optimal endothelial ephrin-B2 levels are required for proper formation of the capillary network and angiogenesis because ephrin-B2-deficient, as well as ephrin-B2 overexpression in EC, leads to embryonic death. EphB4 Null mice exhibit a similar phenotype like ephrin-B2 deficient mice and die in utero as well (Gerety *et al*., 1999). Ephrin-B2 is also expressed on mural cells. In smooth muscle cells, it is involved in their migration to lymphatic capillaries as well as formation of the microvascular architecture and depletion of ephrin-B2 in mural cells results in perinatal lethality (Foo *et al*., 2006). Other members of the EphB/ephrin-B family are expressed on arteries as well as veins such as ephrin-B1 and EphB3 indicating that EphB/ephrin-B interaction does not solely define arterial and venous boundaries. In addition, interaction of EphB and ephrin-B proteins in the surrounding mesenchymal cells with endothelial cells mediate proper development of vessels since EphB2/EphB3 double mutant mice exhibit vascular defects (Adams *et al*., 1999). Further, ephrin-B1 is expressed on arteries and veins, EphB3 mainly by veins and ephrin-B2 and EphB2 are expressed on mesenchymal cells (Adams *et al*., 1999).

The EphB/ephrin-B system was well-studied during embryogenesis but is also involved in processes during adulthood. In tumors and wounds, sites of neovascularization, expression of ephrin-B2 in endothelial cells is upregulated (Bochenek *et al*., 2010) and participates in angiogenic signaling (Nakayama *et al*., 2013). In a model of ischemia/reperfusion injury, EphB4 and ephrin-B2 were upregulated in endothelial cells in hypoxic skin tissue indicating an involvement of the EphB/ephrin-B system after hypoxic injury (Vihanto *et al*., 2005). Further, VEGF receptor endocytosis depends on ephrin-B2, while ephrin-B2 expression is upregulated by VEGF (Salvucci and Tosato, 2012). However, the EphB/ephrin-B system is better known for its regulatory function during migration of inflammatory cells through the endothelium. Cell culture studies revealed that endothelial ephrin-B1 and -B2 mediates adhesion of monocytes and affects their transmigration through an endothelial monolayer (Korff *et al*., 2008; Liu *et al*., 2014; Pfaff *et al*., 2008). In line with this, monocytes showed upregulation and phosphorylation of EphB2 upon adhesion to endothelial cells and

interaction with ephrin-B2 and release of chemokines (Braun *et al*., 2011). Further, ephrin-B2 interacts with endothelial junctional proteins and increases endothelial cell permeability upon activation by EphB2 possibly through diminishing junctional integrity (Liu *et al*., 2014).

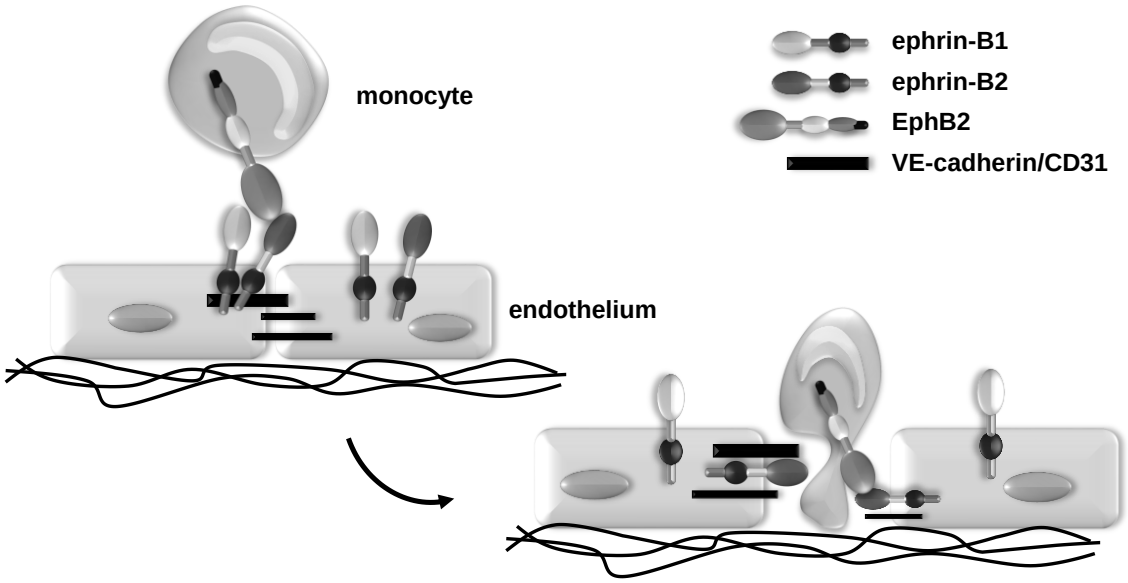

Figure 3: Scheme depicting interaction of monocytic EphB2 and endothelial ephrin-B1/2 during inflammation. Reverse signaling processes in endothelial cells induce disassembly of endothelial junctions thereby increasing endothelial permeability. Subsequently, monocytes are guided through the endothelial monolayer by further interaction of EphB2/ephrin-B2. Scheme according to Liu *et al*. (Liu *et al*., 2014).

Figure 3 represents the proposed mechanism how monocytic EphB2 interacts with endothelial ephrin-B leading to increasing endothelial permeability and transmigration of monocytes through the endothelial monolayer (Figure 3).

1.5.4 EphB/ephrin-B in the nervous system

The EphB/ephrin-B system has been intensively studied for its role in the nervous system. It contributes to the patterning of brain structures, axon guidance, topographic mapping and further to synapse formation and synaptic plasticity. EphB receptors EphB2 and EphB3 and ephrin-B ligands ephrin-B1, -B2 and -B3 support segmentation and boundary formation of anatomic structures during development by complementary expression patterns in the hindbrain. The receptor-ligand interaction induces repulsion thereby stabilizing boundaries and restricting intermingling and movement of cells (Becker *et al*., 1994; Cooke *et al*., 2005). EphB receptors are crucial during axonal guidance and mutations in ephrin-B3 and several EphB receptors result in defects in major brain commissures connecting the two hemispheres. For example, the cytoplasmic domain of EphB2 is essential for proper migration of axons of the posterior tract of the anterior commissure, a lateral axon tract linking the two

temporal lobes (Henkemeyer *et al*., 1996). EphB3 essentially participates in the formation of the corpus callosum, another commissural axon tract connecting the two hemispheres (Orioli *et al*., 1996). Further, EphB/ephrin-B interaction mediates the topographic mapping in the dorsal retina. Forward and reverse signaling processes contribute to guidance of retinal ganglion cell axons (Hindges *et al*., 2002; Thakar *et al*., 2011).

As mentioned previously, the EphB/ephrin-B system contributes to synaptogenesis and spine morphogenesis. Neuronal dendrites form small protrusions referred to as spines, provide the postsynaptic structure of most excitatory synapses. Interaction of EphB2 with ephrin-B triggers presynaptic differentiation (Kayser *et al*., 2006). Direct interaction of the extracellular domain with the NR1 subunit of NMDA receptors induces recruitment of NMDA receptors to Eph receptor clusters (Dalva *et al*., 2000; Nolt *et al*., 2011), while localization of AMPA-type receptors depends on the cytoplasmic domain of EphB2 (Kayser *et al*., 2006). Stimulation of neurons with ephrin-B1 enhances colocalization of EphB2 and NMDA receptors and increases the number of NR1 at presynaptic sites (Dalva *et al*., 2000). Synapse morphology is not altered in *Ephb2*-deficient mutants, however, NR1 synaptic levels are reduced and in EphB1/B2/B3 triple mutants, hippocampal spine density is decreased (Henkemeyer *et al*., 2003). Defects in EphB1/B2/B3 triple mutants can partially be rescued by postnatal induction of EphB2 expression in single neurons in brain slices (Kayser *et al*., 2006). Spine morphogenesis is modulated by EphB receptors through regulation of key regulators of actin dynamics as Rho family GTPases or induction of phosphorylation of syndecan-2, another protein known for regulation of spine morphogenesis (Ethell *et al*., 2001; Irie *et al*., 2005). EphB2 is also involved in NMDA receptor function. Ephrin-B2 activation of EphB receptors enhances NMDA receptor-dependent Ca^{2+} influx by activation of Src family members which subsequently phosphorylates the NMDA receptor subunit NR2B at tyrosine residue 1472. Interestingly, this enhancement is not observed in cells transfected with an EphB2 mutant that cannot bind Src family members. Further, NMDA receptor-mediated Ca^{2+}-influx and gene expression upon glutamate stimulation are enhanced after pretreatment with ephrin-B2 (Takasu, 2002). NMDA receptor subunit localization and amount of NMDA receptors at synapses are regulated by EphB2 (Nolt *et al*., 2011). Functional defects in NDMARs in *Ephb2*-deficient mutants result in a reduction in long-term potentiation and synaptic NMDA receptor-mediated currents (Grunwald *et al*., 2001). Proteins of the EphB/ephrin-B family also mediate interactions between neuronal and non-neuronal cells or between different cell types within the nervous system. During optic nerve injury, macrophages expressing EphB3 seem to interact with damaged axons of retinal ganglion cells thereby modulating axonal re-extension and sprouting (Liu *et al*., 2006). Upon injury, astrocytes play a crucial role in mediating inflammation and tissue repair. Astrocytic ephrin-B1 is upregulated after traumatic brain injury and seems to trigger synapse remodeling through

STAT3 signaling (Nikolakopoulou *et al*., 2016). Noteworthy, inhibition of ephrin-B2/EphB4 signaling between astrocytes and endothelial as well as perivascular cells worsen post-stroke neurovascular repair mechanisms indicating a crucial function in neurovascular homeostasis upon cerebral ischemia (Ghori *et al*., 2017).

Figure 4 summarizes the role of EphB2 and the ligands ephrin-B1/2 during maturation of synapses and synaptic function (Figure 4).

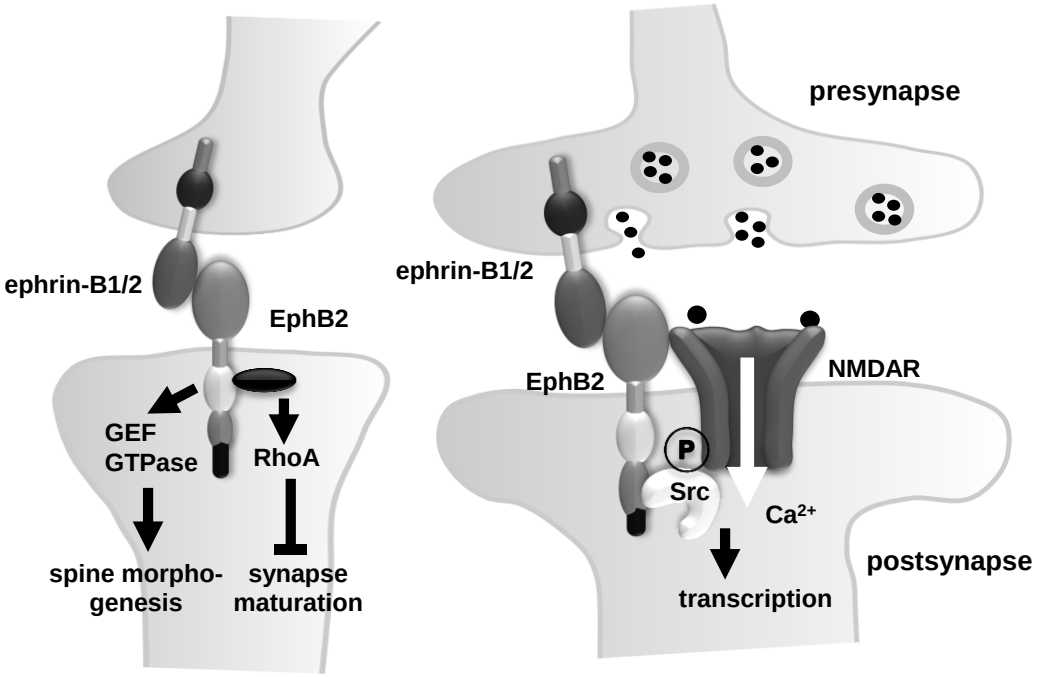

Figure 4: Role of EphB2 and ephrin-B1/2 during synapse formation and synapse function. Left side shows signaling towards remodeling of spines by activating small GTPases, while recruitment of certain adapter molecules leads to activation of RhoA and inhibition of synapse maturation. Right side shows interaction of EphB2 with the NMDA receptor upon binding to ephrin-B and subsequent recruitment of Src family kinases which induces phosphorylation (Ⓟ) of the NMDA receptor. This is followed by Ca^{2+} influx and activation of gene transcription. Black dots: glutamate. Adapted and modified from Dalva 2012 and Sheffler-Collins 2013 (Dalva, 2010; Sheffler-Collins and Dalva, 2012).

1.5.5 The EphB/ephrin-B system in other systems

Apart from the mentioned involvement of the EphB/ephrin-B system in the nervous and vascular system, other biological processes are influenced by EphB receptors and ephrin-B ligands. EphB6 is involved in T-cell responses during experimental autoimmune encephalitis (Luo *et al*., 2004). During arteriosclerosis, a chronic proinflammatory disease during which arterial walls undergo abnormal thickening and hardening, arteriosclerotic plaque formation is possibly influenced by the interaction of endothelial ephrin-B2 with monocytic EphB2. Differentiation of monocytes into macrophages as well as their adhesion to endothelial cells and subsequent upregulation of cytokine gene expression are modified by the abundance of EphB2 and ephrin-B2 (Braun *et al*., 2011).

EphB/ephrin-B binding has been linked to bone formation as the interaction between osteoclasts and osteoblasts through ephrin-B2 and EphB receptors promote osteoclast differentiation while inhibiting osteoblast differentiation and EphB2/B3 or ephrin-B1 mutant mice develop skeletal malformations (Pasquale, 2008).

The EphB/ephrin-B system has also intensively been studied in the context of cancer. Dysregulation of EphB/ephrin-B expression levels has been shown for several cancer entities and can lead to inhibition but also to promotion of cancer progression. Interestingly, in tumor samples derived from human breast cancer patients, particularly high expression levels of cytoplasmic EphB2 were correlated with poor survival (Husa *et al*., 2016). Further, studies showed that EphB2 expression reduces tumor growth by induction of apoptosis in breast cancer cells. Additionally, EphB2 is linked to increased expression of pro-invasive genes like MMP2 or 9 (Chukkapalli *et al*., 2014).

1.6 Rationale and aims of this study

The EphB/ephrin-B system is involved in diverse processes, such as the formation of neuronal synapses, the development of vascular structures, the formation of interendothelial contacts, transendothelial migration, activation of monocytes and function of NMDA receptors – processes which play an important role in the pathogenesis of stroke. However, its role has not been investigated so far in this context of cerebral ischemia. Based on the original results and the functional features of the EphB/Ephrin system, it is assumed that EphB2 and EphB2-mediated signaling processes may i) influence progression of stroke as it possibly ii) modulates the blood-brain barrier (BBB), iii) affects neuronal cell death and iv) modifies the inflammatory responses which may all influence lesion formation upon stroke.

Consequently, the main aims of this project were:

i) Evaluation of infarct and edema sizes as well as motoric impairments upon stroke in *Ephb2*-deficient mice in comparison to WT and further, activation of EphB2 during cerebral ischemia *in vivo*.

ii) Investigation of changes in blood-brain barrier permeability dynamics over time and impact on endothelial junctions in the absence and presence of EphB2 *in vivo*.

iii) Analysis of neuronal cell death and impact of EphB2 on NMDA receptor function in the context of excitotoxicity *in vitro*.

While the project described in this thesis focusses on parts i) - iii), another project part focusing on the involvement and response of the immune system is covered by Laura-Inés Böhler (AG Marti). In accordance with animal welfare, data sets requiring sacrificing of animals were used in this project as well as in the project of Laura-Inés Böhler.

2 Materials

Table 1: Equipment used in this study.

Equipment	Supplier	Model	Application
Camera	Hamamatsu	ORCA flash 4.0	Imaging, Tissue Gnostics system
capillary electrophoresis device	ProteinSimple, Biotechne	Wes	protein separation
Cryostat microtome	Leica Biosystems	Leica CM1520	cryo-sectioning
Digital Imaging System Image Quant	GE Healthcare	LAS 4000 mini	Proteome Profiler
Fluorescence microscope	Zeiss	Axiovert 200M	Imaging, Tissue Gnostics system
Fluorescence microscope	Olympus	IX83	Imaging, CellSense system
Hypoxia working station	Ruskinn	Invivo$_2$ Plus	cell culture, OGD
Laboratory mill	Retsch	Mixermill MM301	Tissue lysis
laser-Doppler flowmetry probe	PeriMed	PROBE 407-1 small straight probe	regional blood flow measurement
multichannel laser Doppler system	PeriMed	PeriFlux 4001 Master	regional blood flow measurement
NanoDrop	Thermo-Fisher Scientific	ND-1000	RNA concentration
Plate reader	Bio-Tek	BioTek Synergy HAT	Evans Blue, Bradford
pump, peristaltic	TSE systems Ismatec	Reglo Analog MS-416	particle perfusion
pump, rate	ASID	Bonz PP50	transcardial perfusion
rotating wheel	UGO Basile S.R.L.	Mouse RotaRod NG	behavioral studies

Table 2: Materials used in animal experiments.

Materials animals	Supplier	Catalogue number	Application
0.9% NaCl	B.Braun Melsungen	3570130	i.v. injection
Bepanthen eye cream	Bayer Vital GmbH		animal surgeries
Adult Mouse Brain Slicer Matrix	Zivic instruments	BSMAS001-1	brain preparation
cannula, 21G	BD Microlance	304432	transcardial perfusion
Clip Applicator Forceps Style	F.S.T. Fine Science Tools	18057-14	animal surgeries, brain dissection

Dumont #5 Fine Forceps	F.S.T. Fine Science Tools	11254-20	animal surgeries, brain dissection
Dumont #7 Fine Forceps	F.S.T. Fine Science Tools	11274-20	animal surgeries, brain dissection
Evans Blue	Sigma Aldrich	E2129	i.v. injection
Graefe Forceps - Curved/Serrated	F.S.T. Fine Science Tools	11051-10	animal surgeries
Mathieu Needle Holder - 14 cm	F.S.T. Fine Science Tools	12010-14	animal surgeries
Micro Serrefine	F.S.T. Fine Science Tools	18055-04	animal surgeries
Ölfarbe Norma® Professional Haut-ton	Schmincke	11220015	particle perfusion
PBS	Sigma Aldrich	D8537	transcardial perfu-sion
PERMA-HAND™ silk suture 3-0	ETHICON	6PA3544 (no longer available)	animal surgeries
RESORBA® silk suture 5-0	RESORBA Medical GmbH	G2105	animal surgeries
silicone rubber-coated monofila-ment for MCAo, 7-0	Doccol Corporation	70191012PK5Re	animal surgeries
Tissue-Tek® O.C.T.TM com-pound	Sakura Finetek	4583	tissue embedding
Vannas Spring Scissors	F.S.T. Fine Science Tools	15000-00	animal surgeries

Table 3: Chemicals and reagents used in this study (without cell culture).

Chemicals and Reagents	Supplier	Catalogue number	Application
10X Sample Buffer	Protein Simple	042-195	c.e.
12-230 kDa Wes Sep-aration Module	Protein Simple	SM-W004	c.e.
5X GoTaq® G2 Flexi buffer	Promega	M891A	genotyping
Anti-Rabbit Detection Module	Protein Simple	DM-001	c.e.
BSA	Sigma Aldrich	A2153	blocking buffer
Capillary Cartridges	Protein Simple	009-050	c.e.
casein	Sigma Aldrich	C5890	blocking buffer
cresyl violet	Merck	1052350025	cresyl violet stain
DAPI	Molecular Probes	D1306	nuclear staining
EnVision+ System-HRP	DAKO	K4002	EphB/ephrin-B staining
Eukitt	Kindler		embedding

Fluoro-Jade C	Chemicon	AG325	FJC staining
goat serum	Dianova	005-000-121	blocking buffer
GoTaq® G2 Flexi DNA polymerase	Promega	M7805	genotyping
Halt™ Protease and Phosphatase Inhibitor Cocktail	Thermo Science Fisher	78442	protein lysis buffer
$KMnO_4$	Merck	1.055082.0250	FJC staining
LowCross buffer	Candor	100125	IF staining
Luminol	Protein Simple	043-311	c.e.
$MgCl_2$, 25 mM	Promega	A351H	genotyping
Mowiol 4-88	Calbiochem	475904	embedding
NonidetTM P 40 sub-stitute (NP-40)	Sigma Aldrich	4385	staining
PCR Nucleotide Mix dNTP	Promega	C114G	genotyping
Peroxide	Protein Simple	043-379	c.e.
Pre-filled microplate	Protein Simple	043-165	c.e.
primer	Eurofins Genomics		genotyping
protease inhibitor cocktail	Sigma Aldrich	P9599	protein lysis buffer
Protein Assay Dye Reagent	Bio-Rad	5000006	Bradford assay
Proteinase K	Thermo Fisher	AM2548	genotyping
Proteome Profiler pRTK	R&D systems	ARY014	protein lysates
RNAse- free DNase	Promega	M6101	genotyping
RNAse-free H_2O			genotyping
RNAsin, 40 U/µL	Promega	N2615	genotyping
RQ1 10X DNase buffer	Promega	M6101	genotyping
saponin	Sigma Aldrich	47036	permeabilization
Standard Pack, Wes	Protein Simple	PS-ST01	c.e.
Streptavidin-HRP	Protein Simple	042-414	c.e.
TRI Reagent	Sigma Aldrich	T9424	RNA isolation
Tris	Roth	4855.2	buffers
TSA Plus Cy5 System	PerkinElmer	NEL745001KT	EphB/ephrin-B staining
Wash Buffer, Wes	Protein Simple	042-202	c.e.
Wes Antibody Diluent II	Protein Simple	042-203	c.e.

Table 4: Primary antibodies used for staining and capillary electrophoresis (Wes).

Antibody	Clonality, host	Supplier	Catalogue number	Dilution	Appli-cation
beta-tubulin	poly, rabbit	Abcam	ab6046	1:500	c.e.
CD31	mono, rat	BD Pharmingen	557355	1:100	IF
desmin	poly, rabbit	Dianova	DLN-13732	1:400	IF
EphB2	poly, goat	R&D systems	AF467	1:2000 1:10	IF c.e.
EphB4	poly, goat	R&D systems	AF446	1:1000	IF
ephrin-B1	poly, goat	R&D systems	AF473	1:4000	IF
ephrin-B2	poly, goat	R&D systems	AF496	1:500	IF
GFAP	poly, rabbit	DAKO	Z0334	1:1000	IF
MAP2	poly, rabbit	Chemicon	ab5622	1:100	IF
NeuN	mono, mouse	Novus Bio-techne	NBP1-92693	1:500	IF
ZO-1	poly, rabbit	Invitrogen	61-7300	1:100	IF

Table 5: Secondary antibodies used for staining and capillary electrophoresis (Wes).

Antibody	Supplier	Catalogue number	Dilution	Application
AF647-donkey-anti-mouse	Dianova	706-606-147	1:100	IF
Cy3-donkey-anti-rabbit	Dianova	711-166-152	1:200	IF
Cy3-goat-anti-rabbit	JacksonImmu-noResearch	111-165-003	1:100	IF
Cy5-donkey-anti-rat	JacksonImmu-noResearch	712-606-150	1:100	IF
FITC-donkey-anti-rat	JacksonImmu-noResearch	712-096-150	1:100	IF
Goat Anti-Rabbit Second-ary HRP Conjugate	R&D systems	042-206	ready-to-use	c.e.
Goat IgG HRP-conjugated Antibody	R&D systems	HAF109	1:50	c.e.

Table 6: Materials and substances used for neuronal cell culture.

Cell culture product	Supplier	Catalogue number
24-well plate	Cellstar	662130
B27 supplement	Invitrogen	17504-044
Bicuculline*	ENZO Life Sciences	ALX-550-515
$CaCl_2x2H_2O$	Merck	1.02382.1000
Cytosine β-D-arabinofuranoside (AraC)	Sigma	C1768
FCCP*	Sigma-Aldrich	C2920
gabazine*	Biotrend	BN 0507
Glucose	Merck	K33069537
Glutamax	Gibco	35050-038
glycine	Fisher Scientific UK	G/0800160
HEPES	Roth	9105.2

Insulin-transferrin-sodium selenite media supplement	Sigma Aldrich	I1884
K_2SO_4 powder	Riedel-de Haën	31270
Kynurenic acid	Sigma Aldrich	K3375-1G
Laminin	Sigma Aldrich	L2020-1MG
L-cystein	Sigma	C7352-25G
MEM, no glutamine	Gibco/Thermo Fisher	21090055
$MgCl_2$ x6 H_2O powder	Merck	5833
Na_2SO_4 powder	Sigma Aldrich	31481-1KG-R
NaCl powder	Sigma	31434-1KG-R
$NaHCO_3$ powder	Riedel-de Haën	31437
NaOH powder	Sigma Aldrich	30620-1KG-R
NBQX*	HelloBio	HB0443
Neurobasal medium	Gibco	21103
nifedipine*	Biotrend	A10643
NMDA*	Biotrend	BN0385
OptiMEM	Invitrogen	31985-054
Papain from papaya latex	Sigma Aldrich	P3125-100MG
PBS	Sigma Aldrich	D8537
PBS with Ca^{2+} and Mg^{2+}	Sigma Aldrich	D8662
Penicillin-Streptomycin (10,000 U/mL)	Gibco	15140122
Phenol red	Sigma Aldrich	P0290-100ML
Poly-D-lysine	Sigma Aldrich	P1149
Rat serum	Bio West	S2150
Rat serum	Abcam	ab7488
Sodium pyruvate solution 100 mM	Sigma Aldrich	S8636-100ML
Sterile syringe filter 0.2 um	Fisher Millipore	SLGP033RS
Trypsin inhibitor	Sigma Aldrich	T9253
TTX*	Biotrend	BN0518
verapamil*	Tocris	0654

*used by Dr Anna Hertle (Bading lab)

2.1 Solution, buffers, media

If necessary, pH values of buffers were adjusted with 10 N or 1 N HCl or NaOH using a pH meter.

Lysis buffer for genotyping

50 mM KCl

1.5 mM $MgCl_2$

10 mM Tris, pH 8.3

0.45% NP-40

0.45% Tween-20

Freshly added: Proteinase K (20 µg/µL), eg. 1 µL to 150 µL lysis buffer

Solution for amplification of DNA for genotyping (volumes in µL)

Solute	Concentration	Volume in µL
primer EphB2-F1	100 nM	0.3
primer EphB2-N1B	100 nM	0.3
primer Neo3	100 nM	0.3
dNTP	10 mM	0.5
$MgCl_2$	25 mM	1.5
5X GoTaq® G2 Flexi buffer	5X	5.0
genomic DNA	from lysis	2.0
GoTaq® G2 Flexi DNA polymerase	5 U/µL	2.0
dH_2O		14.9

Agarose gel for electrophoresis of DNA

1-3% agarose

90 mM Tris

90 mM boric acid

2.5 mM EDTA

0.001% ethidium bromide

PBS, pH 7.6

137 mM NaCl

2.7 mM KCl

10 mM Na_2HPO_4

1.5 mM KH_2PO_4

PBS-T

0.05% Tween-20 in PBS

TBS, pH 7.6

50 mM Tris

150 mM NaCl

TBS-T

0.05% Tween-20 in TBS

Blocking buffer

50 mM Tris, pH 7.6

0.25% casein

0.1% BSA

15 mM NaN_3

Pigment solution

16% Künstlerfarbe Schmincke Norma Professionals Hautton

4% PFA

In PBS

Ringer's solution

154 mM NaCL

5.6 mM KCl

2.4 mM $CaCl_2$

6 mM $NaHCO_3$

5.6 mM dextrose

freshly added: 0.1 mM nitroprusside, 0.1 mM adenosine

PFA in PBS+supplements

20 µM $CaCl_2$

40 mM sucrose

4% PFA

solved in 1XPBS

Zinc-fixative

100 mM Tris, pH 7.4

3.2 mM $Ca(CH_3COO)_2$

22.8 mM $ZnC_4H_6O_4$

36.7 mM $ZnCl_2$

Mowiol

2.4 g Mowiol 4-88 were added to 6 g glycerin and mixed with 6 mL dH_2O for 3 h. Then, 12 mL 200 mM Tris, pH 8.5 were added and the mixture was stirred at 53°C until fully solved. Mowiol was clarified by centrifugation at 5000x*g* for 20 min. Aliquots were made and stored at -20°C.

Lysis buffer Proteome Profiler

Lysis buffer 17 from Array Kit ARY014

Addition of protease inhibitor cocktail according to manufacturer's instruction

2.2 Cell culture

Poly-D-lysine

Solved to a final concentration of 1 mg/mL in sterile H_2O, divided into aliquots and stored at -20°C

Stock solutions, sterilely filtered

1 M NaOH

0.2 M NaOH

1 M HEPES

1 M NaCl

1 M KCl

1 M $NaHCO_3$

2 M $MgCl_2$

1 M Na_2SO_4

0.25 M K_2SO_4

0.1 M $CaCl_2$

2.5 M glucose solution

10 mM glycine

100 mM mannitol

Rat serums purchased from Abcam

Ky/Mg solution

10.5 mM kynurenic acid, 100 mM $MgCl_2$, 50 mM HEPES, 0.5% phenol red, adjusted to slightly acid pH with 1 M NaOH

79.28 mg kynurenic acid

5 mL H_2O

0.2 mL phenol red solution

2.5x 0.2 µL 1 M NaOH

incubated at 37°C for 30 min, mixed in between

after kynurenic acid is in solution

0.2 mL 1 M HEPES

mixed

2 mL 2 M $MgCl_2$

ad 40 mL H_2O

divided into aliquots, stored at -20°C

Dissociation medium

82 mM Na_2SO_4

30 mM K_2SO_4

6 mM $MgCl_2$

0.25 mM $CaCl_2$

1 M HEPES

20 mM glucose

0.2% Phenol red sol

Dissection medium

90% Dissociation medium

10% Ky/Mg solution

addition of 0.2 M NaOH until medium turns slightly purple indicating physiological pH value of approx. 7.5 (eg. 55 µL in 40 mL Dissociation medium)

Enzyme solution

To a solution consisting of 90% Dissociation medium and 10% Ky/Mg solution, L-cystein was added to a final concentration of 3.7 mM. Solutions was adjusted with 0.2 M NaOH and papain is added to a final concentration of 10 U/mL.

45 mL DM

5 mL Ky/Mg solution

22.5 mg L-cystein

300-800 µL 0.2 M NaOH, until phenol red slightly turns purple indicating physiological pH value of approx. 7.5
Mixed
500 units of papain
filtered sterilely once papain is in solution (takes 10-15 min)
divided into aliquots, stored at -20°C

Inhibitor solution
To a solution consisting of 90% Dissociation medium and 10% Ky/Mg solution, 1% trypsin inhibitor was added. Solutions was adjusted with 0.2 M NaOH.
90 mL DM
10 mL Ky/Mg solution
1 g trypsin inhibitor
500-1000 µL 0.2 M NaOH, until phenol red slightly turns purple indicating physiological pH value of approx. 7.5
filtered sterilely once inhibitor is in solution
divided into aliquots, stored at -20°C

Growth medium
1X B27 supplement
0.5 mM Glutamax
100 U/mL Pen/Strep
1% rat serum
solved in Neurobasal A medium

OptiMEM/glucose
20 mM glucose in OptiMEM medium

Salt glucose glycine solution (SGG) (also used as control medium during OGD experiments)
114 mM NaCl
5.29 mM KCl
1 mM $MgCl_2$
26.1 mM $NaHCO_3$
2 mM $CaCl_2$
10 mM HEPES
30 mM glucose

1 mM glycine
0.5 mM Sodium pyruvate solution
0.2% Phenol red solution
sterilely filtered, stored at 4°C

OGD medium

Medium had the same composition as SGG (see above) with the exception that glucose was substituted by equimolar mannitol.

Insulin-transferrin-sodium selenite media supplement ITS

One vial containing ≥21 mg recombinant human insulin; ≥19 mg human transferrin (substantially iron free), and 25 µg sodium selenite was solved in 50 mL acidified sterile water.
1 vial added to 10 mL 10 mM HCl
ad 50 mL sterile H_2O
divided into aliquots, stored at -20°C

Transfection medium TM

88% SGG
10% MEM
1.5% ITS
0.5% Pen/Strep (100 U/mL)

3 Methods

3.1 Animals

All animal experiments were approved by the local animal welfare committee (Regierungspräsidium Karlsruhe, Germany, approval number: 35-9185.81/G-112/13), conformed to the Guide for the Care and Use of Laboratory Animals published by the US National Institutes of Health and were performed in accordance with the recently published Animal Research: Reporting *In vivo* Experiments (ARRIVE) guidelines (http://www.nc3rs.org/ARRIVE). All mice used in the animal experiments were randomized. The surgeon or investigator was blinded to the respective mouse genotypes throughout the experiments and evaluation of the read-out parameters.

Male and female mice were used at the age of 7-9 weeks. For MRI scans, CT scans, RNA isolation, proteome profiler, and Evans Blue injections, only male mice were used.

3.1.1 Maintenance and phenotype of *Ephb2*-deficient mice

All mice were maintained at the animal facility of the University of Heidelberg under specific pathogen-free conditions, a controlled 12:12 h light-dark cycle, constant room temperature (22±2°C) and humidity (40-60%) with food and water *ad libitum*. *Ephb2*$^{-/-}$ (C57BL/6 background) mice were kindly provided by Prof. Dr. Rüdiger Klein (Max Planck Institute of Neurobiology, Munich, Germany). The protein null allele had been created by replacing 1.4 kb of the sequence, which includes the exon that encodes amino acids 29-50, by a neomycin resistance cassette thereby also inducing a frame shift downstream of the mutation (Henkemeyer 1996). EphB2-defcient mice show an abnormal morphology of the anterior commissure pars posterior, a major forebrain commissure that connects the two temporal lobes of the cortex. In addition, *Ephb2*$^{-/-}$ mutants show a hyperactive behavior (Henkemeyer 1996). *Ephb2*$^{+/+}$ mice were either C57BL/6 wild type mice purchased from Jackson Lab or obtained from backcrossing of those wild type mice with *Ephb2*$^{-/-}$ mice. *Ephb2*$^{+/-}$ mice were derived from intercrossing of *Ephb2*$^{+/+}$ and *Ephb2*$^{-/-}$ mice.

3.1.2 Genotyping

Tissue was lysed in 200-300 µL lysis buffer and incubated overnight at 55°C. Lysates were incubated for 5 min at 95°C and centrifuged at 100xg for 5 min. Supernatant contained genomic DNA. DNA lysate was mixed with nucleotide mix, $MgCl_2$, and Taq polymerase. Primer (Table 7) were added and the target gene was amplified based on the following program: 94°C, 5 min; 35x (94°C, 15 s; 61°C, 40 s; 72°C, 90 s); 72°C, 10 min.

Then, the amplificon was applied to agarose gel electrophoresis. DNA was visualized by staining with ethidium bromide. Samples of *Ephb2*$^{+/+}$ animals showed an amplificon with a size of approximately 450 bp, *Ephb2*$^{-/-}$ tissue one of 300 bp.

Table 7: Primer sequences used for genotyping of animals used in this study

Primer name	**Sequence**
EphB2 (F1), start exon 2, forward	5´-AAA CCC TGA TGG ACT CTA CGA CAG C-3´
EphB2 (N1B), intron 2, reverse	5´-GTC AGT TTC ATA GCC TGA AGA ACG-3´
Neo transgene (Neo3), reverse	5'-GGG TAC ATC TCA GTG GTA GAA TG-3´

3.1.3 Middle cerebral artery occlusion

Middle cerebral artery occlusion (MCAo) was done as described before (Barteczek *et al*., 2017). In brief, mice were anesthetized for induction and maintenance by inhalation of a mixture containing 2.5-3.0% and 1.5% isoflurane, respectively, 70% N_2O and remainder O_2 using a vaporizer. Body temperature was maintained at 37°C with a feedback-controlled heating pad. A midline neck incision was made and the left common carotid artery as well as its bifurcation internal carotid artery (ICA) were isolated and dissected from surrounding tissue. Then, a 7-0 silicon rubber-coated monofilament (Doccol Corporation) was induced into the left CCA and pushed through the ICA towards the middle cerebral artery. The incision was closed, and the intraluminal suture was left for 60 minutes. Animals were anesthetized, and the filament was withdrawn to allow reperfusion. For sham surgery, the filament was inserted and withdrawn immediately. During MCAo and 30 min after start of reperfusion, mice were kept under observation under a heating lamp at 30°C. Then, mice were placed in a heating cabinet at 30°C. If reperfusion time was longer than 24 h, mice were placed in a normal cabinet the next day. Mice received softened food pellets and easily accessible drinking bottles.

3.1.4 Laser Doppler flowmetry

Laser Doppler flowmetry was don as described before (Kunze *et al*., 2015; Li *et al*., 2016; Reischl *et al*., 2014). To measure regional cerebral blood flow (rCBF) reduction, a laser-Doppler probe (Perimed Instruments) was positioned 1.5 mm posterior and 3 mm lateral to Bregma on the left side of the exposed skull. RCBF was measured right before and immediately after induction of MCAo.

3.1.5 Magnetic resonance imaging

Magnetic resonance imaging (MRI) was performed at the division of Neuroradiology at the University Hospital Heidelberg (Prof. Dr. Martin Bendszus) by Dr. Angelika Hoffmann and Manuel Fischer. Animals were anesthetized for induction and maintenance by inhalation of

2% and 1-11.5% isofluorane, respectively, in air. Animals were fixed in a prone position in an animal holder equipped with a tooth bar and headlock to reduce head motion. Body temperature was maintained at 37°C using a feedback-controlled water bath and an in-house developed program in LabView (National Instruments Corporation) was used to externally monitor respiration. Animals were scanned on a small animal scanner at 9.4 Tesla magnetic field strength (BioSpec 94/20 USR, Bruker) using a volume coil for RF transmission and a 4-channel-phased-array surface receiver coil.

MRI included different imaging set-ups as described before (Kunze *et al*., 2015): T2-weighted imaging ((TE_{eff}/TR = 66 ms/2650 ms, RARE factor = 8, slice thickness 0.5 mm, 13 slices matrix 256 × 256, in plane resolution 78 µm × 78 µm), diffusion-weighted imaging TE_{eff}/TR = 20 ms/3400 ms, slice thickness = 0.7 mm, 30 diffusion sensitized directions with a b-value of 1500 s/mm^2, field-of-view 12 × 15 mm, matrix 96 × 128, resolution = 125 µm × 117 µm), diffusion-weighted imaging TE_{eff}/TR = 20 ms/3400 ms, slice thickness = 0.7 mm, 30 diffusion sensitized directions with a b-value of 1500 s/mm^2, field-of-view 12 × 15 mm, matrix 96 × 128, resolution = 125 µm × 117 µm), and quantitative T2 measurements (TE increments of 8 ms from 8 ms to 136 ms, TR = 3100 ms, slice thickness = 0.5 mm, matrix = 172 × 172, resolution = 116 µm × 116 µm).

The real signal component from the Multislice Multiple Spin Echo data were fitted after phase correction and SNR optimized multiple coils signal combination on a voxel-by-voxel basis with the monoexponential function $M_0 * e^{-(TE/T2)}$ using a nonlinear least-squares fit procedure (MATLAB Release 2012b, The MathWorks, Inc.).

Diffusion-weighted images by FSL's (FMRIB [The Oxford Centre for Functional Magnetic Resonance Imaging of the Brain] Software Library) FDT toolbox (http://www.fmrib.ox.ac.uk/fsl/fdt/index.html) were utilized to obtain apparent diffusion coefficient (ADC) values. Images were analyzed with the software Amira (Visage Imaging, Inc.). Manual region growing was performed by using a threshold-based pre-segmentation to determine the ischemic lesion on ADC and T2 maps in basal ganglia (including striatum) and cortex.

3.1.6 CT scan

Computer tomographic (CT) scans were performed at the Division of Medical Physics in Radiology, DKFZ, by Dr. Dorde Komljenovic.

Right before µCT imaging, 100 µl ExiTron™ nano CT contrast agent (Miltenyi Biotec, Bergisch Gladbach, Germany) were injected via the tail vein. Mice were anesthetized by inhalation anesthesia (3.5% Sevoflurane in room air) during µCT imaging and scanned with an Inveon scanner (Siemens Medical Solutions, Erlangen, Germany) with following parameters: 500 µA, 60kV, exposure time 600 ms, binning 1, rotation steps 720 RS, total rotation

360°, magnification Med-high, pixel size 30 µm. Images were obtained using OsiriX DICOM viewer (Bernex, Switzerland) with the identical parameters for both mice.

3.1.7 Evaluation of neurological impairments after MCAo

Motoric skills were assessed by using the Rotarod test. Mice were trained to run on a rotating wheel on 3 days with 3 runs each for 300 s with a linear increase from 5-40 rpm. On the day of the MCAo and the day afterward, mice were set on the wheel and time was measured until they fell off.

In addition, neurological function was determined using the modified Bederson neurological deficit score before MCAo and at the end of the reperfusion time. The following scoring system was used:

Score 0	No observable deficit
Score 1	Forelimb flexion
Score 2	Decreased resistance to lateral push
Score 3	Unidirectional circling
Score 4	No movement

3.1.8 Visualization and analysis of brain vessels

Mice were sacrificed by CO_2 asphyxiation. Immediately after the onset of death, thorax cavity was opened, the right atrium was incised leading to venous outflow, while a perfusion cannula (25G) was inserted into the left ventricle. Mice were perfused with approximately 20 mL pre-warmed (37°C) Ringer's solution containing vessel dilators through a peristaltic pump until blood was completely washed out. Then, perfusion was continued with approximately 10 mL of a pre-warmed pigment solution. Mice were decapitated and skulls were fixed overnight in 4% PFA in PBS with supplements at 4°C. The next day, brains were removed from skulls, placed in fresh PFA solutions for additional 3 h and images were taken under a dissecting microscope. Vessels and bifurcation supplying the area of the middle cerebral artery were manually counted.

3.1.9 Tissue processing

For histochemical, immunofluorescence staining, brain lysates for proteome profiler, capillary electrophoresis and RNA analysis, mice were transcardially perfused. Mice were anesthetized with a mixture 3.0% isoflurane, 70% N_2O and remainder O_2 using a vaporizer. Thorax cavity was opened and a perfusion cannula (21G) was inserted into the left ventricle. The right atrium was incised and mice were perfused with PBS (RT) at a rate of 2 mL/min with a total volume of 10 mL, except for tissue harvest for proteome profiler and analysis

with simple western; here, cold PBS and a total volume of 8 mL was used. Subsequently, brains were carefully removed from the skull and processed for further analysis.
For histochemical and immunofluorescence staining brains were harvested after 12, 24 or 48 h of reperfusion and were embedded into Tissue-Tek (Sakura Finetek) and stored at -80°C until usage.
For isolation of RNA (48 h of reperfusion) and analysis of extravasation of Evans Blue (12 and 24 h of reperfusion), olfactory bulbs and cerebellum were removed, hemispheres were separated, quickly frozen in liquid nitrogen, and stored at -80°C until further usage.
For proteome profiler and capillary electrophoresis analysis (6 h of reperfusion), brains were harvested with pre-cooled instruments on ice. Brains were then placed into a pre-cooled brain slicer. Brains were aligned to the sliding groove according to their lambdoid and sagittal sutures. Two pre-cooled razor blades were set around relative to Bregma 0.00±0.5 mm and Bregma 2.50±0.5 mm with a total distance of 3 mm. This thick brain slice was separated into its hemispheres and quickly frozen in liquid nitrogen. Tissue was stored at -80°C until further usage.

3.1.10 Evans Blue injection and quantification

2 h prior to the end of the reperfusion time, mice were anesthetized and 100 µL of a pre-warmed (37°C) solution containing 2% Evans Blue (Sigma-Aldrich) in 0.9% NaCl were injected into the tail vein through a syringe, which was subsequently flushed with 50-100 µL of a 0.9% NaCl solution to ensure full injection of the Evans Blue solution. Mice were kept under a heating lamp at 30°C for 2 h. Then, mice were transcardially perfused and brains were harvested as described above. For detection of extravasated Evans Blue, 500 µL ice-cold 50% trichloroacetic acid (TCA) was added per hemisphere. Tissue was lysed with a grinding ball at 30 Hz for 2 min (Mixer Mill MM301, Retsch). Lysates were incubated for 2 h at 4°C and centrifuged at 16,000xg for 15 min at 4°C. The supernatant was used for quantification. A serial dilution of Evans Blue in 50% TCA was made (1:2 series, starting from 40 µg/mL to 0.625 µg/mL). Technical triplicates were pipetted into a 96-well and absorption was measured at 620 nm with a plate reader (Synergy HT, BioTek).

3.1.11 RNA isolation from brain tissue and purification

RNA was isolated according to manufactures instruction. In brief, 500 µL cold TRI Reagent (Sigma-Aldrich) (4°C) was added per hemisphere. Tissue was lysed with a grinding ball at 1 Hz for 1 min (Mixer Mill MM301, Retsch). Then, 1 mL TRI Reagent was added and the lysates were allowed to stand for 5 min at RT. 200 µL chloroform per 1 mL Tri Reagent was added, samples were shaken vigorously for 15 s, and allowed to stand for 2-15 min at RT. The resulting mixture was centrifuged at 12,000x*g* for 15 minutes at 4 °C. Centrifugation

separated the mixture into 3 phases: a red organic phase (containing protein), an interphase (containing DNA), and a colorless upper aqueous phase (containing RNA). The aqueous phase was transferred to a new tube, 0.5 mL of 2-propanol per mL TRI Reagent used in sample preparation was added and mixed by inverting the tube 15-20 times. Samples were allowed to stand at RT for 5-10 min and centrifuged at 16,100x*g* for 10 min at 4°C allowing the RNA to precipitate as a pellet on the side and bottom of the tube. The supernatant was decanted, and the pellet was washed twice by addition of 1 mL 75% ethanol per 1 mL TRI Reagent, centrifugation at 16,100x*g* for 5 min at 4°C and decanting of the supernatant. Then, remaining ethanol was completely removed, the pellet was briefly dried and finally dissolved in 30 µL RNAse-free H_2O. RNA concentration was measured by a NanoDrop (ND-1000, peqlab). 30 µg of isolated RNA was filled up to a final volume of 39 µL with RNase-free H_2O and the following agents were added: 5 µL RQ1 10X DNAse buffer, 3 µL RNAsin (40 U/µL), and 3 µL RNAse-free DNAse (all Promega). After 30 min incubation at 37°C, 100 µL TRI Reagent was added, and the sample was processed as above. The resulting RNA pellet was dissolved in 20 µL RNAse-free H_2O and stored at -80°C until further usage.

3.1.12 Gene expression profiling

Microarray analysis was performed at the Centre for medical research (ZMF) at the medical faculty Mannheim by Dr. Carsten Sticht.

High quality of RNA was confirmed by capillary electrophoresis on an Agilent 2100 bioanalyzer (Agilent). Arrays of mouse MoGene-2_0-st-type from Affymetrix were used to perform gene expression profiling. GeneChip® WT Plus Reagent Kit and the GeneChip® Hybridization, Wash and Stain Kit (both from Affymetrix, Santa Clara, USA) were applied according to manufacturer's instruction to prepare biotinylated antisense cRNA. After hybridization on the chip on a GeneChip Hybridization oven 640, it was dyed in the GeneChip Fluidics Station 450 and finally scanned with a GeneChip Scanner 3000. All of the equipment used was from the Affymetrix-Company (Affymetrix, High Wycombe, UK).

Arrays were annotated using a Custom CDF Version 20 with ENTREZ based gene definitions (Dai *et al* 2005). Quantile normalization and RMA background correction were used to normalize the raw fluorescence intensity. A commercial software package SAS JMP10 Genomics, version 7, from SAS (SAS Institute, Cary, NC, USA) was used to identify differentially expressed genes by calculating an ANOVA. The level of significance was set to a false positive rate of a=0.05 with FDR correction. Presence of a statistically significant bias in the distribution of defined lists (or sets) of genes within a ranked gene list was tested with Gene Set Enrichment Analysis (GSEA; Subramanian *et al*). Pathways belonging to various cellular processes such as cell cycle or apoptosis were obtained from a public external database (KEGG, http://www.genome.jp/kegg).

3.1.13 Cryo-sectioning

Brains embedded in Tissue-Tek were adapted to the optimal cutting temperature at approximately -15°C in a Cryo-stat (Leica CM1520, Leica Biosystems). Coronal sections were cut at 10 µm thickness and mounted directly on polysine-coated microscope slides. For analysis of infarct and edema sizes, 24 coronal sections at a distance of 0.4 mm were collected and submitted to Nissl staining (see below). For immunofluorescence and Fluoro-Jade C staining, sections from +0.62 to -0.62 mm relative to Bregma were collected. Sections were briefly dried on a heating plate (37°C) and stored at -20°C until further usage. Regions were identified using the atlas *The Mouse Brain in Stereotaxic Coordinated* by Paxinos and Franklin.

3.1.14 Cresyl violet staining and measurement of infarct and edema sizes

All steps were performed at RT if not stated otherwise. Cresyl violet staining and calculation of infarct and edema sizes were done as described before (Reischl *et al*., 2014). In brief, cryosections were air-dried for 20 min. Then, sections were placed into a descending ethanol series: 15 min 96% ethanol, 1 min 70% ethanol, 1 min 50% ethanol. Sections were placed twice into dH_2O for 2 and 1 min, respectively. Subsequently, sections were placed into an acetic cresyl violet solution (0.5% cresyl violet in 1% glacial acetic acid) at 60°C for 10 min. Afterwards, sections were rinsed several times with dH_2O and air-dried. The dye in the cresyl violet solutions stains RNA bluish violet thereby labeling healthy tissue, while damaged tissue appears light (cresyl violet-deficient) as shown in Figure 5. Stained sections were scanned and the sizes of both hemispheres, as well as the cresyl violet-deficient area which corresponds the infarct area, were measured by utilizing ImageJ. To calculate the infarct area of each section the following equation was applied: inf = (cresyl-def + total contra - total ipsi), with inf = infarct area in mm^2, cresyl-def= cresyl violet-deficient area in mm^2, total contra= total area of the contralateral hemisphere in mm^2, total ipsi = total area of the ipsilateral hemisphere in mm^2. The total infarct volume was calculated as the summation of the total infarct area of each section multiplied by the distance between each section, which was 0.4 mm: infarct volume in mm^3 = ∑inf (mm^2) *0.4 mm. This equation includes a correction for the increase in the volume of the ipsilateral hemisphere due to vasogenic edema-induced swelling. In line with this, the edema volume was calculated according to the following equation: edema volume (mm^3) = ∑ (total ipsi (mm^2) - total contra (mm^2)) *0.4 mm.

3.1.15 Fluoro-Jade C staining and counting of dead neurons

This method was adapted from that originally described by Schmued *et al*. (Schmued and Hopkins, 2000) and the manufacture's instruction (Chemicon).

All steps were performed at RT if not stated otherwise. 10 µm cryo-sections were air-dried for 10 min and fixed with 4% PFA in PBS for 15 min at RT. Then, slices were briefly immersed in dH_2O and dried on a slide warmer at 50°C for at least 30 min. Slices were rehydrated and permeabilized by immersion in basic ethanol consisting of 1% NaOH in 80% ethanol for 5 min followed by 2 min in 70% ethanol and dH_2O, respectively. Fluorescent background was blocked and contrast was optimized by immersing slices in 0.06% $KMnO_4$ for 5 min on a rocking table followed by rinsing slices in dH_2O for 2 min. Finally, slices were incubated in 0.0001% Fluoro-Jade C in 0.01% acetic acid including 1 µg/mL DAPI for 20 min in the dark. Then, slices were rinsed 3 times for 1 min in dH_2O and placed on a slide warmer at 50°C until completely dry. After immersing slides in xylene for 1 min, slices were mounted with Eukitt (Kindler) and stored at RT in the dark until usage.

Fluorescence staining was recorded using a Zeiss Axiovert 200M microscope with a Hamamatsu ORCA flash 4.0 camera by applying TissueFAXS scanning software. Nuclei were identified by DAPI-staining. Number of cells showing fluorescent signal for Fluoro-Jade C was automatically counted by using TissueGnostics software. The anatomic structure of Caudate putamen was defined as striatum. The region of the cerebral cortex except was defined as shown in Figure 5.

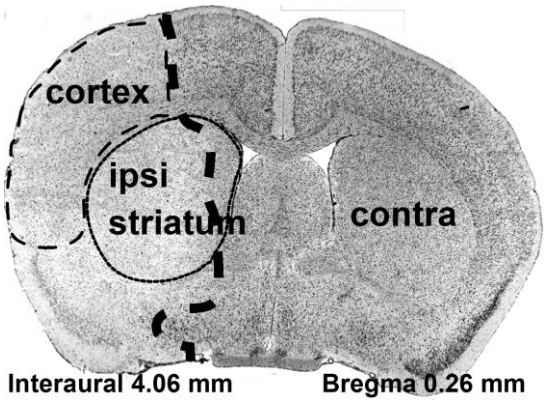

Figure 5: Image of sagittal brain section Nissl-stained with cresyl-violet. The right side is the contralateral, normoxic hemisphere. The left side is the ipsilateral, ischemic hemisphere. Infarct area is bright while viable tissue is darker. Bold dotted line indicates border of infarct. Dotted Thin dotted line labels the area referred as cortex, continuous line labels striatum.

3.1.16 Immunofluorescence staining of brain slices

All steps were performed at RT if not stated differentially. Details regarding antibodies and dilutions can be found in the material section at p 22.

For immunofluorescent staining, all coronal cryo-sections (10 µm in thickness) were fixed with zinc-based fixative (in mM: 100 Tris (pH 7.4), 3 $Ca(C_2H_3O_2)_2$, 25 $Zn(C_2H_3O_2)_2$ and 35 $ZnCl_2$) for 30 min. Then, slices were immersed in ddH_2O for 5 min.

Staining for EphB and ephrin-B proteins and vessels: Activity of endogenous peroxidase was blocked by incubation with 0.3% H_2O_2 in methanol for 10 min. Slices were immersed 3 times in ddH_2O for 3 min each. Subsequently, slices were incubated for 30-60 min with blocking buffer (0.1% BSA, 0.25% casein in 50 mM Tris) followed by incubation with overnight at 4°C with the primary antibody. Next day, slices were washed 3 times in TBS-T for 5 min. Slices were incubated for 30 min with a peroxidase-conjugated EnVision (DAKO, Agilent) reagent followed by incubation with a Tyramide Signal Amplification (Perkin Elmer) reagent for 1 min. When stained with antibodies against EphB-receptors, slices were incubated with blocking buffer again followed by incubation with an antibody against CD31 overnight at 4°C. Next day, slices were washed as before and incubated with an appropriate secondary antibody for 1 h.

Staining for tight junctions and vessels: Slices were immersed 3 times in PBS for 5 min. Then, slices were permeabilized with 0.5% saponin in PBS for 10 min followed by 5 min in PBS and incubation with blocking buffer (10% goat serum in PBS-T) for 30 min. Subsequently, slices were incubated overnight at 4°C with the primary antibodies targeting for the tight junctional protein ZO-1. The next day, slices were washed 3 times with PBS-T for 5 min followed by incubation with appropriate secondary antibodies for 1 h.

Staining for pericytes and vessels: Slices were incubated for 30 min with blocking buffer consisting of 0.1% BSA and 0.25% casein in 50 mM Tris followed by incubation with overnight at 4°C with the primary antibodies targeting for the endothelial cell adhesion molecule CD31 and desmin, a protein found in muscle cells and pericytes. Next day, slices were washed 3 times in TBS-T for 5 min followed incubation with appropriate secondary antibodies for 1 h.

Nuclei were counterstained with DAPI (1 µg/mL in PBS, 3 min). All antibodies were diluted in LowCross-Buffer (Candor). Stained sections were then embedded in Mowiol mounting medium (Polysciences) and stored at 4°C until imaging within 3 days. Fluorescence staining was recorded using a Zeiss Axiovert 200M microscope with a Hamamatsu ORCA flash 4.0 camera.

3.1.17 Analysis of vessels and pericyte-coverage of vessels

To quantify the density of brain vessels, areas with CD31-specific fluorescence intensity were assigned as vessels. Areas, which were associated with desmin-specific fluorescence intensity was defined as an area of a vessel covered by a pericyte. A macro for Image J was used to quantify number of vessels and pericyte-coverage automatically. The macro was designed by Dr. Holger Lorenz, Imaging Faculty, Centre of Molecular Biology (ZMBH), Heidelberg University.

3.1.18 Phospho-RTK Proteome Profiler

Phosphorylation levels of receptor tyrosine kinases (RTK) was analysed using Proteome Profiler Mouse Phospho-RTK Array Kit (R&D systems). Array was used according to manufacturer's instruction with minor modification. Briefly, lysis buffer was prepared according to manual, with the exception that a protease and phosphatase inhibitor cocktail (see list of materials) was used. To each thick brain slice 500 µL lysis buffer was added and tissue was lysed with a grinding ball at 30 Hz for 2 min (Mixer Mill MM301, Retsch). Lysates were incubated on ice for 10 min on a rocking table and centrifuged for 5 min at 16,100x*g* at 4°C. The supernatant was transferred into a new tube and protein concentration was determined utilizing Bradford assay (Bio-Rad Protein Assay Dye, Bio-Rad). Protein-concentration matched tissue lysates (250 µg total protein) were diluted with array buffer and applied to nitrocellulose membranes spotted with capture and control antibodies in duplicates and incubated overnight at 4°C on a rocking table. Membranes were washed to remove unbound proteins followed by incubation with an anti-phospho-tyrosine-HRP detection antibody for 2 h at RT. After washing, phosphorylated tyrosine residues in activated receptors were detected by chemiluminescence using Image Quant LAS 4000 mini machine (GE Healthcare). The signal produced by each sport was quantified using Image QuantTL (GE Healthcare) software. The signal of a PBS-spot served as control spot and was used as background subtraction. Changes in phosphorylation levels of RTK were calculated as the ratio of the ipsi- and contralateral hemisphere of the same animal. Tissue of the contra- and ipsilateral hemisphere of one animal was applied to membranes of the same batch of an array kit to exclude variations within spot densities between batches.

To ensure induction of cerebral ischemia-related processes, only animals were included which showed an increase in the ratio of the phosphorylation level in the ipsilateral hemisphere of more than 1.2 of at least 5 out of 7 RTKs, which were MSPR, PDGFRα, PDGFRβ, TrkC, VEGFR1, 2, and 3, indicating an adequate and prototypic ischemic response of the tissue at that time point. (see results Figure 21).

3.1.19 Capillary electrophoresis

Protein levels of EphB2 in lysates used for the Proteome Profiler Array were detected by capillary electrophoresis. Capillary electrophoresis (Wes, Protein Simple, Biotechne) was used according to manufacturer's instructions. Samples were diluted to a final concentration of 0.5 µg/µL. Protein lysates were diluted with 0.1X sample buffer to a final concentration of 0.5 µg/µL and mixed with 5X Fluorescence master mix according to manufacturer's instruction. Samples were denaturated for 5 min at 95°C, spun for 1 min at 1000x*g*, thoroughly mixed, and spun for 1 min at 100x*g*. Antibodies were diluted in Antibody diluent. Volumes of diluents were applied to the microplate according to manufacturer's instruction with

modification: biotinylated ladder, 5 µL; prepared sample, 5 µL; Wes Antibody Diluent 2, 10 µL; primary antibody, 9 µL; streptavidin-HRP, 10 µL; secondary HRP conjugate, 9 µL; Luminol-Peroxidase Mix, 15 µL.

The following setup was used: separation time, 30 min; separation voltage, 375 V; antibody diluent time, 5 min; primary antibody time, 30 min; secondary antibody time, 30min. Images were automatically analyzed with Compass for SW software. Luminescence was calculated as the area under the curve at a specific exposure time (EphB2, 32 s; beta-tubulin, 1 s). Protein levels of EphB2 were normalized to those of beta-tubulin.

3.2 Primary cortical cultures

3.2.1 Coating of culture wells or cover slips for maintenance of neuronal cells

Wells were covered with poly-D-lysine (2 µg/cm²) and laminin (1 µg/cm²) diluted in sterile H_2O (for a well of a 24-well plate 500 µL were used) for at least 24 h at 37°C, then washed twice with sterile H_2O (1 mL per well in a 24-well plate) and stored at 37°C until usage within 1 week.

3.2.2 Dissection and maintenance

Primary forebrain neuron cultures were established according to Bading *et al* (Bading and Greenberg, 1991; Bading *et al*., 1993) with modification. 4-6 neonatal mice were decapitated and brains were removed from skull and further processed in dissection medium on a cooling device under a binocular microscope. Hemispheres were separated, meninges, midbrain, and hippocampus were removed, the cerebral cortices were isolated and collected in dissection medium on ice. Further steps were performed under a laminar flow. Dissection medium was removed and cortices were incubated with 2 times 3 mL enzyme solution at 37°C with careful swirling in between. Then, cortices were carefully washed with dissection medium (RT) and incubated 3 times with 2 mL inhibitor solution at 37°C. Cortices were carefully washed 3 times with 2 mL pre-warmed growth medium (37°C) for 1 min while turning the tube consistently by hand for 1 min. Subsequently, 2 mL pre-warmed growth medium (37°C) was added and cortices were triturated with a 2-mL serological pipette by pipetting up and down for 50 times. 2 mL growth medium were added and cells were allowed to stand for 5 min at 37°C. As much as possible of the cell suspension was transported to a new tube without any cell clusters. The remaining suspension was triturated as before. Finally, cell suspension was triturated a third time with higher pressure to dissolve remaining cell clusters. Cell density was determined using a Neubauer counting chamber. Cells were diluted in OptiMEM/glucose medium at a density of 125,000 cells/cm² and seeded onto previously coated 24-well plates (poly-D-lysine (2 µg/cm²) and laminin (1 µg/cm²) diluted in sterile H_2O for at least 24 h at 37°C, then washed twice with sterile H_2O and stored at 37°C

until usage within 1 week). Wells were never let get dry and solutions were replaced immediately. After 2.5 h, medium was set to growth medium. Day of plating = day *in vitro* (DIV) 0. To inhibit glial cell growth, AraC was added in a final concentration of 2.8 µM on DIV 3. On DIV 8 cells were set to so-called transfection medium TM. Experiments were performed on DIV 10, when neurons express functional glutamate receptors and have developed an extensive network of synaptic contacts.

All mediums applied to the cells were pre-equilibrated in the respective incubators for at least 16 h.

3.2.3 Recombinant adeno-associated viruses (rAAVs).

The corresponding experiments were done in collaboration with Dr. Anna M Hertle (group of Prof Hilmar Bading, Dep of Neurobiology, Heidelberg University). Viral particles were produced and purified as described previously (Zhang *et al.*, 2007). Expression of the mitochondrially targeted, FRET-based Ca^{2+} indicator 4mtD3cpv was driven by a viral vector containing a CKIIα promoter. Cells were infected more than 6 h after addition of cytosine-D-arabinofuranoside (DIV3-4) by applying approx. 10^{11} rAAV particles per mL.

3.2.4 Fluorescence imaging

The corresponding experiments were done in collaboration with Dr. Anna M Hertle. All imaging experiments were performed RT in a HEPES-buffered saline solution (HBS) containing, in mM: 140 NaCl, 2.5 KCl, 1.0 $MgCl_2$, 2.0 $CaCl_2$, 10 HEPES, 1.0 glycine, 35.6 D-glucose, and 0.5 $C_3H_3NaO_3$. Mitochondrial membrane potential and Ca^{2+} levels and were analyzed as described previously (Hardingham *et al.*, 2002; Palmer & Tsien, 2006; Qiu *et al.*, 2013) using the FRET-based, mitochondrially targeted Ca^{2+} indicator, 4mtD3cpv, and the small molecule dye, Rh123, respectively. Cytoplasmic calcium levels were determined using the small molecule dye, Fura-2. Fluorescence images were taken with the following setup: upright fluorescence microscope (BX51W1, Olympus), cooled CCD camera at 0.667-2.0 Hz (iXon, Andor), 20X water-immersion objective (XLMPlanFluor, Olympus), xenon arc lamp with an excitation filter wheel (cell^R, Olympus), excitation filters (4mtD3cpv: CFP 430±12 nm, YFP 500±10 nm; Fura-2: 340±10 nm and 380±10 nm; Rh123: 470±20 nm; AHF Analysentechnik), emission filters (Fura-2: 510±20 nm; Rh123: 525±25 nm; 4mtD3cpv: 470±12 nm and 535±15 nm; AHF Analysentechnik), DualView beam splitter (for 4mtD3cpv; MAG Biosystems).

Images were acquired using cell^R software (Olympus) and further analyzed with Fiji (RRID:SCR_02283) and IgorPro (WaveMetrics, RRID:000325).

Crosstalk- and bleaching-corrected 4mtD3cpv FRET ratios were used to quantify changes in mitochondrial calcium concentrations in regions of interest drawn around single neurons

(Palmer and Tsien, 2006). Cells grown on coverslips were loaded with Rh123 (Invitrogen, Cat # R302; 4.3 µM) in HBS for 30 min at RT and then extensively washed with HBS. After recording, cells were exposed to the mitochondrial uncoupler FCCP (5 µM, Sigma Aldrich) to induce maximal Rh123 signal. Detection area of Rh123 fluorescence was limited to the nucleus to avoid dequenching artefacts emerging from mitochondria. Fluorescence levels were quantified in a cell-by-cell fashion as a% of the maximum Rh123 signal induced by FCCP in that cell representing changes in mitochondrial membrane potentials (Ψ_m). Fluorescence intensities of Fura-2-AM was determined to quantify cytoplasmic calcium levels. Cells grown on coverslips were loaded with Fura-2-AM (Molecular Probes, Cat # F1221; 1 µM; stock solution, 1 mM in 20% Pluronic F-127 (Sigma-Aldrich, Cat # P2443) in DMSO) in HBS for 30 min at 37 °C and then extensively washed with HBS. Cytoplasmic calcium concentrations were quantified in regions of interest drawn around single neurons. Then, the ratio of emission intensities obtained by sequential excitation with 340±10 nm and 380±10 nm light (340/380 ratio) was determined.

3.2.5 Excitotoxic stimulation

The corresponding experiments were done in collaboration with Dr. Anna M Hertle. Cells were stimulated with Bicuculline (50 µM; negative control) or NMDA (0, 5, 10, 20, or 30 µM) for 10 minutes, carefully washed two times with TM, and incubated in fresh TM for a further 16–24 hours prior to fixation.

3.2.6 Oxygen glucose deprivation (OGD)

Cells grown in 24-well plates were carefully washed once with medium lacking glucose, which was pre-equilibrated in a hypoxic chamber with 1% O_2 for at least 16 h and incubated with the same medium for 3 h. Control cells received the same medium with glucose equilibrated to standard oxygen levels (~19% O_2). After 3 h, cells were either directly fixed or washed once with TM and incubated for another 24 h with TM at in a normal cell culture incubator.

3.2.7 Cell death analysis (excitotoxic stimulation)

The corresponding experiments were done in collaboration with Dr. Anna M Hertle. Cells were fixed with Roti-Histofix 4% (Carl Roth, Cat # P087) for 15 min RT, washed with PBS, and embedded with Mowiol 4-88 mounting medium (Calbiochem) containing 2 µg/mL Hoechst 33258 (Serva, Cat # 15090). In each well, 16 evenly distributed fields of view were acquired. Images were taken at the Nikon Imaging Center at the University of Heidelberg (Ti2 Eclipse inverted microscope (Nikon), Sola SE II Light Engine (Lumencor), S Plan Fluor 20x objective (NA 0.45; Nikon), and a DS-Qi2 14-bit CCD camera (Nikon), 393±11.5 nm

excitation, 447±30 nm emission; Nikon). Images were processed with CellProfiler Software by applying custom pipelines to identify nuclei. Amorphous or shrunken nuclei were classified as dead cells as described previously (Dick and Bading, 2010) and automatically classified using CellProfiler Analyst software.

3.2.8 Cell death analysis (OGD)

Cells were washed twice with pre-warmed (37°C) PBS and fixed with 4% PFA and 4% sucrose in PBS for 15 min at RT. Cells were washed 3 times with PBS-T for 5 min and incubated with 2 µg/mL Hoechst 33258 in PBS for 15 min at RT. After washing twice with PBS for 3 min at RT, cells were mounted with Mowiol medium. Images were taken the next day with a Zeiss Axiovert 200M microscope with a Hamamatsu ORCA flash 4.0 camera. Wells were scanned using TissueFACS software and 11 evenly distributed fields of view of each well were examined. Dead cells were identified as above.

3.2.9 Assessment of neuronal cell culture quality

All steps were performed at RT if not stated otherwise. Purity of cell cultures was tested via immunofluorescence staining on DIV10 with a nuclear marker specific for neuronal cells (NeuN) and a marker specific for astrocytes (GFAP). Cells grown in a 24-well plate were washed twice with pre-warmed PBS (37°C) and fixed with 2% PFA in PBS for 15 min. Then, cells were washed 3 times with PBS for 5 min and permeabilized with 0.5% saponin in PBS for 10 min. After washing twice with PBS for 3 min, cells were incubated with blocking buffer consisting of 0.1% BSA and 0.25% casein in 50 mM Tris followed by incubation with the primary antibodies overnight at 4°C. Next day, cells were washed 3 times in TBS-T for 5 min followed incubation with appropriate secondary antibodies for 1 h. Nuclei were counter stained with DAPI. All antibodies were diluted in LowCross-Buffer. Stained cells were then embedded in Mowiol mounting medium and stored at 4°C until imaging within 3 days. Fluorescence staining was recorded using an Olympus IX51 microscope and a high-resolution camera (Olympus). 10 evenly distributed fields of view of each preparation were imaged. Nuclei were identified by DAPI-staining. Number of cells showing NeuN-specific fluorescent signal were identified as neurons, cells showing GFAP-specific fluorescent signal were identified as astrocytes. Shrunken nuclei showing high fluorescent intensity of DAPI-staining were considered as dead and excluded from quantification. Automatic analysis was performed utilizing TissueGnostics software. Approximately 84% cells were identified as neurons (Figure 6).

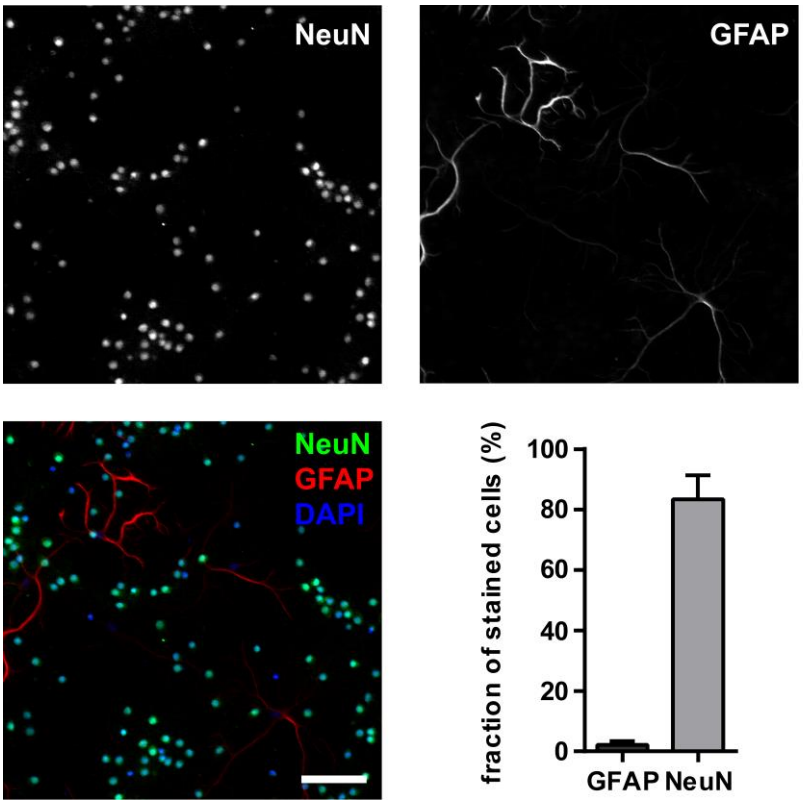

Figure 6: Neuronal purity in cell cultures. Cortical neuron cultures were co-stained at DIV10 with the neuron-specific marker NeuN and the astrocytic-specific marker GFAP. At least 10 evenly distributed FOV of 5 different preparations (both genotypes) were automatically counted. Upper line shows single channel images of primary antibody staining, lower panel shows merged image and quantification. Scale bar= 100 µm.

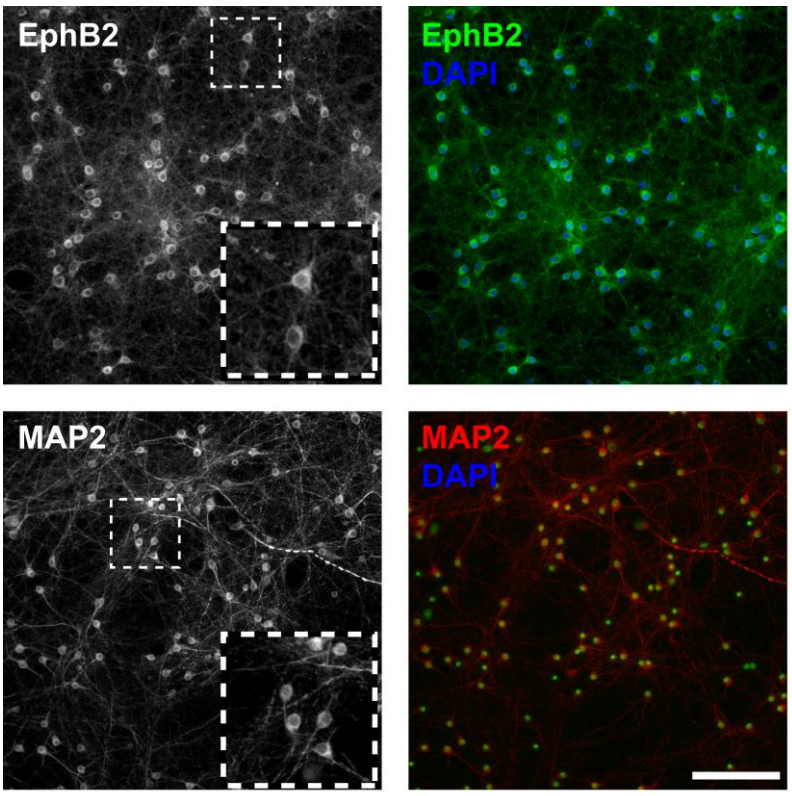

Figure 7: Expression of EphB2 in cultured neurons. Cortical neurons were cultured until DIV10 and single-staining with the neuron-specific marker MAP2 and an antibody targeted against EphB2 was performed. Upper panel shows staining with EphB2, lower panel indicates neuronal structures by MAP2. Small squares are enlarged in the lower right corner of each single-channel image showing neuronal-typical structures. Scale bar=100 µm.

3.2.10 Analysis of expression EphB2 in neuronal cell cultures

Synthesis of EphB2 was analyzed by performing immunofluorescence staining as described above (p 37). Wells with cells from the same preparation were immunofluorescently stained for the neuronal marker MAP2. Cells were fixed with zinc-based fixative, permeabilized with saponin, and incubated with the primary and appropriate secondary antibody as described above (p 22). Nuclei were counterstained with DAPI (1 µg/mL in PBS, 10 min). All antibodies were diluted in LowCross-Buffer (Candor). Stained cells were then embedded in Mowiol mounting medium (Polysciences) and stored at 4°C until imaging within 3 days. Fluorescence staining was recorded using a Zeiss Axiovert 200M microscope with a Hamamatsu ORCA flash 4.0 camera. Cortical neurons synthesize EphB2 at DIV10 (Figure 7).

3.3 Statistics

Data were analyzed using GraphPad Prism 6. Each set of data was tested for normal distribution. If data were normally distributed, data were tested for outliers by using Grubbs' test for outliers. Outliers were removed from the data set. Parametric data sets were tested with unpaired, two-sided Student's *t*-test or Welch's *t*-test (two groups) or one-way ANOVA (more than two groups). Non-parametric data sets were analyzed with Mann-Whitney (two groups) test or Kruskal-Wallis test (more than two groups). Multiple comparisons were performed with two-way ANOVA. Tests were post-corrected with Dunn’s (one-way ANOVA, Kruskal-Wallis test) or Holm-Sidak method (two-way ANOVA). Data are presented as the mean ± standard deviation (SD) if not stated otherwise. Statistical significances are expressed as *p*-values with $p<0.05$ considered as statistically significant difference.

4 Results

4.1 Analysis of progression of stroke in *Ephb2*-deficient mice

To evaluate the role of the receptor tyrosine kinase Eph receptor B2 (EphB2) during stroke, cerebral ischemia was induced by transient middle cerebral artery occlusion (MCAo) for 60 min in animals without mutations in the *Ephb2* gene (described as *Ephb2*$^{+/+}$), *Ephb2*-deficient (*Ephb2*$^{-/-}$) and heterozygous mutant mice (*Ephb2*$^{+/-}$, 24 h of reperfusion only) followed by 48 or 24 h of reperfusion.

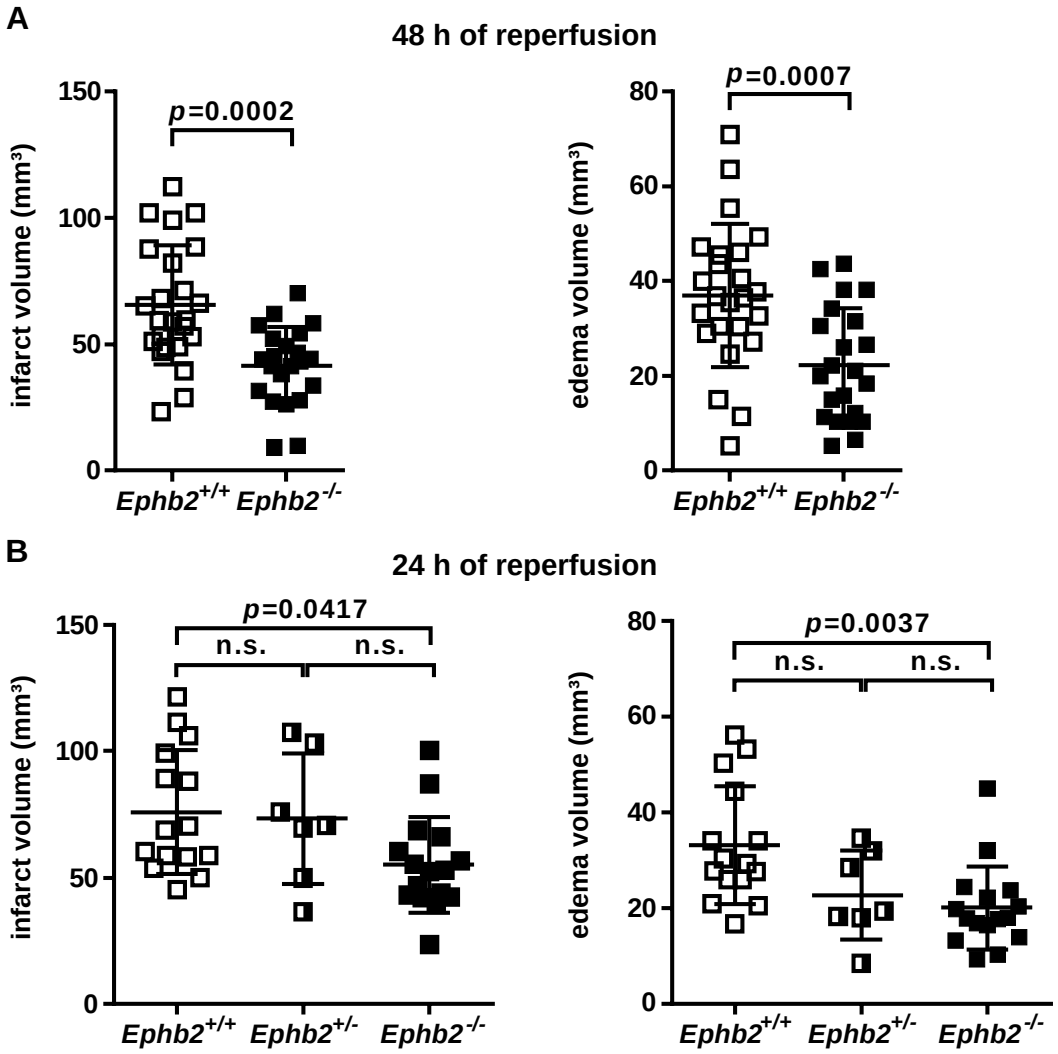

Figure 8: Infarct and edema sizes are reduced in EphB2-defcient mice. *Ephb2*$^{+/+}$, *Ephb2*$^{-/-}$ and *Ephb2*$^{+/-}$ (only 24 h) mice were subjected to 60 min middle cerebral artery occlusion (MCAo) followed by 48 **(A)** or 24 h **(B)** of reperfusion as indicated. Sagittal brain cryo-sections were Nissl-stained and infarct and edema sizes were analyzed using ImageJ. Infarct volume is edema-corrected. Data are presented as single values (scatter plots) combined with the mean±SD; (A) N=24/22, Student's *t*-test, (B) N=15/17/16, One-way ANOVA, n.s.=not significant

After 48 h post the onset of reperfusion, infarct and edema sizes of *Ephb2*$^{+/+}$ and *Ephb2*-deficient mice were evaluated by measurement of cresyl violet-deficient area in Nissl-stained brain sections. *Ephb2*-deficient mice showed a reduction in infarct size of approx. 37% and in edema size of approx. 40% in comparison to *Ephb2*$^{+/+}$ animals (Figure 8A). For the analysis after 24 h of reperfusion, *Ephb2*$^{+/-}$ animals were included to determine a possible gene-dose effect (Figure 8B). *Ephb2*-deficient mice showed reduced infarct and edema sizes of approx. 28% and 40%, respectively, in comparison to *Ephb2*$^{+/+}$ animals. Heterozygous mutants showed a reduction in edema size of 31%, though not significant, while infarct size was similar to *Ephb2*$^{+/+}$ animals (Figure 8B).

Further, neurofunctional deficits were assessed. Animals were assigned a score according to the Bederson scale (details are described on p33), a readily practicable test since it does not require any pre-training of the animals and allows to determine basic neurological deficits. *Ephb2*-deficient animals were less functionally impaired in comparison to *Ephb2*$^{+/+}$ animals after 48 h of reperfusion (Figure 9A). However, after 24 h of reperfusion, no difference was observed for *Ephb2*-deficient and EphB2 heterozygous animals, when compared to *Ephb2*$^{+/+}$ animals (Figure 9B).

In addition, motor coordination was tested. Motoric skills were assessed by utilizing the so-called RotaRod test, which has a high sensitivity to detect motor impairments in ischemic models (Schaar 2010). *Ephb2*-deficient and heterozygous animals showed significantly less impairment in motoric skills in comparison to *Ephb2*$^{+/+}$ animals. Further, the impairment in motoric skills was comparable in *Ephb2*-deficient and heterozygous mutants (Figure 9C).

Taken together, the absence of EphB2 attenuated progression of stroke with a possible gene-dose effect on neurological function and infarct sizes.

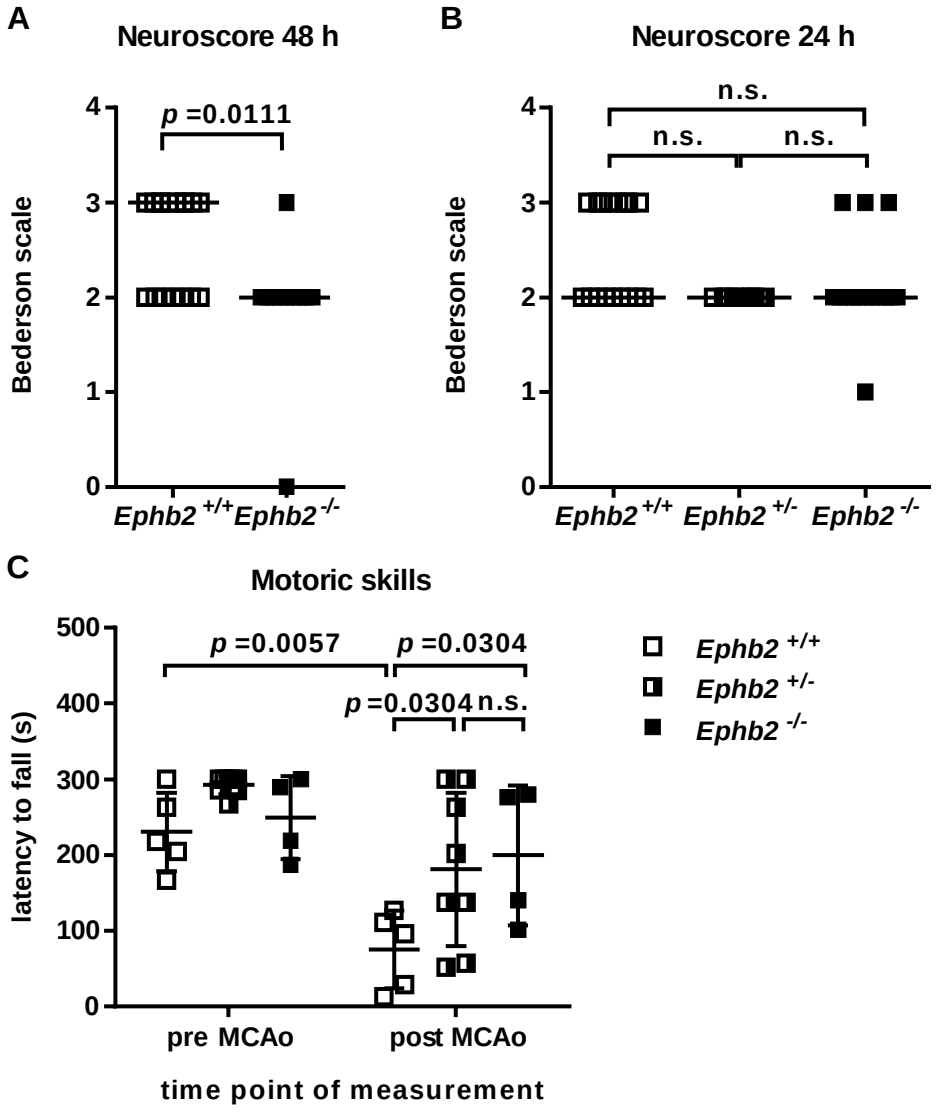

Figure 9: Neurological impairment is reduced in *Ephb2*-deficient mice. Experiments with *Ephb2*$^{+/+}$, *Ephb2*$^{-/-}$ and *Ephb2*$^{+/-}$ ((B)+(C)) mice were performed as described in Figure 8. **(A)** and **(B)** Neurological deficit score was determined according to the Bederson scale. Data are presented as single values (scatter plots) combined with the median; (A) N=17/11, (B) N=17/8/15, Kruskal-Wallis test. **(C)** Motoric skills were tested using the Rotarod test before middle cerebral artery occlusion (MCAo) and the day afterwards (>16 h of reperfusion). Data are presented as single values (scatter plots) combined with the mean±SD; N=5/8/4, Two-way ANOVA, n.s.=not significant.

To analyze the molecular background of the different progression of stroke in greater detail, transcriptome analyses of brain lysates of *Ephb2*$^{-/-}$ and *Ephb2*$^{+/+}$ animals were compared. Animals were subjected to MCAo followed by 48 h of reperfusion and brain hemispheres were separated into an ischemic (ipsilateral) and normoxic (contralateral) hemisphere. The samples were then analyzed by DNA microarray and subsequent gene set enrichment analysis (GSEA). For GSEA, the KEGG database was utilized to identify gene sets clustered in signaling pathways.

The comparison of the transcriptomes of the ischemic and normoxic hemispheres of *Ephb2*$^{+/+}$ animals revealed an upregulation of inflammatory, vascular or cell survival gene sets. Up-regulated expression of gene sets associated with KEGG pathways was observed among others for "ECM-receptor interaction", "Cytokine-cytokine receptor interaction", "Leukocyte transendothelial migration", "VEGF signaling pathway", "HIF-1 signaling pathway", "p53 signaling pathway", and "Apoptosis", which are typically activated in stroke pathogenesis (Baeten and Akassoglou, 2011; Doyle *et al*., 2008; Marti *et al*., 2000; Wang *et al*., 2017; Yilmaz and Granger, 2010). On the other hand, transcripts associated with gene sets relevant for pathways involved in the function of neurons were downregulated, such as "Glutamatergic synapse", "GABAergic synapse", "Calcium signaling pathway", and "Nicotine addiction" caused by the loss of neurons after cerebral ischemia (Lee *et al*., 2000; Won *et al*., 2002). Representative pathways including heatmaps of representative genes from each pathway are depicted in Figure 10. A complete list of activated pathways is shown in Table 8, page 87.

The comparison between the ischemic hemispheres of *Ephb2*$^{+/+}$ and *Ephb2*-deficient animals showed that transcripts associated with inflammatory, vascular or cell survival pathways were less activated in the *Ephb2*-deficient hemispheres, while transcripts associated with pathways describing neuronal function were upregulated in the absence of EphB2 (Figure 11, Table 9, page 89). The differences in the transcriptomes between the ipsilateral hemispheres revealed that cerebral ischemia was attenuated in *Ephb2*-deficient animals on a transcriptional level.

Finally, the comparison of the contralateral hemispheres of both genotypes identified several transcripts associated with pathways in *Ephb2*-deficient mice which were already differently regulated under normoxic conditions. Among others, the transcriptomes of genes involved in the pathways "Nicotine addiction" and "Glutamatergic synapse" are not equally expressed (Figure 12, Table 10, page 91). Within both pathways, genes encoding subunits of the NMDA receptor were differently regulated when compared to *Ephb2*$^{+/+}$ normoxic hemispheres, confirming previous studies highlighting the importance of EphB2 for proper NMDA receptor function and localization (Henderson *et al*., 2001; Nolt *et al*., 2011).

Taken together, the transcriptome analysis confirmed the attenuation of cerebral ischemia in *Ephb2*-deficient mice on the transcriptional level and further revealed differences in the expression of genes encoding products associated with synaptic pathways between the two genotypes at a basal level.

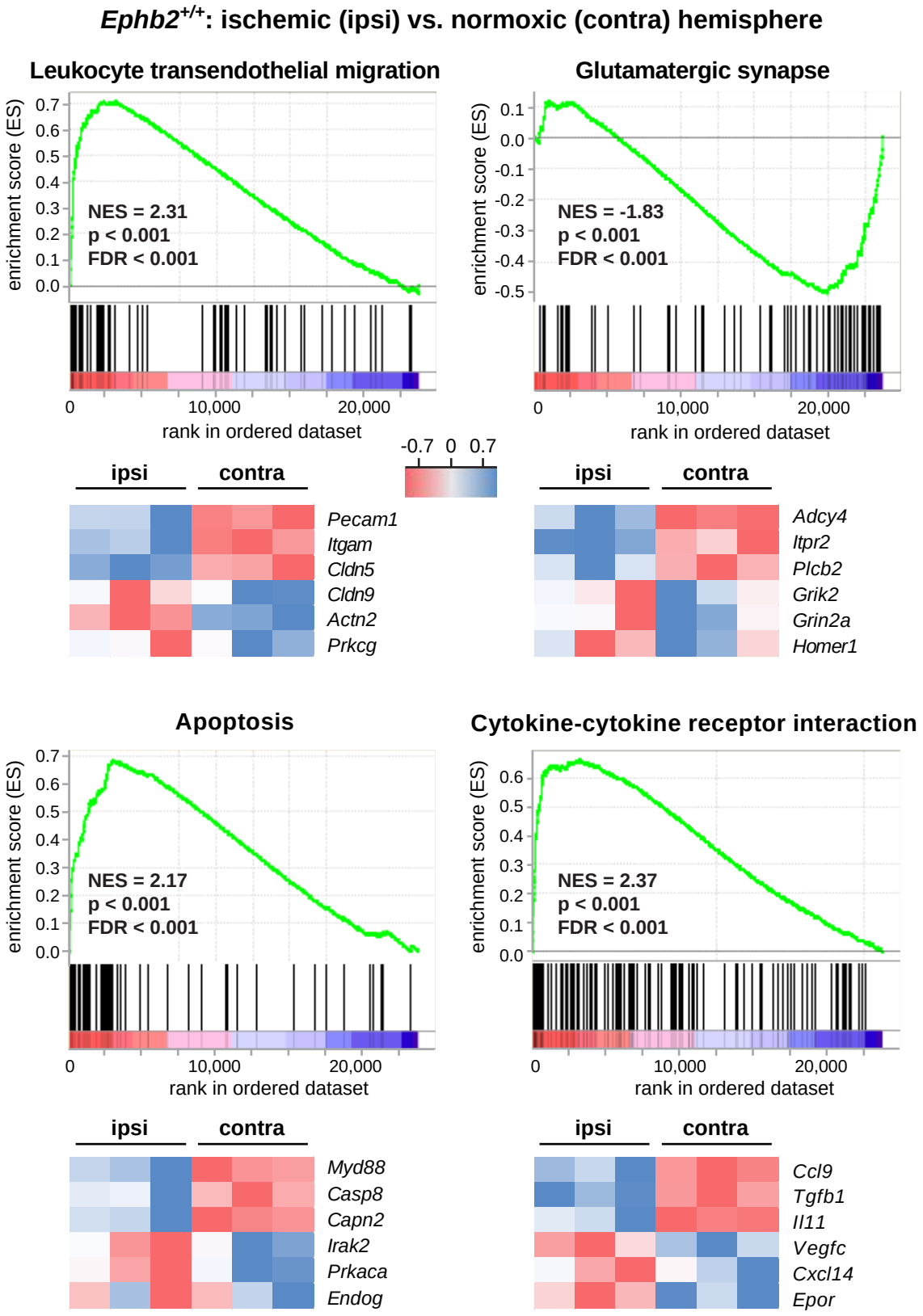

Figure 10: Transcriptome analysis of *Ephb2*$^{+/+}$ mice after stroke. *Ephb2*$^{+/+}$ were subjected to 60 min middle cerebral artery occlusion (MCAo) followed by 48 h of reperfusion. DNA microarray and gene set enrichment analysis of the ipsi- and contralateral hemispheres showed differentially regulated pathways (obtained from KEGG database). Representative pathways including example genes are depicted here. Expression levels are normalized to row maximal and minimal values. N=3. (N)ES=(normalized) enrichment score, FDR=false discovery rate

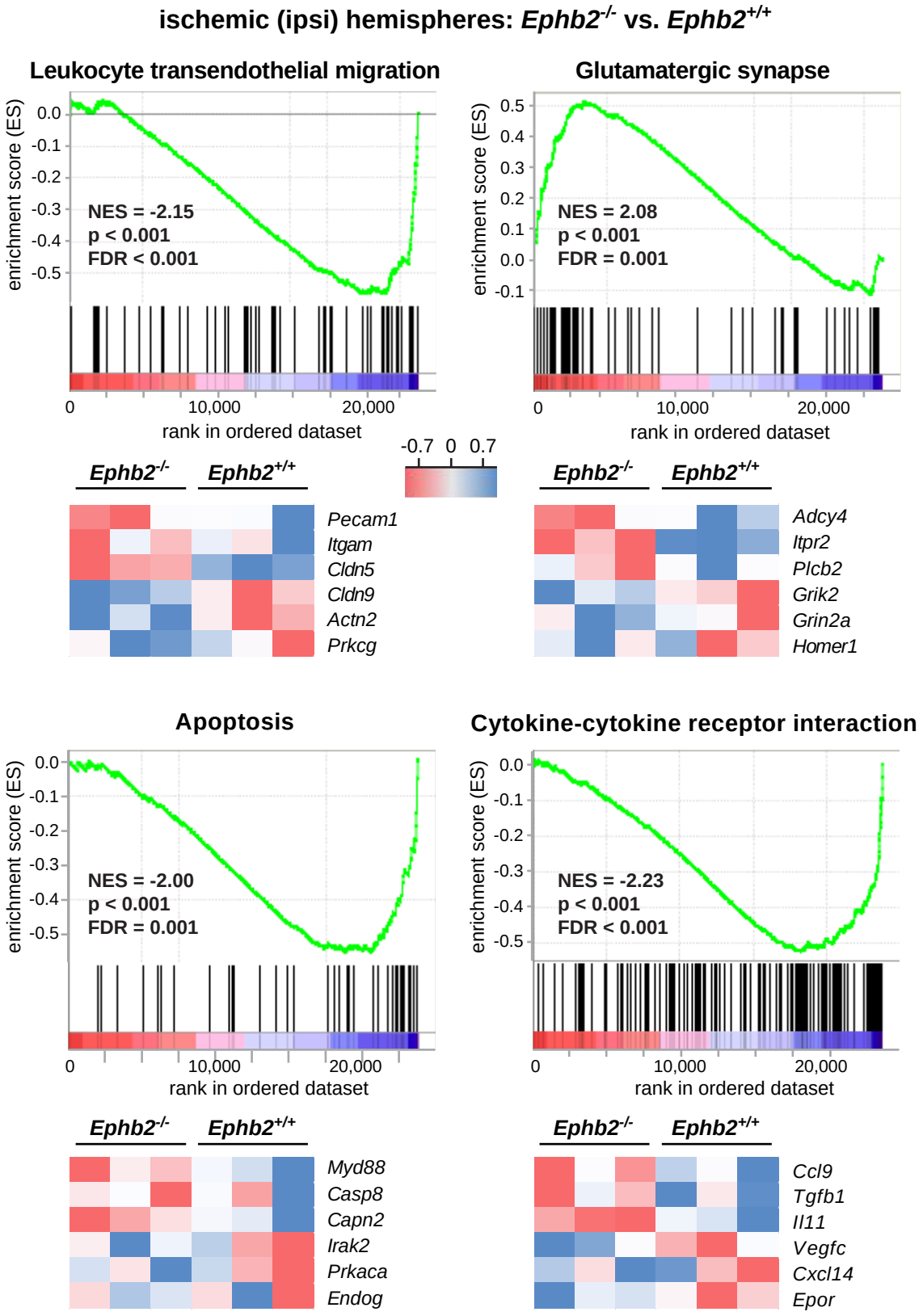

Figure 11: Comparison of transcriptomes upon stroke. *Ephb2*$^{+/+}$ and *Ephb2*$^{-/-}$ mice were subjected to 60 min middle cerebral artery occlusion (MCAo) followed by 48 h of reperfusion. DNA microarray and gene set enrichment analysis of the ipsilateral hemispheres showed differentially regulated pathways (obtained from KEGG database). Representative pathways including example genes are depicted here. Expression levels are normalized to row maximal and minimal values. N=3. (N)ES=(normalized) enrichment score, FDR=false discovery rate

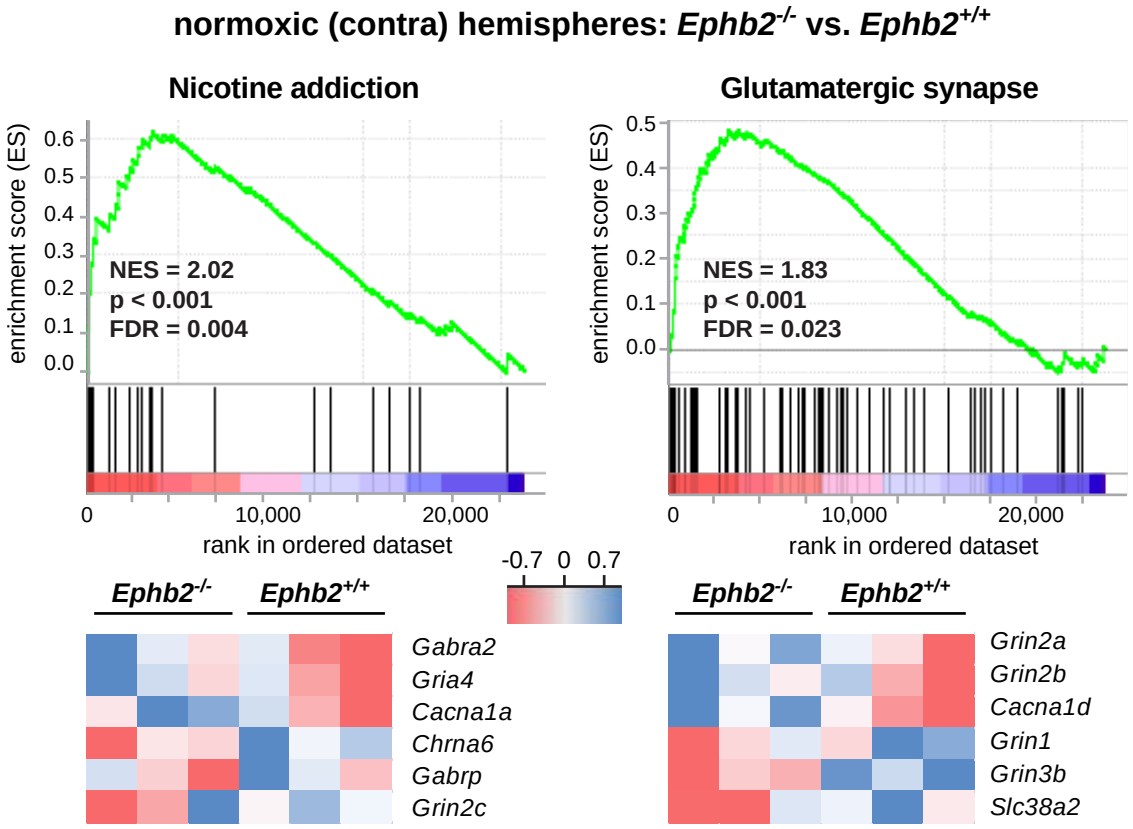

Figure 12: Comparison of transcriptomes under basal conditions. *Ephb2*$^{+/+}$ and *Ephb2*$^{-/-}$ mice were subjected to 60 min middle cerebral artery occlusion (MCAo) followed by 48 h of reperfusion. DNA microarray and gene set enrichment analysis of the contralateral hemispheres showed differentially regulated pathways (obtained from KEGG database). Representative pathways including example genes are depicted here. Expression levels are normalized to row maximal and minimal values. N=3. (N)ES=(normalized) enrichment score, FDR=false discovery rate

4.2 Analysis of vascular function in *Ephb2*-deficient mice

Vascular function and blood vessel growth play important roles in stroke pathogenesis and are influenced by the EphB/ephrin-B system. In mice lacking the Eph receptor ligand ephrin-B2 vascular, development is disrupted and leads to prenatal death before embryonic day 11.5 (Adams *et al.*, 1999). To unravel a possible impact of the deletion of EphB2 on the vascular system, histological and functional analysis were applied.

Brain arteries were visualized by transcardial perfusion with a pigment solution that cannot penetrate the capillary system. Then, images of the basal vessel structure Circle of Willis and the area supplied by the middle cerebral artery were taken. Branches supplying the area of the middle cerebral artery and branches directly originating from the middle cerebral artery were manually counted. *Ephb2*$^{+/+}$ and *Ephb2*$^{-/-}$ mice exhibited a similar gross anatomy of the circle of Willis and the number of artery branches of the middle cerebral artery was similar in both genotypes. Intravenous administration of a contrast agent and subsequent

µCT scans of two mice from each genotype visualized the venous anatomy of the head and did not reveal any gross differences between the genotypes (Figure 13).

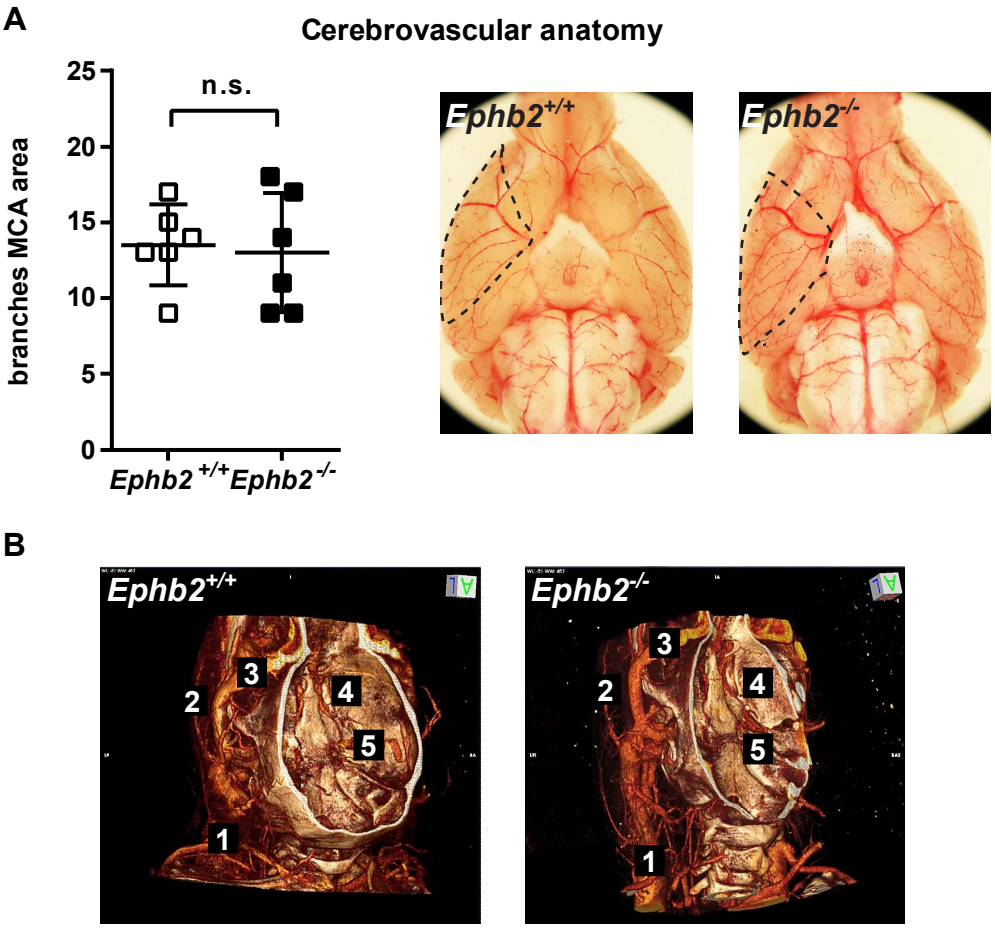

Figure 13: Cerebrovascular anatomy is not altered in *Ephb2*-deficient mice. **(A)** Brain vessels of *Ephb2*$^{+/+}$ and *EphB2*$^{-/-}$ mice were visualized with a particle-solution as shown on the right side. Branches of the middle cerebral artery were counted in the area indicated with the dotted line. N=6; Data are presented as single values (scatter plots) combined with the mean±SD; Mann-Whitney test, n.s.=not significant. **(B)** *Ephb2*$^{+/+}$ and *Ephb2*$^{-/-}$ mice were intravenously injected with a contrast agent and scanned with a µCT to visualize large cranial and cervical vessels. 1 = *Vena jugularis externa*, 2 = *Vena temporalis superficialis*, 3 = *Vena retromandibularis*, 4 = *Vena cerebri media*, 5 = *Vena basalis*.

The endothelial marker CD31 and desmin, which labels pericytes, were detected with immunofluorescence staining techniques. The CD31-specific fluorescence signal was used to calculate the capillary density, while the desmin-specific signal was used to evaluate the pericyte coverage of brain vessels. *EphB2*$^{-/-}$ animals did not show any differences in vessel density or pericyte coverage of brain vessels when compared to *Ephb2*$^{+/+}$ mice (Figure 14). Though *Ephb2*-deficient mice did not show any histologic differences in the vascular system, the function of *Ephb2*-defcient endothelial cells might have been altered in comparison to *Ephb2*$^{+/+}$ mice and was therefore analyzed in more detail.

The reduction in regional cerebral blood flow (rCBF) during MCAo was measured by a laser-Doppler probe as an increased blood supply could lead to less severe infarctions in *Ephb2*-deficient mice. However, the reduction in rCBF was similar in both genotypes (Figure 15A), indicating that the reduction in infarct and edema volumes seen in Figure 8 cannot be explained by a reduced induction of cerebral ischemia *per se*.

Disruption of endothelial tight junctions and rearrangement of tight junctional proteins such as ZO-1 are hallmarks of I/R injury. Subsequently, junctional integrity is impaired, thereby increasing blood-brain barrier (BBB) paracellular permeability which leads to vasogenic edema formation.

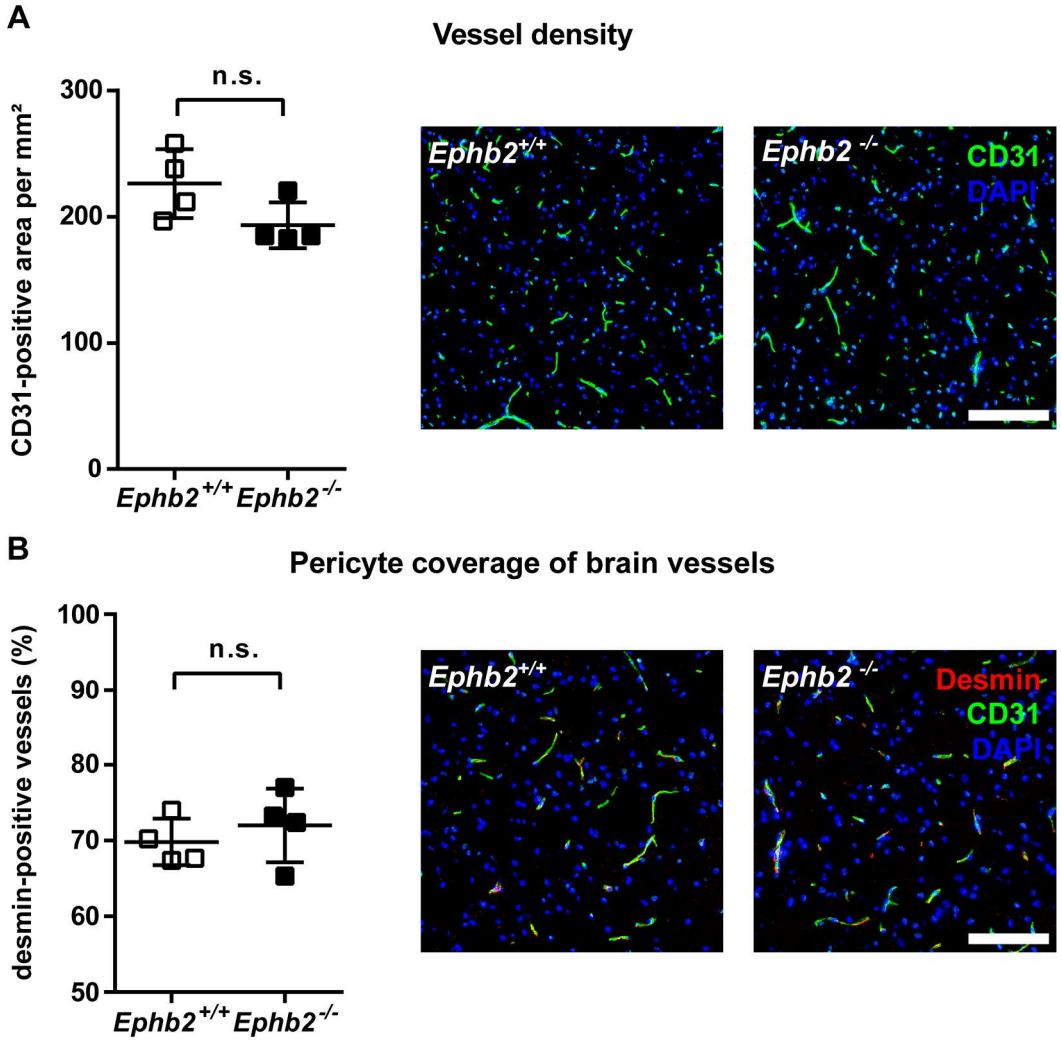

Figure 14: Brain vessel characteristics are comparable in *Ephb2*$^{+/+}$ and *Ephb2*$^{-/-}$ mice. CD31 and desmin were detected with immunofluorescence staining techniques in sagittal cryo-sections of brains of *Ephb2*$^{+/+}$ and *Ephb2*$^{-/-}$ mice. **(A)** Number of CD31-positive vessels per mm² and representative images. **(B)** Pericyte coverage of brain vessels representative images. Representative images were digitally enhanced for better clarity. N=4; Data are presented as single values (scatter plots) combined with the mean±SD; Mann-Whitney test, n.s.=not significant. Scale bar=100 µm.

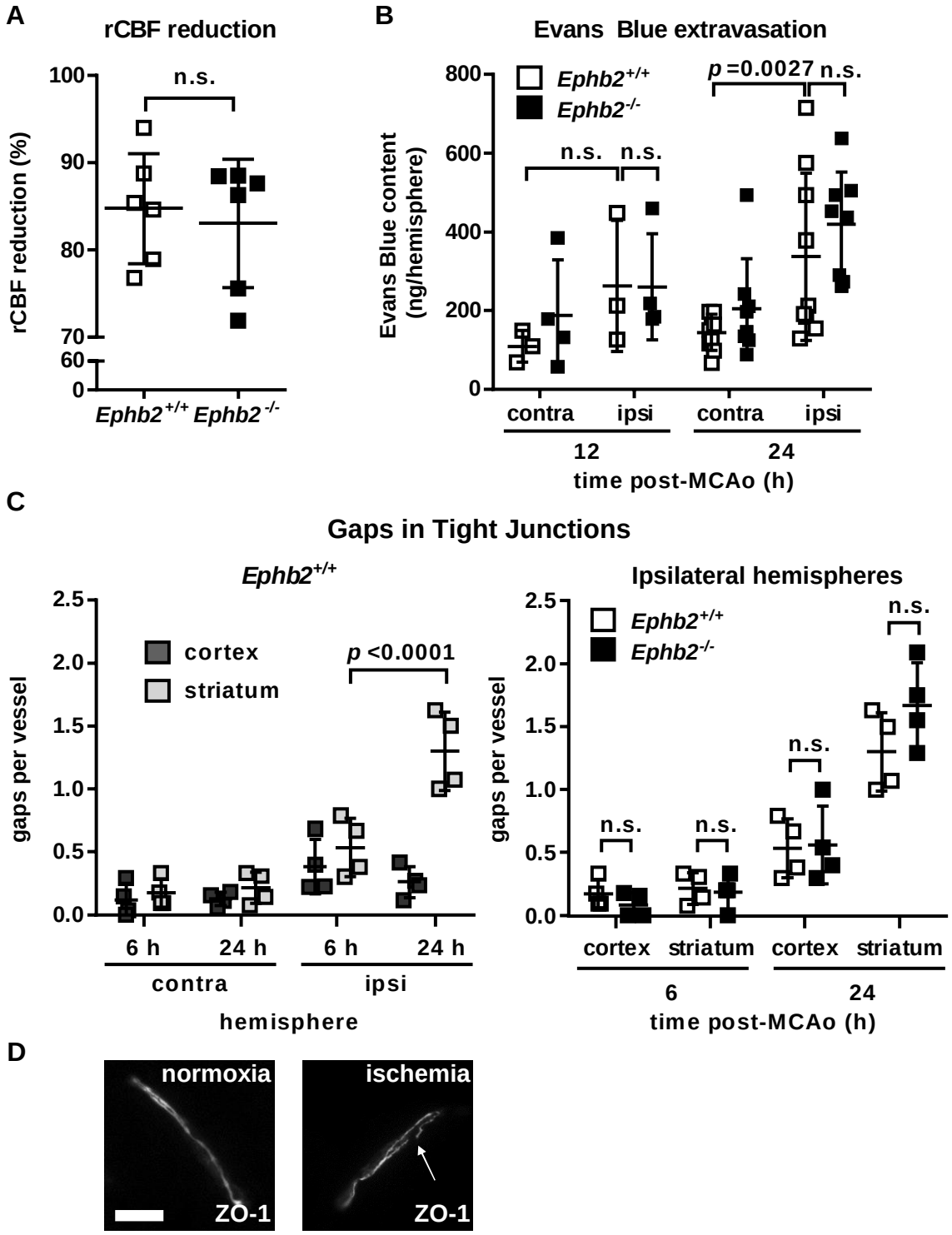

Figure 15: Endothelial permeability is not altered. *Ephb2*$^{+/+}$ and *Ephb2*$^{-/-}$ mice were subjected to middle cerebral artery occlusion (MCAo) followed by reperfusion as indicated. **(A)** Just before occlusion of the middle cerebral artery and immediately after occlusion, regional cerebral blood flow (rCBF) was measured using a laser-Doppler-probe on the skull of the mouse. N=6; Mann-Whitney test. **(B)** Evans Blue was injected via the tail vein. Evans Blue extravasation in each hemisphere was measured by absorption. 12 h: N=3/4; 24 h: N=9/8, Two-way ANOVA. **(C)** CD31 and ZO-1 were detected with immunofluorescence staining techniques in sagittal brain cryo-sections of of *Ephb2*$^{+/+}$ and *Ephb2*$^{-/-}$ mice. Cortex (periinfarct) and striatum (infarct core) were separately analyzed. N=4, Kruskal-Wallis test. (A)-(C): Data are presented as single values (scatter plots) combined with the mean±SD. n.s.=not significant. **(D)** Representative image for analysis in (C). Gaps (arrow head) in ZO-1 staining were counted in brain vessels. Scale=10µm.

BBB permeability was first assessed with the well-established Evans Blue assay. Here, the fluorescent dye Evans Blue is intravenously injected shortly before the end of reperfusion after MCAo. Because of its high affinity to serum albumin, an increase in BBB permeability can be measured as serum albumin only leaks into the brain parenchyma when the BBB is impaired. The assay showed an increase in Evans Blue content in the ipsilateral hemisphere upon stroke after 24 h, but not after 12 h of reperfusion. However, at both time points, the Evans Blue content in the ipsilateral hemispheres was similar in both genotypes (Figure 15B).

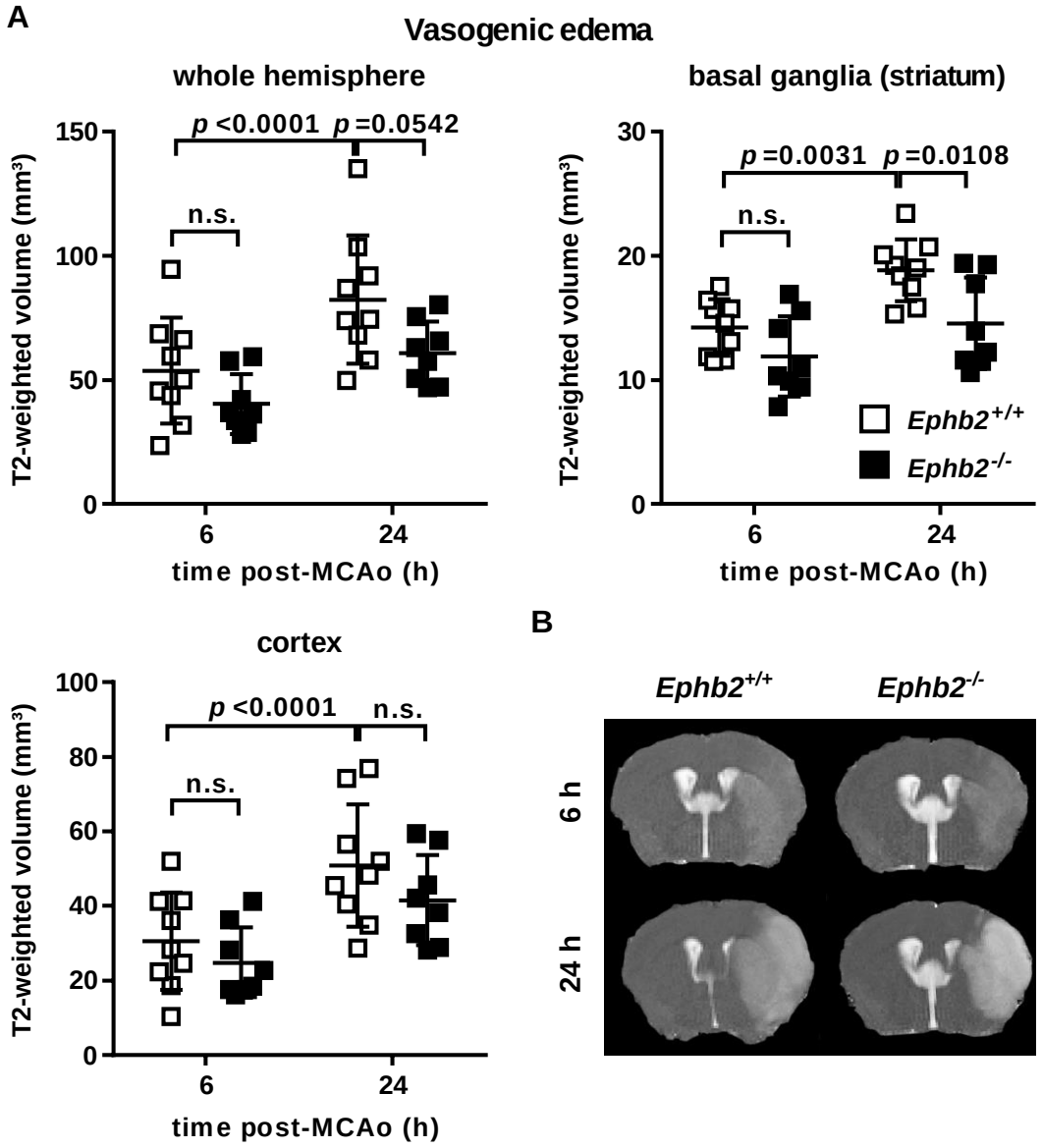

Figure 16: Vasogenic edema formation is reduced after 24 h of reperfusion in *Ephb2*-deficient mice. *Ephb2*$^{+/+}$ and *Ephb2*$^{-/-}$ mice were subjected to 60 min middle cerebral artery occlusion (MCAo) followed by 6 h and 24 h of reperfusion. High-resolution MRI at 9.4T was performed with a T2-weighted set-up. (A) T2-weighted volume indicates vasogenic edema size. N=8-9, Data are presented as single values (scatter plots) combined with the mean±SD, Two-way ANOVA, n.s.=not significant. (B) Representative image.

Next, gap formation in tight junctions was analyzed by counting the numbers of interruption in the ZO-1-specific fluorescent signal in striatum and cortex. Though this method showed an increase in gaps in tight junctions after 24 h of reperfusion in the ipsilateral striatum when compared to the contralateral region as expected, there was no difference between the two genotypes at any time point of in any brain region measured (Figure 15C).

Taken together, the paracellular leakage through the BBB and the rearrangment of endothelial junctional proteins were not different in the absence of EphB2.The post-mortem analysis regarding edema formation (Figure 8) revealed differences in the total edema volume between the two genotypes. However, the methods used so far to show the reduction in brain swelling in *Ephb2*-deficient mice did not differ between the two types of edema formation induced by stroke. The vasogenic edema is mainly caused by disruption of the BBB leading to extravasation and extracellular accumulation of fluid in the cerebral parenchyma. In contrast, cytotoxic edema does not involve dysfunction of endothelial permeability but is caused by an accumulation of ions in the intracellular space followed by massive influx of water. Subsequently, cells undergo swelling. Though cytotoxic edema formation itself does not induce addition of water mass into the brain parenchyma, it promotes vasogenic edema formation which finally results in brain swelling. By utilizing magnetic resonance imaging (MRI) with an imaging protocol including T2 relaxometry and diffusion-weighted imaging, it is possible to evaluate and differentiate between vasogenic and cytotoxic edema formation in the hyperacute phase (6 to 24 h post-MCAo) *in vivo* and in a longitudinal fashion.

To this end, mice were scanned 6 and 24 h after MCAo. The T2-weighted set-up was used to calculate the vasogenic edema, while diffusion-weighted imaging allowed to evaluate the formation of the cytotoxic edema by measurement of the apparent diffusion coefficient (ADC). T2-weighted volumes were measured in the whole ipsilateral hemisphere, in the cortex and in the basal ganglia which include the striatum. MRI scans confirmed an increase in all volumes in all areas from 6 to 24 h (Figure 16) as expected from other studies (Barber *et al*., 2005; Gerriets *et al*., 2009; Henninger *et al*., 2006; Zhang *et al*., 2016).

The volume of the vasogenic edema in the *Ephb2*-deficient mice was smaller after 24 h compared to *Ephb2*$^{+/+}$ mice, though not significantly (p=0.0542). Next, cortex and striatum were analyzed in greater detail as the cortex represents an area which is later affected upon stroke, while the striatum represents the infarction core. The comparison between the two genotypes did not show a difference in the T2-weighted volumes in the cortex at any time point. However, a significant reduction of 23% in the striatum of *Ephb2*-deficient mice after 24 h of reperfusion was observed.

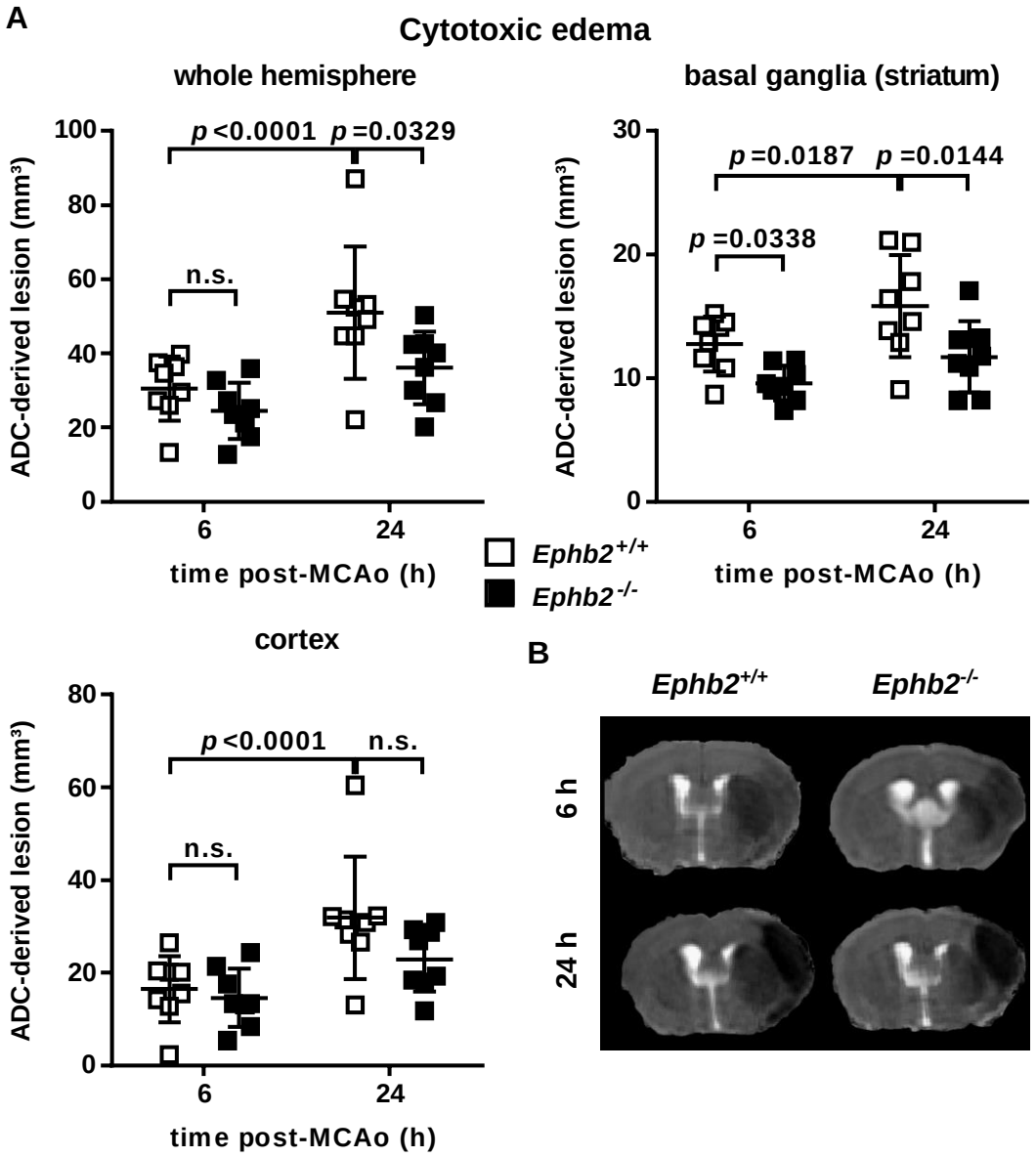

Figure 17: Cytotoxic edema formation is reduced after 6 h of reperfusion in *Ephb2*-deficient mice. *Ephb2*$^{+/+}$ and *Ephb2*$^{-/-}$ mice were subjected to 60 min middle cerebral artery occlusion (MCAo) followed by 6 h and 24 h of reperfusion. Diffusion-weighted imaging was performed with a high-resolution MRI at 9.4T. (A) Apparent diffusion coefficient (ADC)-derived lesion volume indicates cytotoxic cell swelling. N=8-9, Data are presented as single values (scatter plots) combined with the mean±SD, Two-way ANOVA, n.s.=not significant. (B) Representative images.

The ADC-derived lesion volume increased over time as it was already shown for the vasogenic edema. ADC-derived lesion volumes (Figure 17) in the whole ipsilateral hemispheres were reduced by 29% in *Ephb2*-deficient mice after 24 h of reperfusion, but not during the hyperacute phase 6 h after stroke. The cytotoxic edema did not differ in the cortex at any time point measured. However, in the striatum, the cytotoxic edema was already significantly smaller by 25% in the *Ephb2*$^{-/-}$ mice after 6 h and also later after 24 h of reperfusion.

Taken together, the results suggest that less cytotoxic edema evolves in the absence of EphB2 in the hyperacute phase after stroke (6 h of reperfusion), while the vasogenic edema develops to a similar extent after 6 h of reperfusion.

4.3 Evaluation of cytotoxic effects in *Ephb2*-defcient mice

The results shown in Figure 16 and Figure 17 insinuate that the attenuation in progression of stroke in the absence of EphB2 was not caused by a dysregulation of endothelial function in *Ephb2*$^{-/-}$ mice but rather by a reduction of cytotoxic effects in the early phase after stroke.

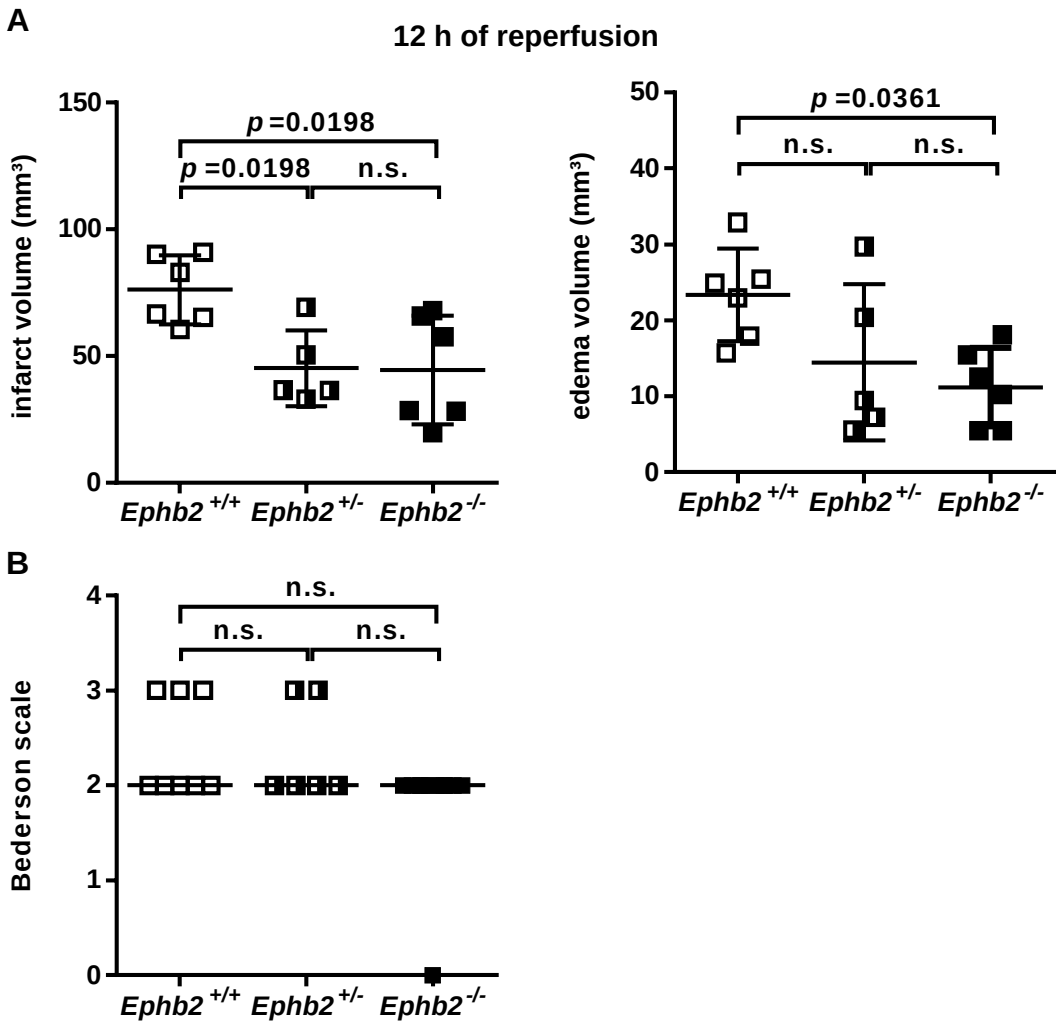

Figure 18: Infarct and edema sizes differ already 12 h after reperfusion. *Ephb2*$^{+/+}$, *Ephb2*$^{-/-}$ and *Ephb2*$^{+/-}$ mice were subjected to 60 min middle cerebral artery occlusion (MCAo) followed by 12h of reperfusion. **(A)** Infarct and edema volumes were determined in Nissl-stained brain sections as in Figure 8. Data are presented as single values (scatter plots) combined with the mean±SD; N=6/5/6; One-way ANOVA test. **(B)** Animals were treated as in (A). Neurological deficit score was determined as described in Figure 9. Data are presented as single values (scatter plots) combined with the median; N=8/6/11; Kruskal-Wallis test, n.s.=not significant.

Therefore, the infarct volumes were determined earlier than 24 h of reperfusion. As cresyl violet staining is not sensitive enough to enable identification of an infarction at 6 h after stroke, infarct volume was determined at 12 h after stroke.

Both *Ephb2*-deficient and *Ephb2* heterozygous mutants showed significantly decreased infarct volumes 12 h after stroke. The edema volume determined by Nissl staining showed a difference between *Ephb2*$^{+/+}$ and *Ephb2*$^{-/-}$ mice. Neuronal function determined by Bederson scale, which was developed to show successful infarction after 24 h, was not different between the three genotypes.

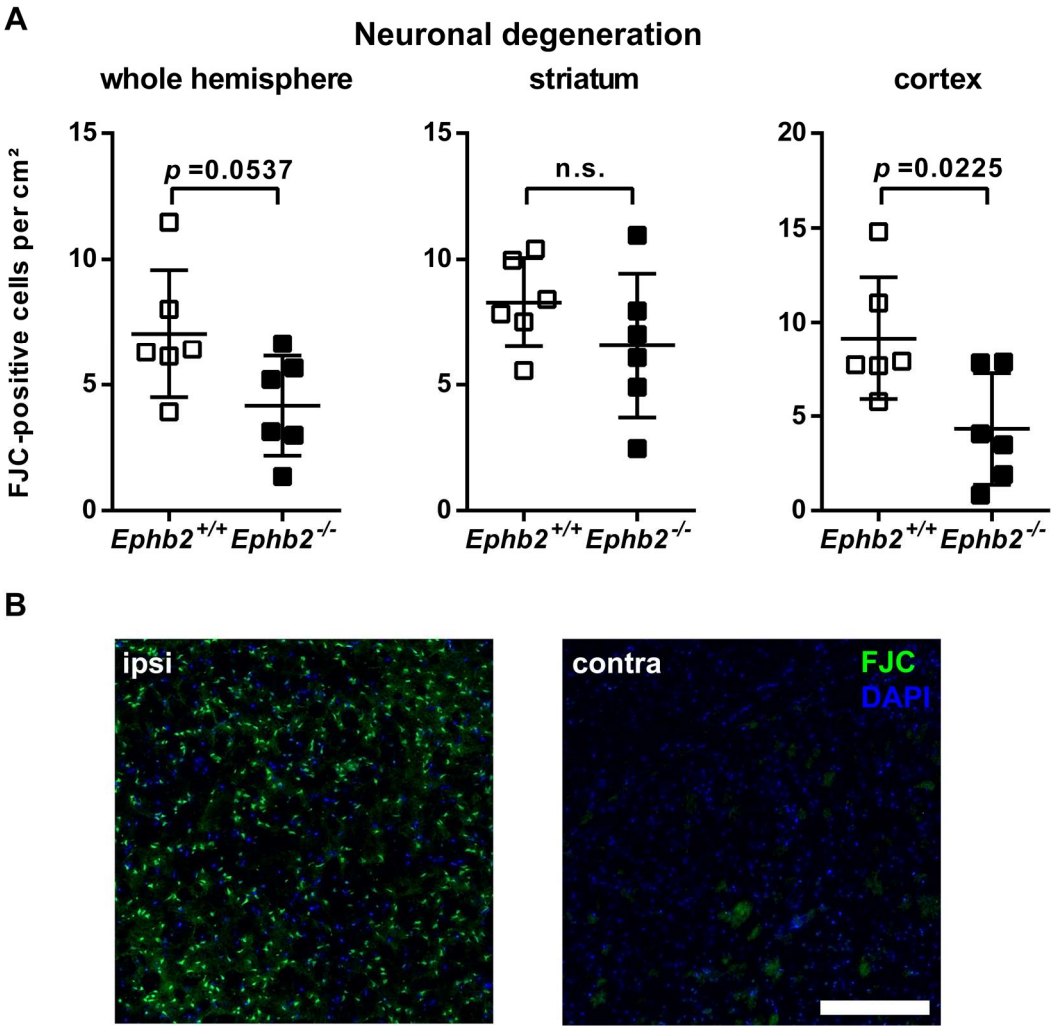

Figure 19: Neuronal degeneration is attenuated in *Ephb2*-deficient mice. *Ephb2*$^{+/+}$ and *EphB2*$^{-/-}$ mice were subjected to 60 min middle cerebral artery occlusion (MCAo) followed by 12 h of reperfusion. Degenerative neurons in brain cryo-sections were labeled by Fluoro-Jade C (FJC) staining. Data are presented as single values (scatter plots) combined with the mean±SD; N=6; Student's *t*-test. (B) Representative images of ipsi- and contralateral regions after FJC staining. Representative images were digitally enhanced for better clarity Scale bar=100 µm.

Next, the neuronal degeneration was determined in cryo-sections of *Ephb2*$^{+/+}$ and *Ephb2*$^{-/-}$ mice 12 h after stroke. Neuronal degeneration is a process leading to the loss of function and/or death of neurons and was determined by Fluoro Jade C staining, which is a fluorochrome specifically labeling neurons undergoing neurodegeneration (Schmued and Hopkins, 2000). Neuronal degeneration was reduced in the whole ipsilateral hemisphere in *Ephb2*-deficient mice when compared to *Ephb2*$^{+/+}$ mice, though not significantly. Neuronal degeneration was similar in both genotypes in the infarction core, the striatum, 12 h after stroke. However, in the cortex, an area which is later affected, neuronal degeneration was significantly reduced in the *Ephb2*-deficient mice compared to control mice.
Taken together, neuronal degeneration in the cortex was already reduced in the hyperacute phase (12 h of reperfusion) in *Ephb2*-deficient mice.

4.4 EphB2 activation in the early hyperacute phase after stroke

The *Ephb2*-deficient mutant mice used in this study has developmental defects as described previously (Grunwald *et al*., 2001; Henderson *et al*., 2001; Henkemeyer *et al*., 1996). The observed attenuation of progression of stroke could be explained by an overall different preconditioning of these mice caused by developmental differences rather than by an involvement of EphB2 in stroke pathogenesis in general.
Activation of EphB2 and subsequent signal induction can be determined by its phosphorylation. To this end, brain lysates of *Ephb2*$^{+/+}$ mice subjected to MCAo followed by 6 h of reperfusion were applied to a protein array to assess phosphorylation levels of 39 different murine receptor tyrosine kinase (RTK) proteins including members of the Eph receptor family.
Phosphorylation of EphB2 was significantly increased in the ipsilateral hemispheres, indicating an involvement of EphB2 in stroke pathogenesis. At 6 h after reperfusion, the overall abundance of EphB2 is not reduced in the ipsilateral hemisphere as shown by immunofluorescence staining techniques and measurement of protein levels in brain lysates. However, EphB2 abundance decreased over time according to the loss of neurons (Figure 20).

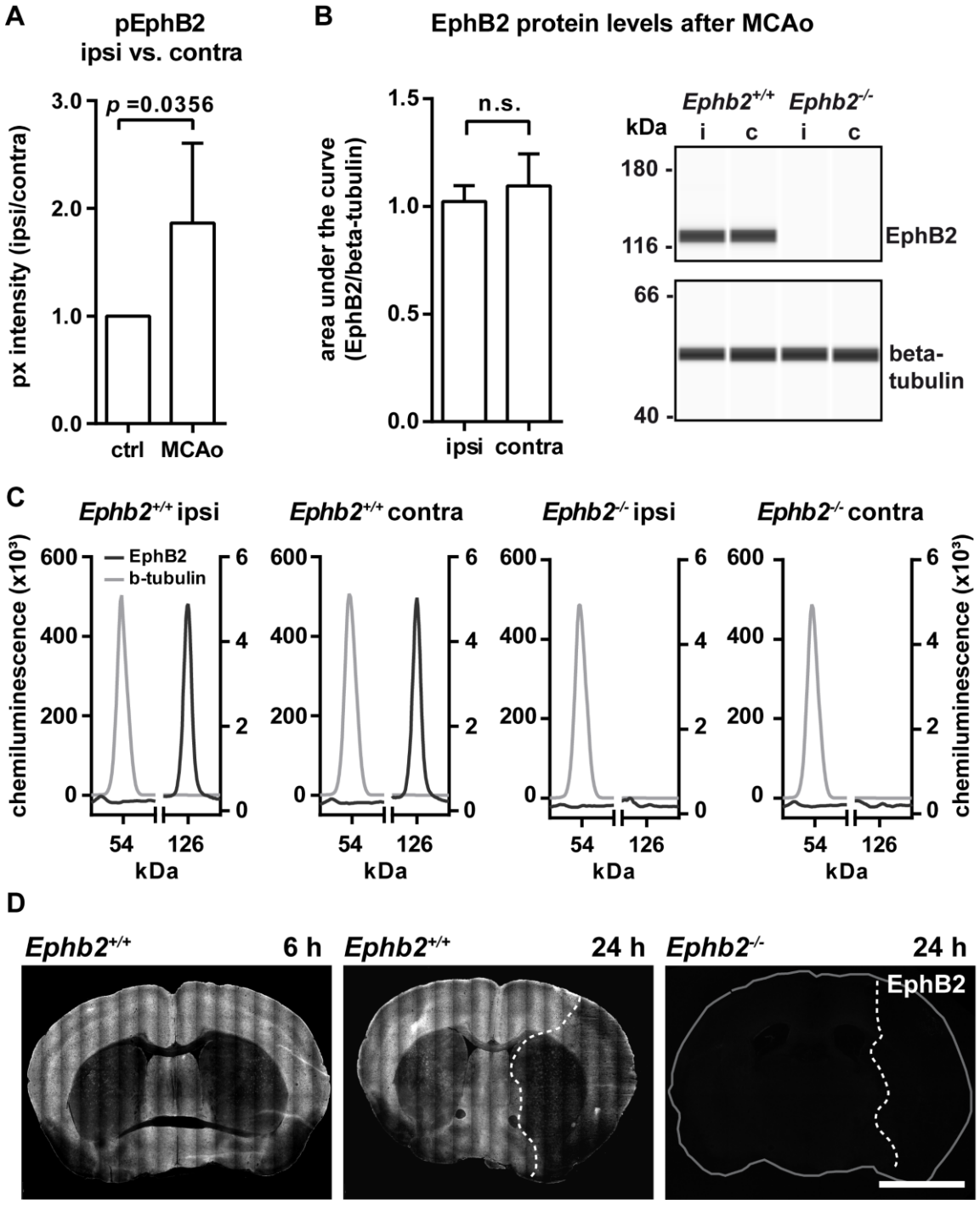

Figure 20: EphB2 is phosphorylated in the early hyperacute phase upon stroke. **(A)** *Ephb2*$^{+/+}$ mice were subjected to 60 min middle cerebral artery occlusion (MCAo) followed by 6 h of reperfusion. Brains were divided into contralateral (normoxic) and ipsilateral (ischemic) hemispheres and applied to proteome profiler membranes (protein-concentration matched amounts) for detection of phosphorylation levels of EphB2 (pEphB2). Ratio of pEphB2 levels in the ipsi- vs. the contralateral hemisphere was calculated and compared to ideal control (ctrl). N=6, mean±SD, Student's t-test with Welch's correction. (B) Lysates from (A) were analyzed by capillary electrophoresis for detection of EphB2-levels. N=3, mean±SD, Mann-Whitney test, n.s.=not significant. **(C)** Peak analysis of Simple Western analysis software. **(E)** Mice were treated as in Figure 15C. Representative images showing detection of EphB2 in cryo-sections by applying immunofluorescence-based techniques. Dotted line indicates border of infarcted are. Grey line in lower right panel indicates tissue border. Scale=5mm.

4.5 Involvement of further members of the EphB/ephrin-B family in the hyperacute phase after stroke

The evaluation of the phosphorylation levels of RTKs revealed that many RTKs are activated after cerebral ischemia (Figure 21 and Figure 22). For instance, phosphorylation of macrophage-stimulating protein receptor (MSPR), platelet-derived growth factor receptor (PDGFR) alpha and beta, tropomyosin receptor kinase C (TrkC) and VEGF receptors was increased and used as identification of an adequate cerebral ischemia, since the activation of these proteins have already been shown to be involved in cerebral ischemia or similar brain insults (Renner *et al*. 2003; Suzuki *et al*. 2008; Ma *et al*. 2011; Greenberg & Jin 2013; Chung *et al*. 2017).

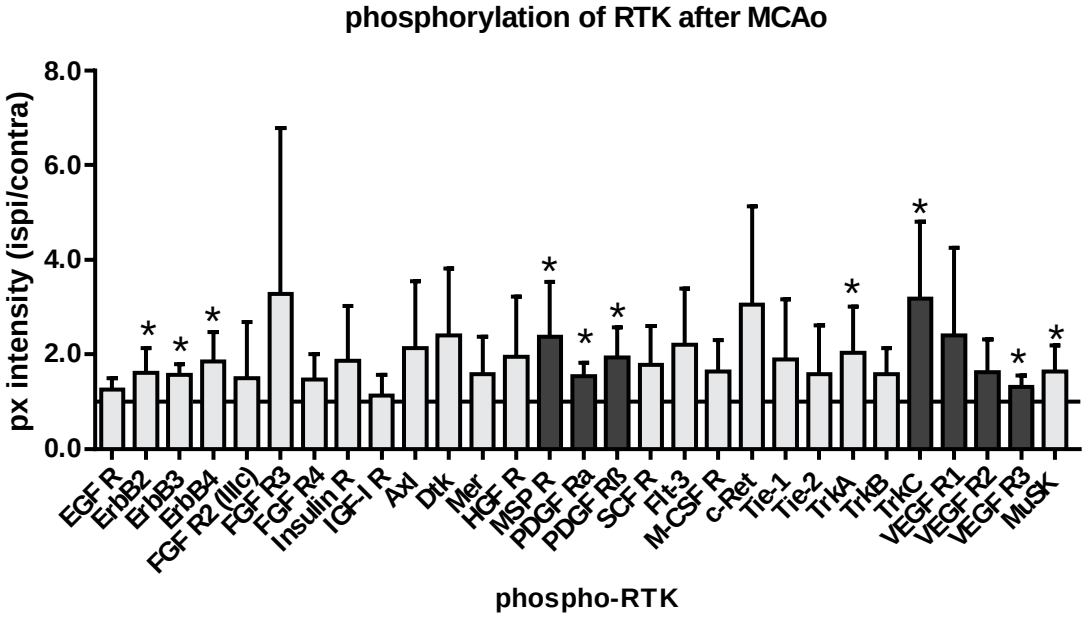

Figure 21: Phosphorylation levels of various RTKs (without Eph receptors) are elevated upon cerebral ischemia. *Ephb2*$^{+/+}$ mice were subjected to 60 min middle cerebral artery occlusion (MCAo) followed by 6 h of reperfusion. Brains were divided into contra-(non-ischemic) and ipsi-(ischemic)lateral hemispheres and applied to proteome profiler membranes for detection of phosphorylation levels of receptor tyrosine kinases. RTKs, which were selection-criteria for successful induction of cerebral ischemia are highlighted in dark grey. N=6, mean±SD, Student's t-test with Welch's correction.

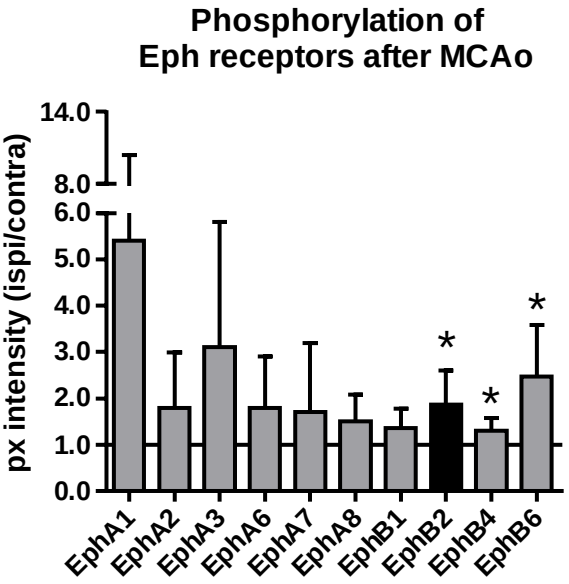

Figure 22: Phosphorylation levels of Eph receptors are increased upon cerebral ischemia. *Ephb2*$^{+/+}$ mice were subjected to 60 min middle cerebral artery occlusion (MCAo) followed by 6 h of reperfusion. Brains were divided into contralateral (non-ischemic) and ipsilateral (ischemic) hemispheres and applied to proteome profiler membranes for detection of phosphorylation levels of receptor tyrosine kinases. EphB2 is highlighted as this data point is also depicted in Figure 20. N=6, mean±SD, Student's t-test with Welch's correction. *: $p<0.05$.

MCAo did not only induce phosphorylation of EphB2 but also of other Eph receptors underlining the importance of the Eph receptor family in stroke pathogenesis. Phosphorylation levels of EphB4 and EphB6 were significantly elevated in the ipsilateral hemisphere. EphA1, 2, 3, 6, 7 and 8 also showed increases in phosphorylation levels, however, not significantly (Figure 22). In addition to EphB2 (Figure 20), expression levels of EphB2 ligands, ephrin-B1 and ephrin-B2, were analyzed in cryo-section 6 and 24 h after MCAo. Immunofluorescence staining showed a similar decay of ephrin-B1- and ephrin-B2-specific intensity after 24 h of reperfusion in the ipsilateral hemisphere in both genotypes. Fluorescence intensity specific for the Eph receptor EphB4, which is mainly expressed on veins, declined only slightly (Figure 23).

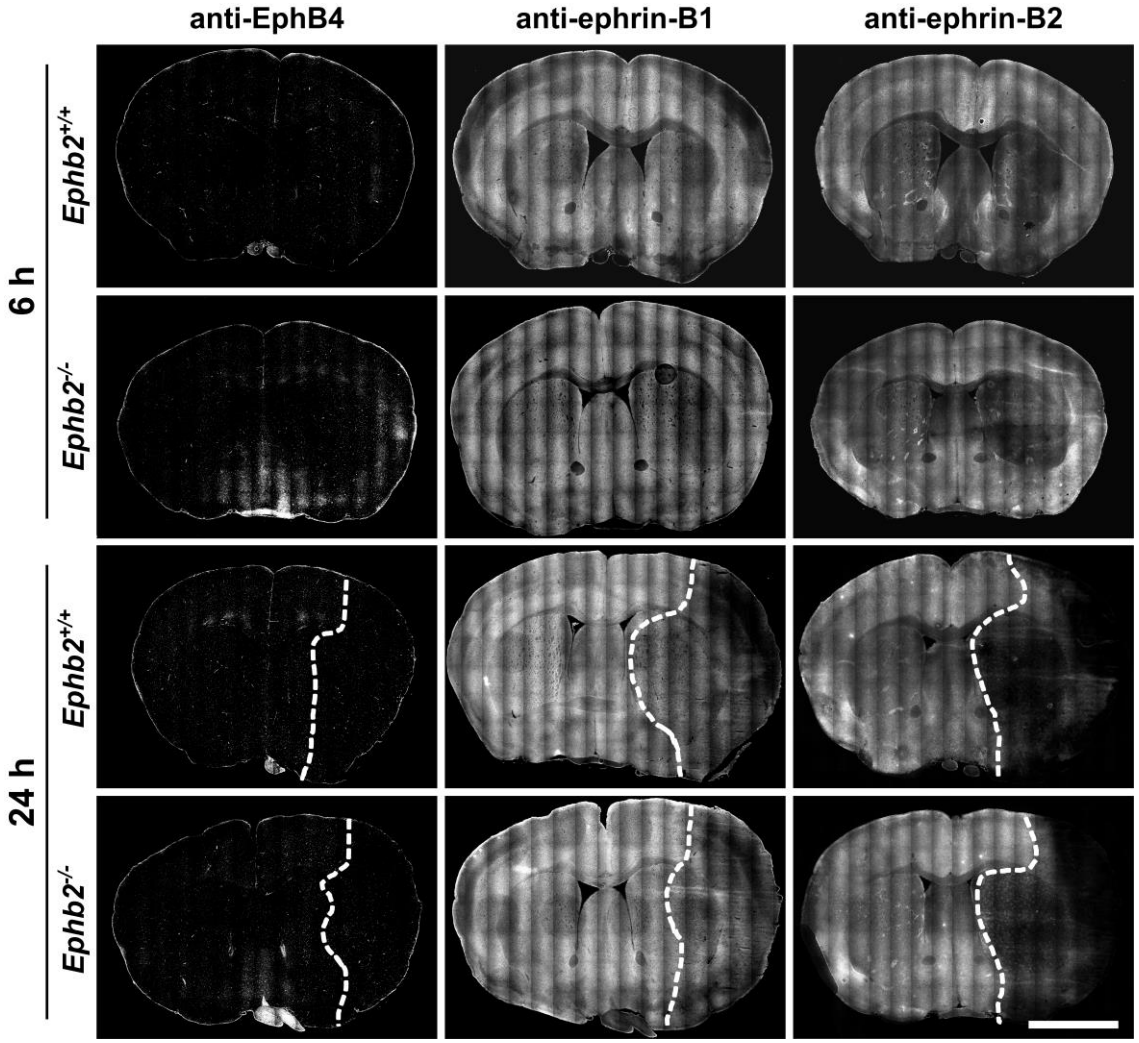

Figure 23: Immunofluorescent staining of members of the EphB/ephrin-B family. *Ephb2*$^{+/+}$ and *EphB2*$^{-/-}$ mice were subjected to 60 min middle cerebral artery occlusion (MCAo) followed by 6 h or with 24 h of reperfusion. EphB4, ephrin-B1 and ephrin-B2 were detected with immunofluorescence staining techniques in sagittal cryo-sections of brains of *Ephb2*$^{+/+}$ and *Ephb2*$^{-/-}$ mice. Representative images were digitally enhanced for better clarity. Dotted line indicates border of infarct obtained from corresponding Nissl-stained cryo-sections. Corresponding immunofluorescence staining of EphB2 is shown in Figure 20. Scale bar=5mm.

4.6 Analysis of NMDA receptor function in *Ephb2*-deficient neurons

Excessive release of glutamate into the extracellular space and subsequent overactivation of NMDA receptors is a crucial step in the ischemic cascade. Previous studies already showed an impact of the Eph receptor EphB2 on NMDA receptor function (Dalva *et al*., 2000; Grunwald *et al*., 2001; Henderson *et al*., 2001; Nolt *et al*., 2011; Takasu *et al*., 2002). Activation of EphB2 with ephrin-B ligands induce interaction of EphB2 with the NMDA receptor subunit NR1 and phosphorylation of another subunit of the NMDA receptor, NR2B. This phosphorylation is required for Ca^{2+} influx through the NMDA receptor and induction of further signaling processes (Dingledine *et al*., 1999). It was already shown that *Ephb2*-

defcient neurons exhibit reduced NMDA receptor-mediated signaling (Dalva *et al*., 2000). The results from previous studies suggest that activation of EphB2 with ephrin-B ligands modulates Ca^{2+} influx through the NMDA receptor in neurons. NMDA receptor overstimulation leads to an increase in cytoplasmic calcium as well as accumulation of calcium in mitochondria, and further to depolarization of the mitochondrial membrane potential which eventually causes cell death (Stanika *et al*., 2009a). Considering the importance of NMDA receptor-mediated excitotoxicity during cerebral ischemia, the next part of this study aimed at analyzing the function of NMDA receptors in *Ephb2*-deficient neurons in the context of excitotoxicity.

To this end, primary cortical cultures, mainly consisting of neurons (>80% Figure 1), were isolated from newborn (P0) brains of *Ephb2*$^{+/+}$ and *Ephb2*$^{-/-}$ mice and cultured for 10 days. At the tenth day *in vitro* (DIV10), neurons express EphB2 receptors (Figure 7) and functional glutamate receptors, are susceptible to NMDA-induced excitotoxicity (Fogal *et al*., 2005) and have developed an extensive network of synaptic contacts (Verderio *et al*., 1999). Cytoplasmic and mitochondrial Ca^{2+} levels as well as changes in mitochondrial membrane potentials were evaluated before and after NMDA receptor stimulation.

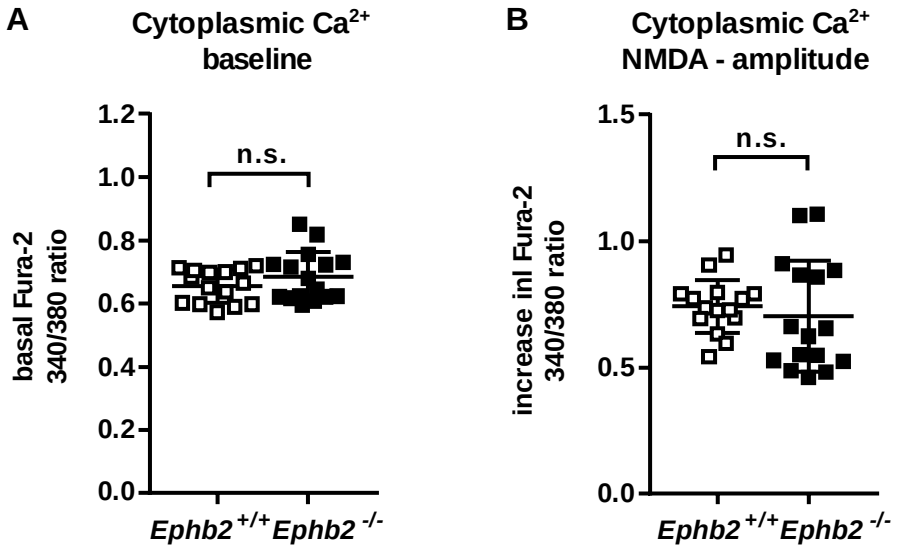

Figure 24: Cytoplasmic Ca^{2+} levels are not altered upon NMDA receptor stimulation. *Ephb2*$^{+/+}$ and *Ephb2*$^{-/-}$ forebrain neurons were obtained from P0 mice. Cytoplasmic Ca^{2+} imaging performed in control conditions **(A)** and brief (30 s) stimulation with 20 µM NMDA signal **(B)**. N=15/16 cover slips from 4 independent preparations. Data are presented as single values (scatter plots) combined with the mean±SD, Student's t-test, n.s.=not significant.

Ca^{2+} imaging using the ratiometric indicator Fura-2 was performed to examine global cytoplasmic Ca^{2+} levels at baseline and during selective stimulation of NMDA receptors. Neither baseline 340/380 fura-2 ratios (in the presence of inhibitors of voltage-dependent Ca^{2+}

channels, AMPA receptors, and voltage-dependent sodium channels to prevent AP bursts and associated Ca^{2+} signals) nor the amplitudes of indicator responses to brief (30 s) stimulation with 20 µM NMDA were different between the two genotypes. These results indicate that NMDA receptor-mediated cytoplasmic Ca^{2+} signaling is not grossly affected by the absence of Ephb2 (Figure 24) in cultured neuronal cells.

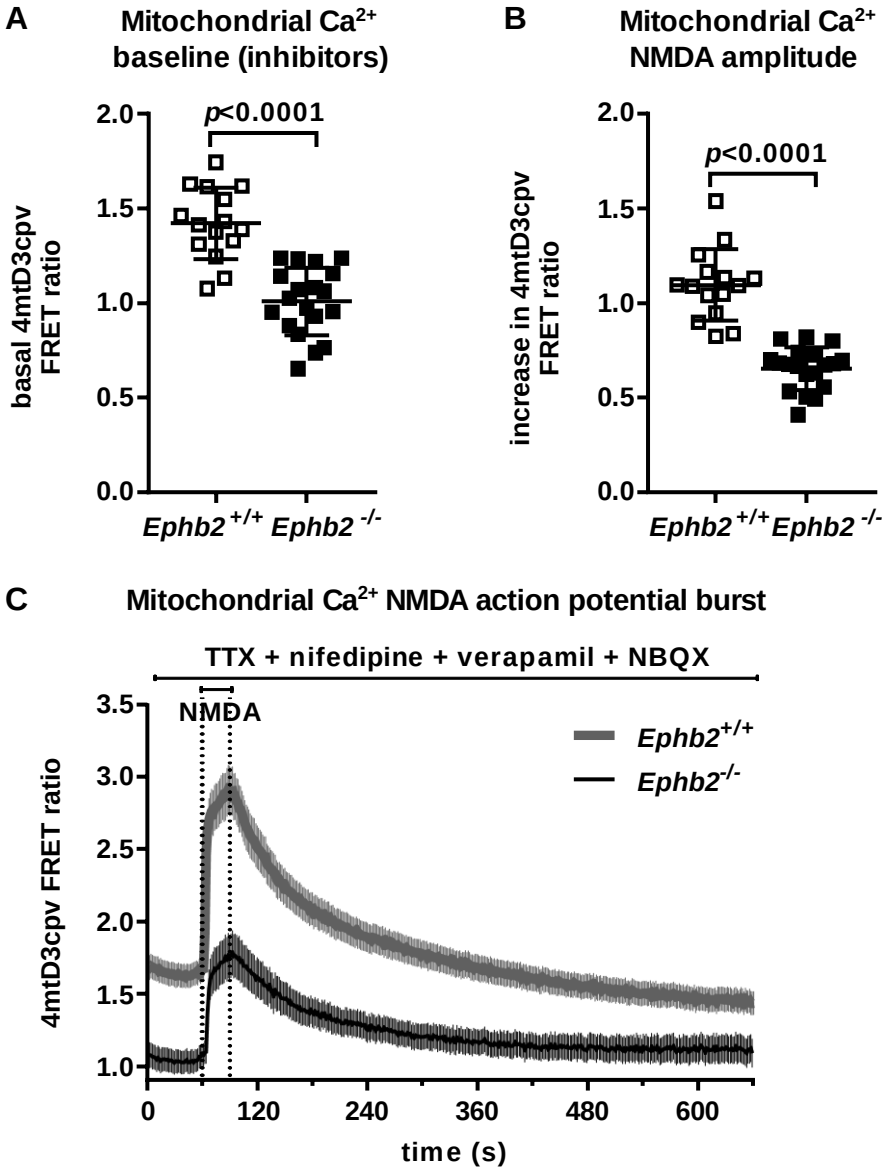

Figure 25: *Ephb2*-deficient mice have reduced NMDA receptor-dependent mitochondrial Ca^{2+} levels. *Ephb2*$^{+/+}$ and *Ephb2*$^{-/-}$ forebrain neurons were obtained from P0 mice. Mitochondrial calcium imaging performed with drugs in the bath to inhibit voltage-dependent calcium channels, AMPA receptors, and voltage-dependent sodium channels. This should prevent action potentials and all associated calcium signals, leaving the "pure" NMDA signal, which is evoked by a brief (30 s) application of 20 µM NMDA. Mitochondrial calcium levels after application of inhibitors **(A)** and after NMDA stimulation **(B)**. N=15/19 cover slips from 4 independent preparations. Data are presented as single values (scatter plots) combined with the mean±SD, Student's t-test. **(C)** Representative data for 1 cover slip each of *Ephb2*$^{+/+}$ and *Ephb2*$^{-/-}$ cells. Data are mean±SEM) N=15/19 cover slips from 4 independent preparations.

To measure mitochondrial Ca^{2+} levels, cells were infected with rAAVs driving the expression of a FRET-based Ca^{2+} indicator (4mtD3cpv) targeted to mitochondria. As previously, cells were treated with drugs inhibiting voltage-dependent Ca^{2+} channels, AMPA receptors, and voltage-dependent sodium channels to prevent APs and associated Ca^{2+} signals. Subsequently, cells were briefly stimulated with 20 µM NMDA thereby evoking an almost pure NMDA signal. Treatment with the inhibitors already resulted in a decreased baseline of the FRET ratio in *Ephb2*-deficient neurons. Further, the increase in the FRET ratio was significantly reduced in *Ephb2*-deficient neurons when compared to *Ephb2*$^{+/+}$ neurons (Figure 25). This suggests that the mitochondrial Ca^{2+} homeostasis regulated by NMDA receptors is impaired already under baseline conditions when EphB2 is absent, and to an even greater extent when NMDA receptors are stimulated.

As excessive NMDA receptor stimulation is known to promote cell death via breakdown of the mitochondrial membrane, the next experiments aimed at identifying whether and how the absence of EphB2 may alter mitochondrial membrane potential responses to NMDA receptor -stimulation. To these ends, cells were loaded with the fluorescent dye Rhodamine 123 (Rh123). Due to its positive charge, Rh123 accumulates under basal conditions within the mitochondrial matrix, where its high concentration leads to quenching. Mitochondrial membrane depolarization induces leakage of Rh123 from the mitochondria into the cytoplasm, where its fluorescence is dequenched resulting in intensive fluorescent intensity (Baracca *et al*., 2003). Exposing neurons to the mitochondrial uncoupler FCCP results in maximum fluorescence intensity of Rh123 and signal intensities of Rh123 are expressed as% of the maximum. Neurons were stimulated with 5 or 20 µM NMDA and changes in Rh123 fluorescence intensity during the subsequent 9 min were quantified. Stimulation with low-dose NMDA did not lead to changes to in the Rh123 intensity and did not reveal differences between the two genotypes. However, when cells were treated with 20 µM, *Ephb2*-deficient neurons showed a significantly smaller increase in Rh123 intensity when compared to *Ephb2*$^{+/+}$ neurons indicating that *Ephb2*-deficient neurons are less susceptible to NMDA-induced mitochondrial membrane depolarization (Figure 26).

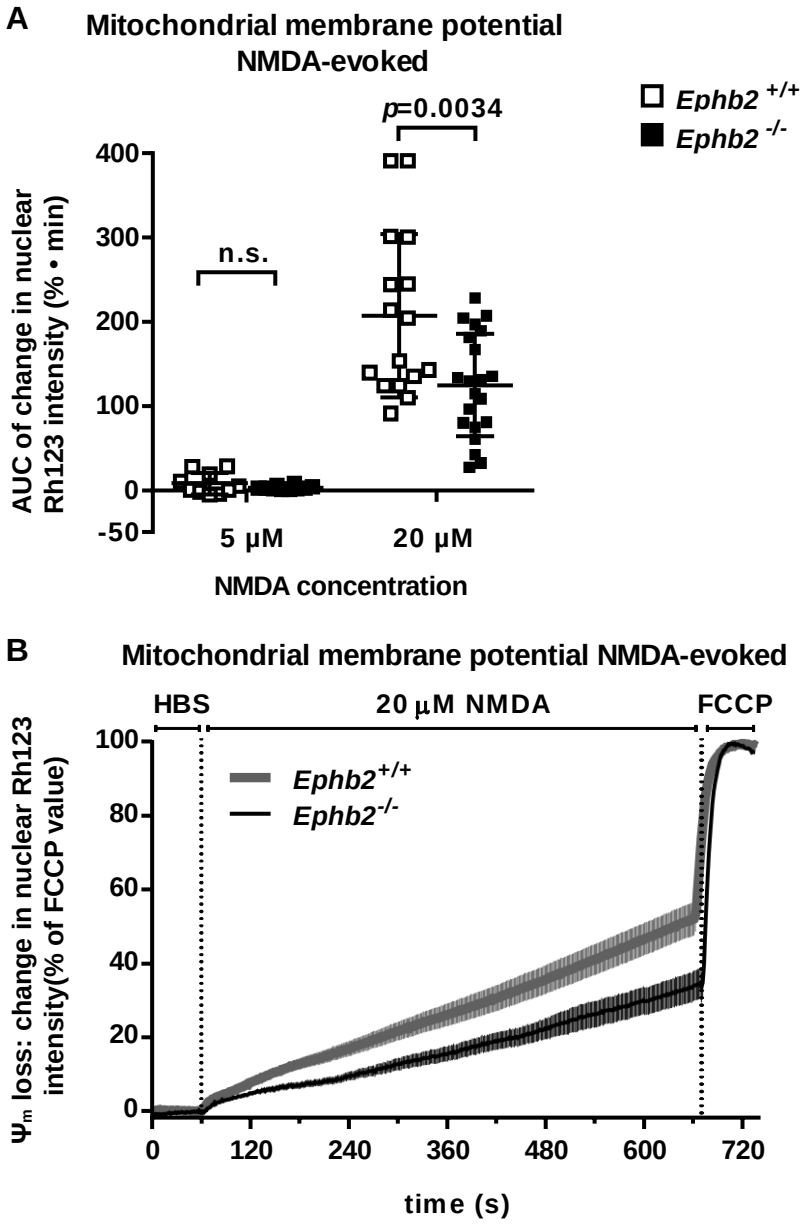

Figure 26: Mitochondrial membrane potential imaging. **(A)** Quantification of the area under the curve during the first 9 minutes of NMDA treatment for 5 and 20 µM NMDA. **(B)** Representative data for 1 cover slip each of *Ephb2*$^{+/+}$ and *Ephb2*$^{-/-}$ cells during stimulation with 20 µM NMDA over ~10 minutes. N=10 cover slips (5 µM), N=16/22 cover slips from 4 independent preparations. Data are presented as single values (scatter plots) combined with the mean±SD, Student's t-test, n.s.=not significant.

4.7 Ca^{2+} rises during action potential bursts are slightly attenuated in *Ephb2*-deficient neurons

Synaptic activity can trigger a nuclear Ca^{2+}-driven neuroprotective gene program leading to a reduction in excitotoxicity-associated mitochondrial Ca^{2+} load (Depp 2017). Consequently, neurons are less sensitive to excitotoxicity-mediated cell death (Depp 2017, Tauskela 2008). AP bursting was triggered by treatment with the GABAa receptor antagonist gabazine and cytoplasmic Ca^{2+} responses were measured with Fura-2 as above.

The amplitudes of cytoplasmic Ca^{2+} responses to a single burst of action potentials were attenuated in *Ephb2*-deficient neurons (Figure 27). However, mitochondrial Ca^{2+} levels, which were measured as before, were not different during action potential burst (Figure 28). Taken together, these data show both attenuated NMDA receptor -dependent mitochondrial Ca^{2+} signaling and diminished sensitivity of the mitochondrial membrane potential to NMDA receptor stimulation in *Ephb2*-deficient neurons. These findings support the hypothesis that *Ephb2*-deficient neurons might be protected from NMDA-induced excitotoxicity.

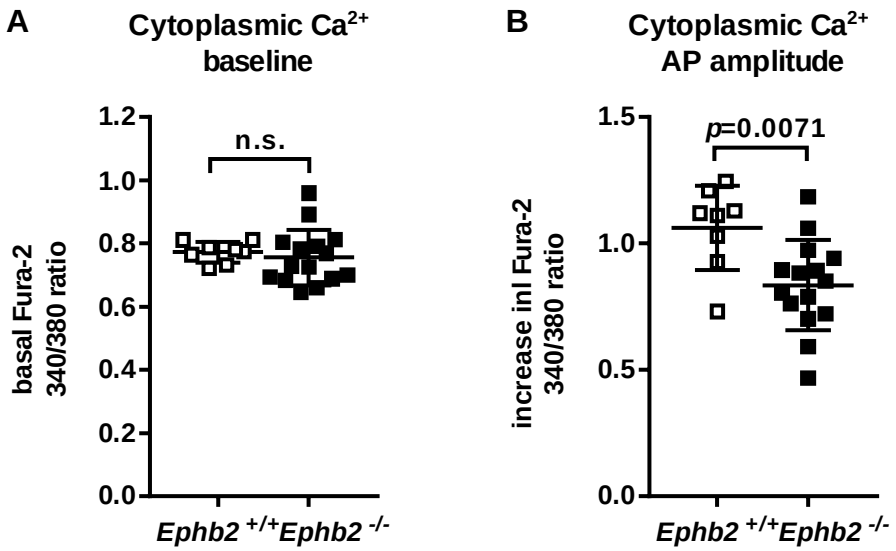

Figure 27: Cytoplasmic Ca^{2+} levels during AP burst. *Ephb2*$^{+/+}$ and *Ephb2*$^{-/-}$ forebrain neurons were obtained from P0 mice. Cytoplasmic calcium imaging performed in control conditions **(A)** and after action potential burst triggered by GABAa receptor antagonist gabazine, halted by TTX **(B)**. N=8/15 cover slip from 4 independent preparations. Data are presented as single values (scatter plots) combined with the mean±SD, Student's t-test, n.s.=not significant.

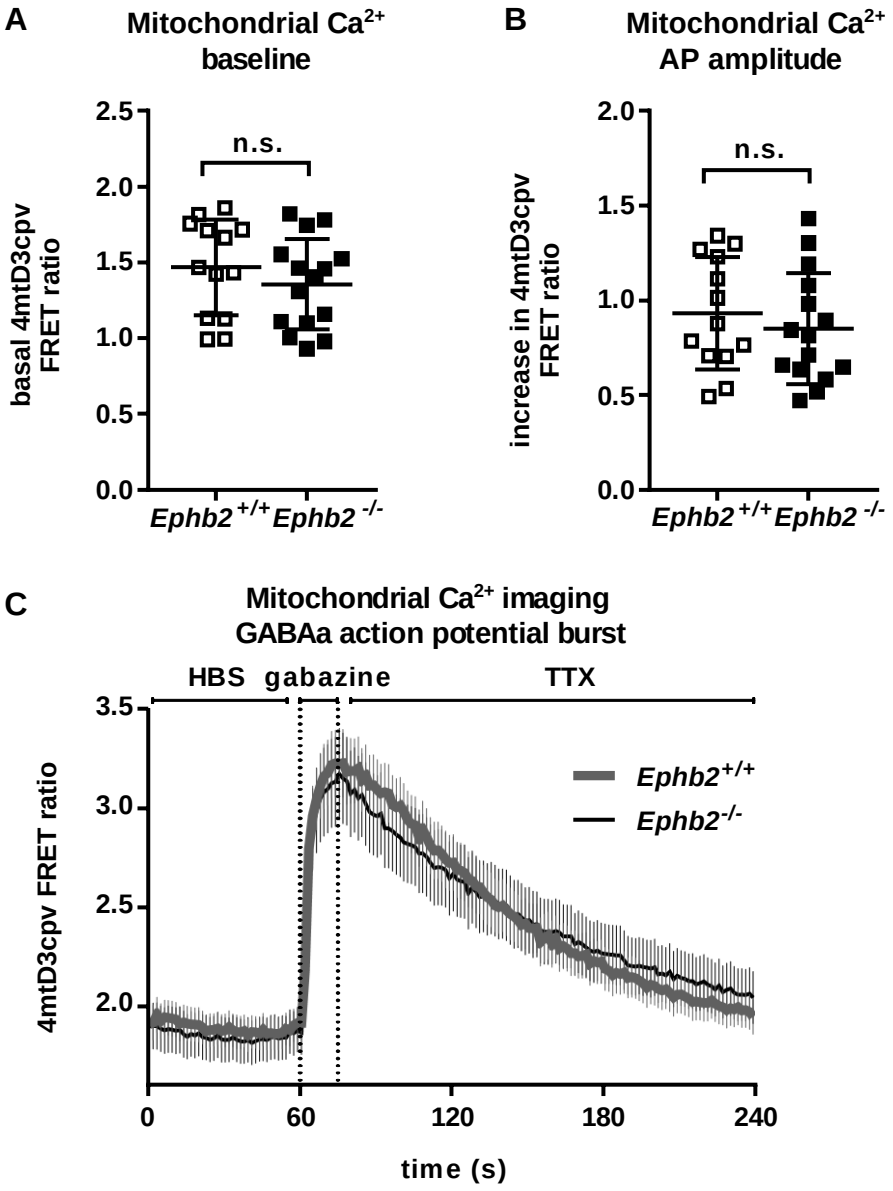

Figure 28: Mitochondrial Ca^{2+} levels during AP burst are not different. *Ephb2*$^{+/+}$ and *Ephb2*$^{-/-}$ forebrain neurons were obtained from P0 mice. Mitochondrial calcium imaging, action potential burst triggered by GABAa receptor antagonist gabazine, halted by TTX. **(A)** Mitochondrial calcium levels in control conditions. **(B)** Amplitude of AP-triggered mitochondrial calcium rises. N=13/15 CS from 4 independent preparations. Data are presented as single values (scatter plots) combined with the mean±SD, Student's t-test, n.s.=not significant. **(C)** Representative data for 1 cover slip each of *Ephb2*$^{+/+}$ and *Ephb2*$^{-/-}$ cells. Data are mean±SEM.

4.8 Excitotoxic NMDA receptor stimulation does not induce different levels of cell death in the absence of EphB2

To evaluate the influence of NMDA on excitotoxicity in greater detail, neurons from *Ephb2*$^{+/+}$ and *Ephb2*$^{-/-}$ mice were stimulated with increasing concentrations of NMDA (no inhibitors applied).

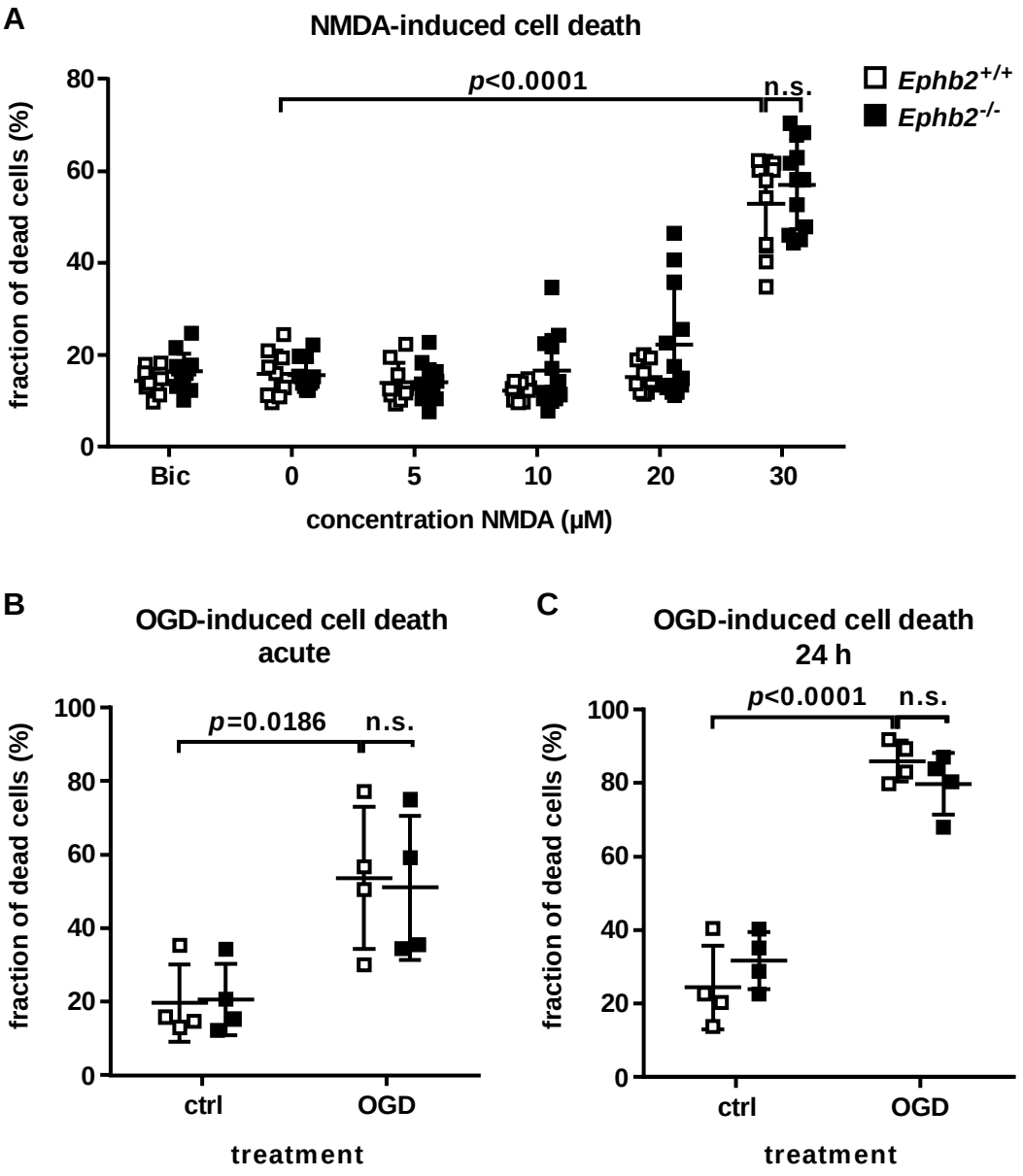

Figure 29: Neuronal cell death upon excitotoxic stimuli. *Ephb2*$^{+/+}$ and *EphB2*$^{-/-}$ forebrain neurons were obtained from P0 mice. **(A)** Cells were stimulated with Bicculin (Bic, as negative control) or different NMDA concentrations as indicated. Fraction of dead cells was determined 24 h after stimulation. N=10/8 cover slips from 4 independent preparations. **(B)** and **(C)** Cells were subjected to 3 h oxygen-glucose deprivation (OGD). Fraction of dead cells was determined immediately afterwards (B) or 24 h afterwards (C) and compared to control conditions (ctrl). N=4, data are presented as single values (scatter plots) combined with the mean±SD, Two-way ANOVA, n.s.=not significant.

The fraction of dead cell was determined 24 h later by automatic evaluation of nuclear morphology visualized by Hoechst staining. Although there was a successful induction of cell death at 30 µM NMDA, there was no difference between the two groups of neurons (Figure 29A). To mimic cerebral ischemia *in vitro*, cells were subjected to oxygen-glucose deprivation (OGD) for three hours. Control cells were incubated under the same conditions but with glucose and normal oxygen levels. Cells were either directly stained with Hoechst dye afterwards or reoxygenated in normal growth medium for another 24 h before staining with Hoechst. The fraction of dead cells was automatically determined as before according to the morphological appearance of the nuclei. There was sufficient induction of cell death already after 3 h of OGD. However, the levels of cell death did not differ between the two genotypes at any time point measured (Figure 29B).

Annotation regarding shared data usage

In accordance with the guidelines for animal welfare and implementation of the three Rs in experimental protocols, the following *in vivo* data were generated together with Laura-Inés Böhler and will also be found in her doctoral thesis:

- infarct and edema sizes Figure 8 and Figure 18
- neurological deficits Figure 9 and Figure 18
- cerebrovascular anatomy Figure 13
- endothelial permeability Figure 15A and B
- MRI scans Figure 16 and Figure 17
- raw data obtained from transcriptome analysis

5 Discussion

5.1 Progression of stroke is attenuated in *Ephb2*-deficient mice

According to the world health organization, stroke is the second most common cause of death worldwide and the primary cause of disability in adults in the Western world. Despite intensive research, the pathophysiological mechanisms are not fully understood, and no causative therapy is available. The current therapy in humans aims at fastest possible restoration of cerebral blood flow by drug-induced thrombolysis with tissue plasminogen activator or mechanical removal of the thrombus occluding the brain artery (Powers *et al*., 2018). In contrast to human ischemic strokes, animal stroke models, such as the MCAo in rodents, are reproducible, controllable and allow investigation of the molecular pathomechanisms especially during the first hours upon cerebral ischemia. The degree of the progression of stroke highly depends on the duration of the MCAo. The longer the rCBF is interrupted, the larger the final damage to the brain tissue becomes (Carmichael, 2005). It is suggested that the infarct volume increases until 24 h after MCAo followed by reperfusion and remains relatively stable until 7 days afterwards. During the first 6 h after MCAo, the infarct is limited to regions in the striatum. Therefore, the striatum is considered as infarct core. After 12 h, the whole striatum is infarcted and tissue damage becomes also visible in the cortex. Due to limited regenerative capacity tissue damage in the infarct core is unlikely to be salvageable at any time point later than 12 h after cerebral ischemia followed by immediate reperfusion as suggested by several studies (Clemens *et al*., 1998; Liu *et al*., 2009; Reglodi *et al*., 2000).

This study is the first one to show that the RTK EphB2 is involved in the early progression of stroke shedding further light on the molecular mechanism of EpB2-related stroke pathogenesis. In *Ephb2*-deficient mice, brain tissue injury and motoric impairments were clearly reduced 24 h upon MCAo confirming that the lack of EphB2 attenuates the progression of stroke. In line with the aforementioned facts, a time-course analysis revealed that infarct volumes of *Ephb2*-deficient mice were already reduced after 12 h of reperfusion when compared to *Ephb2*$^{+/+}$ mice. *Ephb2*$^{+/-}$ mice also developed less brain tissue injury and showed less impaired motoric skills when compared to *Ephb2*$^{+/+}$ mice indicating a gene-dose effect of EphB2 on stroke progression. While neuronal degeneration in the infarct core was not different between *Ephb2*$^{+/+}$ and *Ephb2*$^{-/-}$ mice, neuronal degeneration in the cortex was diminished in *Ephb2*-deficient mice indicating decreased spatial spread of cellular depolarization and subsequent neuronal cell death induction (Lee *et al*., 2000) in *Ephb2*$^{-/-}$ mice.

For the first time, this study shows that a member of the Eph/ephrin family influences the progression of stroke during the first 6 h. So far, studies mainly investigated the involvement of Eph or ephrin proteins during later phases upon stroke (24 h – 4 weeks). The later phases upon stroke are hallmarked by regenerative processes, such as angiogenesis and

neurogenesis (Ruan *et al*., 2015; Xiong *et al*., 2010). In this context, it was shown that the ligand ephrin-B2, which also interacts with EphB2 (Kullander and Klein, 2002), is involved in the restoration of the BBB and neurovascular repair mechanisms upon cerebral ischemia. Enhanced activation of ephrin-B2 improved neurovascular repair mechanisms by increased pericyte recruitment after MCAo. However, the authors suggested that this mechanism is mediated by the interaction of ephrin-B2 with EphB4 and that this interaction would influence the angiopoietins/Tie2 system in endothelial cells and pericytes (Ghori *et al*., 2017). In another study, it was shown that infarct volumes were increased in mice lacking the EphB-ligand ephrin-B3. Surprisingly, post-ischemic neurogenesis, which usually improves neurological function upon cerebral ischemia (Gonzalez *et al*., 2007; Ishibashi *et al*., 2007), was enhanced but could not contribute to functional recovery of these mice (Doeppner *et al*., 2011). Induction of post-ischemic neurogenesis is mediated by enhanced proliferation and migration of progenitor cells in the subventricular zone (Palma-Tortosa *et al*., 2017; Zhang *et al*., 2008). Conover and colleagues suggested that blockage of EphB2/ephrin-B signaling induces enhanced cell proliferation and disrupted neuroblast migration in the SVZ (Conover *et al*., 2000). Further, hypertensive stroke-prone rats treated with EphB2-Fc protein showed improved neurological function as well as enhanced cell proliferation in the SVZ 3 weeks after permanent MCAo. The authors claimed that the administration of EphB2-Fc blocks endogenous EphB2 signaling as it interacts with available ephrin-B ligands. The interruption of EphB2 signaling would lead to improved neurological functions after cerebral ischemia (Xing *et al*., 2008).

However, the suggested signaling processes in the previous studies are relevant only for later phases in the progression of stroke. In contrast, this study focused on the role of EphB2 especially during the first hours after cerebral ischemia. Interestingly, analysis of the phosphorylation of EphB2 revealed that EphB2 is activated already after 6 h of reperfusion in the ischemic hemisphere of *Ephb2*$^{+/+}$ mice. In addition to EphB2, the phosphorylation of 38 other RTKs, including Eph receptors, was analyzed. Though it was shown previously that the RTKs ErbB4 (Guan *et al*., 2015), MSPR (Suzuki *et al*., 2008), PDGFR alpha and beta (Ma *et al*., 2011; Renner *et al*., 2003), TrkA and TrkC (Chung *et al*., 2017; Lee *et al*., 1998) as well as VEGFR (Greenberg and Jin, 2013) are involved in the progression of brain injury, this is the first study to show that the phosphorylation of these RTKs is increased already in the first hours after cerebral ischemia. Further, EphB4 and EphB6 showed increased phosphorylation upon cerebral ischemia indicating that additional members of the EphB/ephrin-B system might be involved in the early phase upon stroke. In contrast, the phosphorylation level of EphA2 is not increased though it was shown previously in *Epha2*$^{-/-}$ mice that EphA2 contributes to neuronal cell death and BBB damage during stroke (Thundyil *et al*., 2013).

The result showing that infarct volumes were reduced after 12 h of MCAo in *Ephb2*-deficient mice and the increased phosphorylation of EphB2 6 h after MCAo suggested that EphB2 influences the progression of stroke in the early phase upon cerebral I/R injury.

5.2 BBB function and vascular phenotype in the brain are not altered in *Ephb2*-deficient mice

Alterations in the cerebrovascular anatomy due to the lack of EphB2 could compensate for the disturbed blood flow during the MCAo or the subsequent reperfusion thereby influencing the progression of stroke. So far, no studies were available regarding the cerebrovascular anatomy, capillary density, and pericyte coverage of brain vessels in *Ephb2*-deficient mice, though EphB2 and EphB2 ligands play a crucial role during vasculogenesis (Adams *et al*., 1999; Gerety and Anderson, 2002). However, this study revealed that the reduction in regional cerebral rCBF during MCAo was not altered in *Ephb2*-deficient mice. Further, cerebrovascular anatomy, capillary density, and pericyte coverage of brain vessels were comparable in *Ephb2*$^{+/+}$ and *Ephb2*$^{-/-}$ mice indicating that the attenuated progression of stroke cannot be explained by an altered cerebrovascular system. The expression of gene-products in contralateral (normoxic) hemispheres of mice subjected to MCAo was analyzed to investigate if *Ephb2*-deficient mice had an altered expression pattern of gene products related to the function of endothelial cells. Gene sets associated with the regulation of activation of endothelial cells were comparable between *Ephb2*$^{+/+}$ and *Ephb2*$^{-/-}$ mice. In conclusion, the decrease in the progression of stroke in *Ephb2*-deficient mice cannot be ascribed to an altered cerebrovascular anatomy or changes in transcripts related to the activation of endothelial cells.

A major complication in the clinical therapy of stroke is the treatment of the developing vasogenic edema which arises upon cerebral ischemia. Vasogenic edema evolves from an increase in the permeability of the BBB thereby allowing extravasation of fluid into the brain parenchyma (Gelderblom *et al*., 2009). Though *Ephb2*-deficient mice did not show alterations in the cerebrovascular anatomy, the function of endothelial cells in the BBB might be influenced by the lack of EphB2-mediated signaling. Important regulators of the stability of the BBB are tight junctional proteins which connect the endothelial cells in the BBB. Subtle endothelial cytoskeletal reorganization is already detectable almost immediately after I/R injury leading to slight increases in BBB permeability (Shi *et al*., 2016). Interestingly, the EphB/ephrin-B system was shown to affect endothelial permeability. Ephrin-B-mediated reverse signaling in endothelial cells, which can be induced by EphB2, influences the junctional integrity and pro-inflammatory differentiation of endothelial cells (Liu *et al*., 2014). Further, mice deficient for *Epha2* showed decreased BBB permeability upon MCAo and reduced infarct sizes to a similar extent as *Ephb2*-deficient mice in this study (Thundyil *et al*.,

2013). These aforementioned data suggested that BBB permeability could evolve to a lesser extent when EphB2-mediated signaling processes are absent. In this study, BBB hyperpermeability was analyzed by quantification of Evans Blue extravasation but was not different between *Ephb2*$^{+/+}$ and *Ephb2*$^{-/-}$ mice. As it was shown previously that EphB2 ligands interact with endothelial junctional proteins (Liu *et al*., 2014), next it was investigated if endothelial cytoskeletal reorganization might be diminished in the absence of EphB2. However, this study showed that the disassembly in endothelial tight junctions upon stroke was similar in both genotypes. Finally, edema formation was assessed by MRI, which allowed to distinguish vasogenic and cytotoxic edema formation (Barber *et al*., 2005; Rumpel *et al*., 1998). As mentioned before, vasogenic edema formation requires increased vascular permeability. In line with the previous data obtained from histological analyses in this study, vasogenic edema was smaller in *Ephb2*-deficient mice after 24 h of reperfusion. Though vasogenic edema formation can be monitored by T2-relaxometry already 90 min after I/R injury (Barber *et al*., 2005), there was no difference in vasogenic edema volume after 6 h of reperfusion between the two genotypes. The results from this study suggest that the loss of EphB2 and the absence of EphB2-mediated signaling does not affect the vascular component, such as endothelial permeability, during the progression of stroke. A possible explanation could be that EphB3 compensates for the loss of EphB2. Adams and colleagues showed before that mice deficient for either Ephb2 or Ephb3 do not exhibit vascular defects while in Ephb2/Ephb3 double mutants the embryonic vascular development was impaired (Adams *et al*., 1999).

In contrast to vasogenic edema, cytotoxic edema evolves from cytotoxic cell swelling which is independent of additional water influx into the brain parenchyma but a consequence of ion pump failure (Brouns and De Deyn, 2009). Unlike vasogenic edema, cytotoxic cell swelling differed already after 6 h of reperfusion in the infarction core between the two genotypes in this study. These data suggest that the lack of EphB2-mediated signaling attenuates the progression of stroke rather by limiting cytotoxic cell swelling during the first hours after stroke than by affecting the stability of the BBB. Consequently, vasogenic edema formation is indirectly attenuated in *Ephb2*-deficient mice. Cytotoxic cell swelling is driven by the depletion of ATP due to focal hypoperfusion and arises prior to vasogenic edema (Yan *et al*., 2015). Subsequently, the function of ion pumps fails and leads to a dysbalance in ion homeostasis. The increased ion influx is followed by water inflow thereby inducing cell swelling which can trigger cell death (Dirnagl *et al*., 1999). Astrocytes play a crucial role in the clearance of extracellular potassium ions and glutamate and are therefore susceptible to cell swelling caused by ion dysbalance. In addition to astrocytes, neuronal cells undergo swelling not only due to ion dysbalance but also because of hyperactivation of glutamate receptors, such as NMDA receptors (Choi and Rothman, 1990; Rossi *et al*., 2007; Wang and

Parpura, 2016). Though the main part of cytotoxic edema formation, which evolved to a lesser extent in *Ephb2*-deficient mice upon I/R injury (this study), supposedly is caused by astrocytic cell swelling, neurons are more susceptible to ischemia-induced cell swelling and death (Liang *et al*., 2007).

5.3 EphB2 promotes NMDA-triggered Ca^{2+} influx into mitochondria

So far, many studies have focused on the role of the neuronal NMDA receptor-mediated excitotoxicity as it represents one of the most relevant signaling mechanisms triggering cell death induced by ion dysbalance (Kalia *et al*., 2008a; Lai *et al*., 2011; Martin and Wang, 2010). The NMDA receptor is an important receptor in excitatory synaptic transmission by increasing Ca^{2+} influx into the postsynapse upon binding of glutamate and glycine. Many clinical trials targeting NMDA receptors during stroke failed, among others due to severe side effects as the NMDA receptor is of pivotal physiological importance (Kalia *et al*., 2008a; Lai *et al*., 2014).

Indeed, this study showed that NMDA-induced elevation of mitochondrial Ca^{2+} levels and membrane depolarization, which precede neuronal excitotoxicity, are reduced in *Ephb2*-deficient neurons. EphB2 was shown to influence NMDA receptor-mediated Ca^{2+} influx before (Takasu *et al*., 2002). A disturbed NMDA receptor-mediated signaling in *Ephb2*-deficient mice could lead to reduced neuronal cytotoxic cell swelling and subsequently to attenuation in the progression of stroke. The connection of disturbed NMDA receptor signaling and reduced infarct volume was already shown before in other studies. In mice and respective neuronal cultures treated with pertussis toxin or genetically altered mice, which are haploinsufficient for the NMDA receptor subunit NR2B, NMDA receptor signaling is impaired and brain damage is reduced (Tang *et al*., 2015; Tang *et al*., 2018). In the study presented here, basal mitochondrial Ca^{2+} levels differed between *Ephb2*$^{+/+}$ and *Ephb2*$^{-/-}$ neurons. This suggests that mitochondrial Ca^{2+} uptake is already reduced when extracellular Ca^{2+} influx depends on NMDA receptors without functional EphB2. In contrast to mitochondrial Ca^{2+} levels, changes in cytoplasmic Ca^{2+} levels in NMDA-stimulated neurons were surprisingly not differently regulated in *Ephb2*$^{-/-}$ neurons as compared to *Ephb2*$^{+/+}$ neurons. Cytoplasmic and mitochondrial Ca^{2+} responses upon NMDA stimulation usually show similar time courses (Peng and Greenamyre, 1998; Stanika *et al*., 2009b) or both parameters are altered as studies in genetically modified neurons have shown (Martorell-Riera *et al*., 2014; Qiu *et al*., 2013). However, Takasu *et al*. also observed that changes of cytoplasmic Ca^{2+} levels upon stimulation with glutamate occur also independently of EphB2: Overexpression of wildtype EphB2 or a construct of EphB2 lacking the cytoplasmic kinase domain in hippocampal neurons does not lead to different changes in cytoplasmic Ca^{2+} levels upon stimulation with glutamate. On the contrary, treatment with recombinant ephrin-B2 prior to

glutamate stimulation, which activates EphB2, increases cytoplasmic Ca^{2+} but only in neurons transfected with the wildtype EphB2 construct (Takasu *et al*., 2002). These data suggest that the mitochondria in *Ephb2*$^{-/-}$ neurons have a decreased NMDA receptor-dependent Ca^{2+} load. On the contrary, mitochondrial Ca^{2+} levels which are not solely regulated by NMDA receptor and cytoplasmic Ca^{2+} are similar in comparison to *Ephb2*$^{+/+}$ neurons.

Though mitochondria play a crucial role in buffering changes in Ca^{2+} levels upon stimulation by their capacity to take Ca^{2+} up, they are not considered as vast Ca^{2+} stores. Intracellular Ca^{2+} levels are tightly regulated at many sites of action. The majority is stored in the endoplasmic reticulum or is bound to cytosolic proteins. Typically, the concentration of free cytosolic Ca^{2+} is maintained at approximately 100 nM. During basal conditions, Ca^{2+} levels in mitochondria are usually also maintained at a constant level. Mitochondrial Ca^{2+} uptake is mediated by a Ca^{2+}-sensitive uniporter allowing a net influx of Ca^{2+} when cytoplasmic Ca^{2+} is elevated. Ca^{2+} release from mitochondria is mainly regulated by a Na^{+}/Ca^{2+} exchanger during recovery after stimulation (Duchen, 2000; Pivovarova and Andrews, 2010). In conclusion, a decreased mitochondrial Ca^{2+} load in *Ephb2*$^{-/-}$ neurons could compensate increases in cytoplasmic Ca^{2+} upon NMDA stimulation which would explain why cytoplasmic Ca^{2+} levels were not altered while the mitochondrial responses were still different.

Mitochondrial dysfunction including mitochondrial Ca^{2+} overload and mitochondrial membrane depolarization is a hallmark of NMDA receptor-induced neuronal cell death (Bading, 2017). Though NMDA receptor-mediated mitochondrial Ca^{2+} load was decreased in the absence of EphB2, it was not clear if the differences in mitochondrial Ca^{2+} levels would lead to differences which might result in an impaired mitochondrial function. This study showed that NMDA-evoked changes in mitochondrial membrane potential were less increased in *Ephb2*-deficient neurons compared to *Ephb2*$^{+/+}$ neurons at NMDA concentration which can lead to excitotoxicity. Ca^{2+} influx into mitochondria decreases the electrochemical gradient leading to reduced ATP synthesis and accumulation of intramitochondrial Ca^{2+}(Pivovarova and Andrews, 2010). Further, pro-apoptotic proteins are released, the protease calpain is activated and ROS production is increased (Pivovarova and Andrews, 2010). Together, these processes induce rapid necrotic, caspase-independent as well as caspase-dependent cell death (Niizuma *et al*., 2010; Zhan *et al*., 2001). In conclusion, the reduction in NMDA receptor-mediated Ca^{2+} load of mitochondria and subsequent membrane depolarization in *Ephb2*-deficient neurons suggests a dysfunction of NMDA receptor-mediated mitochondrial processes in the absence of EphB2. Against this background, it is tempting to speculate that the reduction in neuronal cell death upon cerebral ischemia in *Ephb2*-deficient mice is caused by a dysfunctional mitochondrial Ca^{2+} load of the NMDA receptor.

In addition to the observed altered mitochondrial Ca^{2+} load, an attenuation of NMDA receptor-mediated cell death induction in *Ephb2*-deficient neurons is supported by results

obtained from other studies. As mentioned before, the function of the NMDA receptor is influenced by several different factors. EphB2 has intensively been studied for its interaction with and functional impact on the glutamate receptor NMDA receptor. In addition to co-activators, the mechanism of action and subsequent downstream signaling of the NMDA receptor is influenced by its subunit composition as well as the localization of the receptor complex (Lai *et al*., 2011; Liu *et al*., 2007). Further, the overall development of excitatory synapses depends on the recruitment of NMDA receptor which is essential for synaptic plasticity (Cull-Candy *et al*., 2001). The interaction of the extracellular domains of EphB2 and the NR1 subunit of the NMDA receptor enables EphB2 to influence the localization and function of the NMDA receptor. Interestingly, extrasynaptic NMDA receptors are mainly composed of NR2B subunits and Nolt and colleagues showed that EphB2 is involved in directing NR2B to its designated target (Nolt *et al*., 2011). Activation of extrasynaptic NMDA receptors induces mitochondrial dysfunction and neuronal cell death, while activation of synaptic NMDA receptors rather drives neuroprotective pathways. It is suggested that extrasynaptic NMDA receptors are closer located to mitochondria than synaptic NMDA receptors. Additionally, the postsynaptic protein complexes could shield the mitochondria from NMDA receptor. Consequently, extrasynaptic mitochondria would be more directly exposed to calcium ions entering the cell through the NMDA receptor (Bading, 2017). The function of NMDA receptors is modified by EphB2 and in light of these facts, one could speculate that NMDA receptors in *Ephb2*-deficient neurons might be functionally impaired and incorrectly located. Both could lead to reduced Ca^{2+} influx through extrasynaptic NMDA receptors and a subsequent reduced Ca^{2+} load of mitochondria during cerebral ischemia resulting in reduced cell death induction.

5.4 Synaptic activity is altered in *Ephb2*-deficient neurons

Though the main function of both, synaptic and extrasynaptic NMDA receptors is the regulation of Ca^{2+} influx into the neuron, the subsequent signaling pathways differ. While the experiments so far involved activation of all forms of the NMDA receptor, the next experiments aimed mainly on the function of synaptic NMDA receptors. As mentioned before, synaptic NMDA receptors are involved in pro-survival pathways suggesting that alterations in this function could also influence neuronal survival. Synaptic activity was induced by the GABAa receptor antagonist gabazine. GABAergic neurons inhibit excitotoxic neurons thereby modulating synaptic activity in the CNS (Purves and Williams, 2001). Application of the GABAa receptor antagonist Bicuculline reverses the GABAergic inhibitory effect and leads to rapid AP spikes, called burst (AP burst). This enables Ca^{2+} influx through synaptic NMDA receptors which in turn triggers calcium-dependent activation of gene expression programs. In particular, the neuroprotective transcription factor CREB is activated upon

nuclear calcium signaling (Hardingham *et al*., 2001; Papadia *et al*., 2005). In this study, mitochondrial Ca^{2+} levels were not altered in *Ephb2*-deficient neurons during AP burst induced by the GABAa receptor antagonist gabazine. As this stimulation activates mainly synaptic NMDA receptors, this result is in line with the previous claim that activation of synaptic NMDA receptors alone is not involved in mitochondrial dysfunction (Zhou *et al*., 2013). Further, *Ephb2*-deficient neurons showed reduced elevated cytoplasmic Ca^{2+} levels during AP burst indicating reduced synaptic activity. This is in line with experiments of Grunwald and Henderson who demonstrated that *Ephb2*-deficient mice have defects in synaptic plasticity as the protein-synthesis required for long-term potentiation was defective (Grunwald *et al*., 2001; Henderson *et al*., 2001). Additionally, in this study gene sets associated with pathways involved in synaptic function and NMDA receptors were less activated in *Ephb2*-deficient contralateral (normoxic) brain hemispheres when compared to *Ephb2*$^{+/+}$ indicating impaired synaptic function in *Ephb2*-deficient mice. NMDA receptor-dependent synaptic dysfunction can be reversed by EphB2 overexpression in a murine Alzheimer model (Cissé *et al*., 2011) implying the diverse aspects of EphB2- and NMDA receptor-mediated signaling. This result seems to be contradictory to the previous results, which suggested that impaired NMDA receptor signaling is beneficial and would reduce excitotoxicity. The reduced synaptic activity would subsequently lead to a reduced induction of expression of neuroprotective gene programs. However, the dynamics of activation of either synaptic or extrasynaptic NMDA receptor or simultaneous activation of both kinds of NMDA receptor are still under debate. Zhou and colleagues suggested that the dose of NMDA applied to neurons also influences whether extrasynaptic or synaptic NMDA receptor are activated. They implied that high doses of NMDA, which would be equivalent to the massive glutamate concentrations present in the ischemic brain, preferably activate extrasynaptic NMDA receptors thereby triggering excitotoxic cell death. On the other hand, low doses would activate pro-survival gene programs through synaptic NMDA receptor. Importantly, though the toxic effect seems to be primarily regulated by activation of extrasynaptic NMDA receptors, activation of extrasynaptic NMDA receptors alone leads only to changes in Ca^{2+} transients but it does not induce detrimental dysregulation of Ca^{2+} homeostasis or cell death. Mitochondrial dysfunction and cell death induction seem to be dependent on the simultaneous activation of synaptic and extrasynaptic NMDA receptors (Hardingham *et al*., 2002; Zhou *et al*., 2013). Though synaptic responses are reduced in *Ephb2*-deficient neurons, both, synaptic and extrasynaptic NMDA receptors can still be activated. Therefore, NMDA receptor-mediated neuronal cell death induction is still possible in *Ephb2*-deficient neurons but could be attenuated.

Additional mechanistic insights might be gained from the analysis of a solely synaptic-driven NMDA receptor-protective function in *Ephb2*-deficient neurons. Lau and colleagues showed

that the neuroprotective mechanism of BDNF acts via initiating synaptic NMDA receptor-driven expression of inhibin β-A which subsequently reduces neurotoxic extrasynaptic NMDA receptor signaling. As *Ephb2*-deficient neurons show impairments in both, extrasynaptic and synaptic NMDA receptor signaling, the decrease in extrasynaptic NMDA receptor-mediated Ca^{2+} influx upon BDNF application should be reduced in *Ephb2*-deficient neurons when compared to *Ephb2*$^{+/+}$ neurons (Lau *et al*., 2015).

5.5 Excitotoxic neuronal cell death induction *in vitro* differs from cerebral ischemia-induced neuronal degeneration *in vivo*

The aforementioned results suggested that *Ephb2*-deficient neurons are less susceptible to NMDA receptor-mediated cell death induction. Therefore, the next experiments in this study focused on the detection of cell death levels after stimulation of the NMDA receptor or by exposure to OGD. However, in the chosen experimental setup, neither NMDA-stimulated nor OGD-challenged *Ephb2*-deficient neurons showed detectable differences in the fraction of dead cells as compared to *Ephb2*$^{+/+}$ neurons. It is important to take into consideration that the experimental setup used in the cell death assay was not comparable with the conditions used for the detection of mitochondrial Ca^{2+} levels upon NMDA stimulation. Mitochondrial Ca^{2+} levels were decreased in *Ephb2*-deficient neurons when the Ca^{2+} influx solely depended on the NMDA receptor but not if other Ca^{2+} channels were still active. The experimental setup for the detection of the fraction of dead cells, however, did not include inhibition of other voltage-dependent Ca^{2+} channels, AMPA receptors, or voltage-dependent sodium channels. Further, the differences in mitochondrial Ca^{2+} levels were detected almost immediately upon stimulation of the NMDA receptor while the detection of dead cells was performed more than 16 h later. During this time, calcium and glutamate released from dying neurons could potentiate excitotoxicity and activate further signaling processes. Therefore, the addition of NMDA to cultured neurons without inhibiting other Ca^{2+} channels is not comparable to the situation which led to differences in mitochondrial Ca^{2+} levels and mitochondrial membrane depolarization. Though neuronal degeneration was attenuated in *Ephb2*-deficient mice, it is likely that function and signaling processes of cultured neurons do not mirror the more complex situation *in vivo* which showed decreased neuronal cell death. Activation of the NMDA receptor during OGD is considered to trigger the main part of neuronal cell death induction. However, Aarts and colleagues demonstrated an NMDA-independent cell death mechanism during prolonged OGD. Cell death induction in cortical neurons subjected to 1 h of OGD followed by approximately 24 h of re-oxygenation was almost completely inhibited when the glutamate receptor (NMDA receptors, AMPA receptors, and kainate receptors) antagonists were applied. In the presence of a specific NMDA receptor antagonist, cell death levels were greatly reduced after 1 h of OGD. After 1.5 h, the levels

of cell death were still reduced when an NMDA receptor antagonist was present but to reach a similar reduction as after 1 h, AMPA and kainite receptors had to be also blocked. When OGD was extended to 2 h, the antagonists failed to reduce the fraction of cell death (Aarts *et al*., 2003). Hence, the chosen setup for cell death induction by OGD in this study (3 h) did not solely aim at NMDA receptor-mediated cell death induction. Therefore, future experiments should be conducted by specifically targeting the NMDA receptor-mediated cell death signaling process and should further rule out that released molecules of dying neurons induce further NMDA receptor-independent cell death processes.

5.6 Involvement of EphB2 ligands in brain injury models

In addition to the altered function of NMDA receptors at the post-synapse, further EphB2-dependent signaling mechanisms might be altered in *Ephb2*-deficient mice. Though many studies have been dealing with the questions about localization and function of members of the EphB/ephrin-B family, many questions remain open. The expression pattern of EphB receptors and ephrin-B ligands in the CNS is diverse and complex (Hruska and Dalva, 2012; Kania and Klein, 2016; Klein, 2009; Pasquale, 2008). Further, the interaction of EphB and ephrin-B induces signaling processes in both cells, the EphB and the ephrin-B-expressing cell. Immunofluorescence staining techniques applied on cryo-sections of *Ephb2*$^{+/+}$ and *Ephb2*$^{-/-}$ mice subjected to cerebral ischemia showed similar expression patterns of EphB2 ligands (visualized after 6 h of reperfusion prior to any substantial loss of cells) as well as similar loss of the ephrin-B-specific signal outside of vessel-like structures after 24 h of reperfusion. Importantly, the association of EphB2 with the NMDA receptor is driven by interaction with EphB2 ligands, such as ephrin-B1 and -B2. Further, it was shown that the EphB2-mediated modulation of NMDA receptor function requires activation of EphB2 by ephrin-B (Dalva *et al*., 2000; Takasu *et al*., 2002). Post-synaptic EphB2 could be activated by pre-synaptic ephrin-B1/2/3 during cerebral ischemia. However, activation of EphB2 can also occur by ephrin-B present on non-neuronal cells. For example, astrocytes are in physical contact with neurons and are involved in several neuronal functions. They contribute to ion homeostasis by potassium or glutamate release (Bellot-Saez *et al*., 2017). Further, they participate in neuronal development and have even been shown to regulate memory formation and synaptic plasticity (Ota *et al*., 2013; Pál, 2015; Pirttimaki *et al*., 2017). Astrocytic ephrin-B1 modulates remodeling of synapses upon traumatic brain injury as shown by the acceleration of the recovery of glutamatergic synapses in astrocytic-specific ablation of ephrin-B1 (Nikolakopoulou *et al*., 2016). In contrast to the results in this study, which showed reduced cell death in the absence of EphB2-mediated signaling, activation of neuronal EphB1-mediated signaling triggers neuroprotective pathways via interaction with astrocytic ephrin-B1 (Tyzack *et al*., 2017). Further, Bundesen and colleagues suggested that

astrocytic ephrin-B2 regulates glial scar formation by interaction with EphB2 on fibroblasts upon spinal cord injury (Bundesen *et al*., 2003) indicating that further steps during the progression of stroke could additionally be influenced in *Ephb2*-deficient mice. Analysis of mice with a CNS cell-specific deletion of *Ephrinb2* showed decreased infarct and edema volume upon MCAo followed by 24 h of reperfusion (unpublished data) indicating that ephrin-B2 is also important during the acute phase of stroke. Further, astrocytes derived from *Ephb2*-deficient mice showed reduced pro-inflammatory activation upon stimulation with recombinant EphB2 protein in cell culture experiments. Interestingly, stimulation of WT astrocytes with EphB2 promotes translocation of nuclear factor kappa B (NF-kB) into the nucleus (see PhD thesis Laura-Inés Böhler). The lack of EphB2 could additionally affect the inflammatory response of the resident cells in the brain, such as astrocytes and microglia, by diminishing EphB2-induced ephrin-B reverse signaling thereby further attenuating brain tissue damage.

5.7 Proposed model of EphB2-dependent NMDA receptor-mediated excitotoxicity

Taken together, this study showed that EphB2 contributes to the formation of cytotoxic edema during the first hours after cerebral stroke which is independent of BBB breakdown. Further, *Ephb2*-deficient neurons reacted differently upon NMDA receptor stimulation as the mitochondrial Ca^{2+} levels and membrane depolarization were decreased. Importantly, these parameters are involved in mediating NMDA receptor-induced excitotoxicity. Based on these results and previous findings it is proposed that EphB2 is involved in neuronal cell death induction after hyperactivation of NMDA receptor during cerebral ischemia. In the absence of EphB2, detrimental Ca^{2+} influx through (extra-)synaptic NMDA receptors is impaired

The extracellular domain of EphB2 interacts with the NMDA receptor subunit NR1 upon interaction with ephrin-B (shown by Grunwald *et al*. 2001; Takasu *et al*. 2002)). The NMDA receptor is stimulated by excessive glutamate during cerebral ischemia (Dingledine *et al*., 1999). Src family kinases are recruited by the intracellular domain of EphB2 and interact with the cytoplasmic tail of the NMDA receptor and induce phosphorylation of the NR2B subunit at tyrosine residue 1472 (Antion *et al*., 2010; Brückner and Klein, 1998; Takasu *et al*., 2002). Ca^{2+} influx through the NMDA receptor increases and triggers signaling cascades promoting neuronal cell death which would be attenuated in *Ephb2*-deficient neurons.

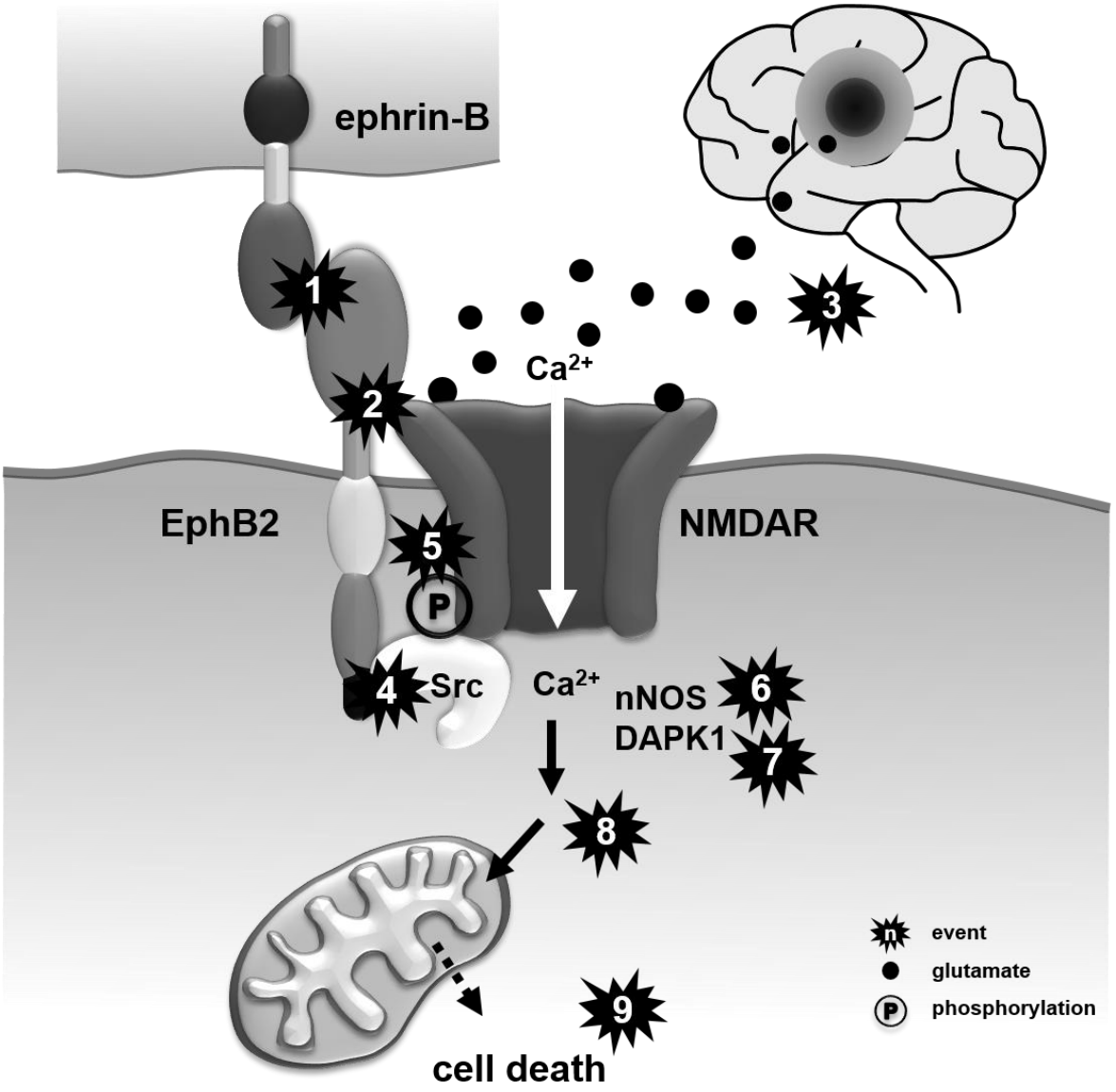

Figure 30: Scheme depicting the proposed mechanism of EphB2-mediated neuronal excitotoxicity. The membrane-bound RTK EphB2 is activated by a membrane-bound ephrin-B ligand (event 1). Next, the extracellular domain of EphB2 interacts with the NR1 subunit of the NMDA receptor (NMDAR) (event 2,) which is overstimulated during cerebral ischemia by excessive glutamate (event 3). The intracellular domain of EphB2 recruits members of the Src family kinases (event 4), which subsequently induce phosphorylation (Ⓟ) of the NMDA receptor subunit NR2B (event 5), and Ca^{2+} influx through the NMDA receptor increases. Then, nNOS is activated (event 6) and DAPK1 recruited inducing further signaling events (event 7). The increase in intracellular Ca^{2+} is buffered by mitochondria as they take up Ca^{2+} (event 8). This leads to mitochondrial membrane depolarization, activation of pro-apoptotic factors and mitochondrial dysfunction and finally cumulates in cell death induction (event 9). In the absence of EphB2, glutamate-induced NMDA receptor signaling during cerebral ischemia is impaired and cell death induction is decreased (results this study). Glutamate is represented by black dots.

Ca^{2+} influx through the NMDA receptor leads to activation of CaM which in turn activates neuronal nitric oxide synthase (nNOS). Activation of nNOS leads to ROS formation. Neuronal NOS is coupled via the post-synaptic density protein 95 (PSD-95) to the NMDA receptor and disruption of the PSD-95-nNOS complex leads to decreased infarct sizes in mice subjected to MCAo (Zhou *et al*., 2010). Another consequence of NMDA receptor activation during ischemia is the recruitment of DAPK1 which further was shown to promote neuronal excitotoxicity (Tu *et al*., 2010). NMDA receptor signaling further includes the activation of MAP kinases, such as the c-Jun N-terminal kinase (JNK). Inhibition of JNKs is also neuroprotective during cerebral ischemia (Borsello *et al*., 2003; Esneault *et al*., 2008). In addition to the interruption of the NMDA receptor signaling processes, the localization, and composition of NMDA receptors in *Ephb2*-deficient neurons could be altered (Nolt *et al*., 2011) and would make these neurons less susceptible to NMDA receptor-mediated cell death induction. Figure 30 illustrates the proposed mechanism. A similar mechanism was already suggested by Yuferov and colleagues who showed that high expression of EphB2 correlates with increased cognitive impairments in HIV-positive patients (Yuferov *et al*., 2013).

It remains a challenging question how NMDA receptor-mediated cell death induction during stroke can be interrupted without interfering with the physiological requirement of proper NMDA receptor function in human patients. This study suggests that detrimental Ca^{2+} influx through extrasynaptic NMDA receptor is modulated by EphB2. Targeting EphB2 in this context could reduce this Ca^{2+} influx. In this way, the function of the NMDA receptor would be partially maintained but neuronal cell death induction could be reduced.

6 Appendix

Table 8 Transcriptome analysis of *Ephb2*$^{+/+}$ mice after stroke. *Ephb2*$^{+/+}$ mice were subjected to 60 min middle cerebral artery occlusion (MCAo) followed by 48 h of reperfusion. DNA microarray and gene set enrichment analysis of the ipsi- and contralateral hemispheres showed differentially regulated pathways (obtained from KEGG database). N=3. Only pathways showing NES >1.5 or <-1.5, *p*<0.05 and FDR<0.1 were included. NES=normalized enrichment score, FDR=false discovery rate

Pathway	NES	*p* value	FDR
Staphylococcus aureus infection	2.49	<0.001	<0.001
Leishmaniasis	2.49	<0.001	<0.001
Complement and coagulation cascades	2.46	<0.001	<0.001
ECM-receptor interaction	2.46	<0.001	<0.001
Focal adhesion	2.41	<0.001	<0.001
Osteoclast differentiation	2.38	<0.001	<0.001
Cytokine-cytokine receptor interaction	2.37	<0.001	<0.001
Phagosome	2.37	<0.001	<0.001
Toxoplasmosis	2.35	<0.001	<0.001
Pertussis	2.34	<0.001	<0.001
Tuberculosis	2.33	<0.001	<0.001
Leukocyte transendothelial migration	2.31	<0.001	<0.001
Proteoglycans in cancer	2.28	<0.001	<0.001
Hematopoietic cell lineage	2.27	<0.001	<0.001
Chagas disease (American trypanosomiasis)	2.27	<0.001	<0.001
B cell receptor signaling pathway	2.25	<0.001	<0.001
Toll-like receptor signaling pathway	2.23	<0.001	<0.001
Influenza A	2.23	<0.001	<0.001
Measles	2.22	<0.001	<0.001
Malaria	2.20	<0.001	<0.001
Pancreatic cancer	2.19	<0.001	<0.001
TNF signaling pathway	2.19	<0.001	<0.001
Jak-STAT signaling pathway	2.19	<0.001	<0.001
NF-kappa B signaling pathway	2.19	<0.001	<0.001
Rheumatoid arthritis	2.18	<0.001	<0.001
Apoptosis	2.17	<0.001	<0.001
Antigen processing and presentation	2.17	<0.001	<0.001
Inflammatory bowel disease (IBD)	2.17	<0.001	<0.001
Hepatitis B	2.16	<0.001	<0.001
Herpes simplex infection	2.12	<0.001	<0.001
Amoebiasis	2.11	<0.001	<0.001
Salmonella infection	2.11	<0.001	<0.001
Small cell lung cancer	2.11	<0.001	<0.001
HIF-1 signaling pathway	2.11	<0.001	<0.001
PI3K-Akt signaling pathway	2.09	<0.001	<0.001
Transcriptional misregulation in cancer	2.09	<0.001	<0.001
p53 signaling pathway	2.06	<0.001	<0.001
Cell cycle	2.06	<0.001	<0.001
Lysosome	2.06	<0.001	<0.001
HTLV-I infection	2.05	<0.001	<0.001
Epstein-Barr virus infection	2.05	<0.001	<0.001
Natural killer cell mediated cytotoxicity	2.05	<0.001	<0.001
Legionellosis	2.04	<0.001	<0.001
Viral myocarditis	2.03	<0.001	<0.001
Asthma	2.00	<0.001	<0.001
Chemokine signaling pathway	1.98	<0.001	<0.001
Graft-versus-host disease	1.98	<0.001	<0.001
Systemic lupus erythematosus	1.97	<0.001	<0.001
Bacterial invasion of epithelial cells	1.97	<0.001	<0.001
Fc gamma R-mediated phagocytosis	1.97	<0.001	<0.001
DNA replication	1.96	<0.001	<0.001
Viral carcinogenesis	1.95	<0.001	<0.001
Mineral absorption	1.94	<0.001	<0.001
MicroRNAs in cancer	1.94	<0.001	<0.001
Chronic myeloid leukemia	1.94	0.002	<0.001

Proteasome	1.91	<0.001	0.001
Fc epsilon RI signaling pathway	1.91	<0.001	0.001
Hepatitis C	1.90	<0.001	0.001
Regulation of actin cytoskeleton	1.90	<0.001	0.001
Protein processing in endoplasmic reticulum	1.88	<0.001	0.001
Cell adhesion molecules (CAMs)	1.86	<0.001	0.001
Intestinal immune network for IgA production	1.85	<0.001	0.001
Allograft rejection	1.85	<0.001	0.002
Prion diseases	1.84	<0.001	0.002
Platelet activation	1.83	<0.001	0.002
Acute myeloid leukemia	1.82	0.002	0.002
NOD-like receptor signaling pathway	1.79	<0.001	0.003
Prostate cancer	1.79	<0.001	0.003
Sphingolipid signaling pathway	1.79	<0.001	0.003
Pathways in cancer	1.79	<0.001	0.003
TGF-beta signaling pathway	1.78	0.002	0.004
Autoimmune thyroid disease	1.75	<0.001	0.006
Cytosolic DNA-sensing pathway	1.75	<0.001	0.006
Colorectal cancer	1.74	0.002	0.006
T cell receptor signaling pathway	1.74	0.002	0.006
VEGF signaling pathway	1.74	0.002	0.006
Type I diabetes mellitus	1.74	0.004	0.006
Glioma	1.74	<0.001	0.007
Steroid biosynthesis	1.73	0.015	0.007
Glycosaminoglycan degradation	1.72	0.008	0.008
Spliceosome	1.70	<0.001	0.009
MAPK signaling pathway	1.67	<0.001	0.012
Porphyrin and chlorophyll metabolism	1.67	0.014	0.012
Adherens junction	1.67	0.002	0.013
Bladder cancer	1.66	0.005	0.014
Renal cell carcinoma	1.65	0.007	0.015
FoxO signaling pathway	1.64	0.002	0.016
Non-alcoholic fatty liver disease (NAFLD)	1.61	0.002	0.021
Melanoma	1.61	0.006	0.021
Protein digestion and absorption	1.60	0.011	0.022
RIG-I-like receptor signaling pathway	1.59	0.003	0.024
Pentose and glucuronate interconversions	1.58	0.024	0.028
Hypertrophic cardiomyopathy (HCM)	1.55	0.008	0.034
Adipocytokine signaling pathway	1.55	0.015	0.035
Prolactin signaling pathway	1.54	0.013	0.038
Endocytosis	1.53	<0.001	0.039
One carbon pool by folate	1.53	0.039	0.038
Primary bile acid biosynthesis	1.50	0.071	0.049
Hippo signaling pathway	1.50	0.005	0.050
Rap1 signaling pathway	1.50	0.005	0.050
Dopaminergic synapse	-1.50	0.006	0.081
Amphetamine addiction	-1.59	0.005	0.036
Glycosaminoglycan biosynthesis - HS/Hep	-1.63	0.006	0.028
Neuroactive ligand-receptor interaction	-1.67	<0.001	0.019
Calcium signaling pathway	-1.69	<0.001	0.018
GABAergic synapse	-1.71	<0.001	0.016
Circadian entrainment	-1.73	<0.001	0.014
Parkinson's disease	-1.73	<0.001	0.015
Retrograde endocannabinoid signaling	-1.76	<0.001	0.013
Glutamatergic synapse	-1.83	<0.001	0.006
Cocaine addiction	-1.86	<0.001	0.004
Morphine addiction	-1.94	<0.001	0.002
Nicotine addiction	-2.24	<0.001	<0.001

Table 9: Comparison of transcriptomes of *Ephb2*$^{+/+}$ and *Ephb2*$^{-/-}$ mice upon stroke. Mice were subjected to 60 min middle cerebral artery occlusion (MCAo) followed by 48 h of reperfusion. DNA microarray and gene set enrichment analysis of the ipsilateral hemispheres showed differentially regulated pathways (obtained from KEGG database). N=3. Only pathways showing NES >1.5 or <-1.5, p<0.05 and FDR<0.1 were included. NES=normalized enrichment score, FDR=false discovery rate

Pathway	NES	*p* value	FDR
ECM-receptor interaction	-2.46	<0.001	<0.001
Focal adhesion	-2.29	<0.001	<0.001
Small cell lung cancer	-2.27	<0.001	<0.001
Cytokine-cytokine receptor interaction	-2.23	<0.001	<0.001
Toxoplasmosis	-2.22	<0.001	<0.001
NF-kappa B signaling pathway	-2.20	<0.001	<0.001
TNF signaling pathway	-2.17	<0.001	<0.001
Complement and coagulation cascades	-2.16	<0.001	<0.001
Leukocyte transendothelial migration	-2.15	<0.001	<0.001
p53 signaling pathway	-2.13	<0.001	<0.001
Proteoglycans in cancer	-2.12	<0.001	<0.001
Leishmaniasis	-2.11	<0.001	<0.001
HIF-1 signaling pathway	-2.08	<0.001	<0.001
B cell receptor signaling pathway	-2.07	<0.001	<0.001
Osteoclast differentiation	-2.07	<0.001	<0.001
Legionellosis	-2.06	<0.001	<0.001
Staphylococcus aureus infection	-2.06	<0.001	<0.001
Malaria	-2.06	<0.001	<0.001
Pertussis	-2.05	<0.001	<0.001
Antigen processing and presentation	-2.00	<0.001	0.001
Amoebiasis	-2.00	<0.001	0.001
Rheumatoid arthritis	-2.00	<0.001	0.001
Apoptosis	-2.00	<0.001	0.001
Proteasome	-1.98	<0.001	0.001
PI3K-Akt signaling pathway	-1.97	<0.001	0.001
Jak-STAT signaling pathway	-1.97	<0.001	0.001
Toll-like receptor signaling pathway	-1.97	<0.001	0.001
Hematopoietic cell lineage	-1.96	<0.001	0.001
Chagas disease (American trypanosomiasis)	-1.94	<0.001	0.001
Tuberculosis	-1.93	<0.001	0.001
Phagosome	-1.93	<0.001	0.001
Spliceosome	-1.92	<0.001	0.001
Influenza A	-1.88	<0.001	0.002
Epstein-Barr virus infection	-1.87	<0.001	0.002
VEGF signaling pathway	-1.87	<0.001	0.002
Protein processing in endoplasmic reticulum	-1.87	<0.001	0.002
Salmonella infection	-1.85	0.002	0.002
Hepatitis B	-1.85	<0.001	0.002
MicroRNAs in cancer	-1.84	<0.001	0.003
Prostate cancer	-1.84	<0.001	0.003
Chronic myeloid leukemia	-1.82	<0.001	0.003
FoxO signaling pathway	-1.80	<0.001	0.004
HTLV-I infection	-1.79	<0.001	0.004
Fc gamma R-mediated phagocytosis	-1.79	<0.001	0.005
Pancreatic cancer	-1.78	<0.001	0.005
Measles	-1.77	<0.001	0.006
Arginine and proline metabolism	-1.77	<0.001	0.005
Chemokine signaling pathway	-1.76	<0.001	0.006
Cell cycle	-1.76	<0.001	0.006
Bacterial invasion of epithelial cells	-1.75	0.002	0.007
Regulation of actin cytoskeleton	-1.74	<0.001	0.007
Glioma	-1.74	<0.001	0.007
Natural killer cell mediated cytotoxicity	-1.74	<0.001	0.007
Transcriptional misregulation in cancer	-1.74	<0.001	0.007
Fc epsilon RI signaling pathway	-1.74	<0.001	0.007
Estrogen signaling pathway	-1.72	<0.001	0.008
Protein digestion and absorption	-1.72	<0.001	0.008

Biosynthesis of amino acids	-1.69	<0.001	0.011
Hepatitis C	-1.68	<0.001	0.012
Pathways in cancer	-1.67	<0.001	0.013
MAPK signaling pathway	-1.67	<0.001	0.013
Sphingolipid signaling pathway	-1.65	<0.001	0.015
Acute myeloid leukemia	-1.64	0.011	0.017
Mineral absorption	-1.63	0.008	0.018
Adipocytokine signaling pathway	-1.63	0.002	0.018
Galactose metabolism	-1.63	0.011	0.019
Bladder cancer	-1.62	0.011	0.020
Melanoma	-1.61	0.007	0.021
Viral myocarditis	-1.61	0.002	0.021
Herpes simplex infection	-1.60	0.002	0.022
Cell adhesion molecules (CAMs)	-1.58	0.002	0.027
Non-alcoholic fatty liver disease (NAFLD)	-1.56	0.002	0.029
Colorectal cancer	-1.55	0.009	0.031
NOD-like receptor signaling pathway	-1.55	0.011	0.031
DNA replication	-1.55	0.026	0.031
Inflammatory bowel disease (IBD)	-1.55	0.018	0.031
Prolactin signaling pathway	-1.54	0.007	0.036
TGF-beta signaling pathway	-1.53	0.014	0.036
Hypertrophic cardiomyopathy (HCM)	-1.51	0.012	0.043
One carbon pool by folate	-1.50	0.042	0.046
Choline metabolism in cancer	-1.50	0.003	0.046
Central carbon metabolism in cancer	-1.50	0.020	0.047
Platelet activation	-1.50	0.003	0.048
Dopaminergic synapse	1.51	0.005	0.082
Parkinson's disease	1.53	0.002	0.079
Neuroactive ligand-receptor interaction	1.55	<0.001	0.072
Salivary secretion	1.56	0.002	0.070
Cocaine addiction	1.73	0.004	0.015
Calcium signaling pathway	1.77	<0.001	0.011
Circadian entrainment	1.78	<0.001	0.010
Axon guidance	1.83	<0.001	0.007
GABAergic synapse	1.87	<0.001	0.005
Retrograde endocannabinoid signaling	1.97	<0.001	0.001
Morphine addiction	2.03	<0.001	0.001
Glutamatergic synapse	2.08	<0.001	0.001
Nicotine addiction	2.41	<0.001	<0.001

Table 10. Comparison of transcriptomes of normoxic brain tissue from *Ephb2*$^{+/+}$ and *Ephb2*$^{-/-}$ mice. Mice were subjected to 60 min middle cerebral artery occlusion (MCAo) followed by 48 h of reperfusion. DNA microarray and gene set enrichment analysis of the contralateral hemispheres showed differentially regulated pathways (obtained from KEGG database). N=3. Only pathways showing NES >1.5 or <-1.5, p<0.05 and FDR<0.1 were included. NES=normalized enrichment score, FDR=false discovery rate

Pathway	NES	*p* value	FDR
Nicotine addiction	2.02	<0.001	0.004
Long-term potentiation	1.87	<0.001	0.023
Glutamatergic synapse	1.83	<0.001	0.023
Retrograde endocannabinoid signaling	1.77	<0.001	0.042
Long-term depression	1.69	0.008	0.075
Osteoclast differentiation	-1.50	0.004	0.088
Hepatitis B	-1.50	<0.001	0.089
Central carbon metabolism in cancer	-1.51	0.017	0.090
Fatty acid elongation	-1.51	0.044	0.090
2-Oxocarboxylic acid metabolism	-1.54	0.032	0.074
Arginine and proline metabolism	-1.54	0.016	0.073
Tryptophan metabolism	-1.55	0.024	0.072
Chronic myeloid leukemia	-1.55	0.008	0.074
Adipocytokine signaling pathway	-1.55	0.010	0.072
Epstein-Barr virus infection	-1.56	0.002	0.073
Parkinson's disease	-1.57	0.005	0.067
Fatty acid degradation	-1.58	0.009	0.065
Non-alcoholic fatty liver disease (NAFLD)	-1.60	<0.001	0.055
Selenocompound metabolism	-1.62	0.015	0.051
Notch signaling pathway	-1.63	0.011	0.044
beta-Alanine metabolism	-1.64	0.010	0.045
Ribosome	-1.64	0.004	0.046
Fructose and mannose metabolism	-1.65	0.008	0.043
Other types of O-glycan biosynthesis	-1.66	0.010	0.042
Drug metabolism - cytochrome P450	-1.68	<0.001	0.036
Purine metabolism	-1.69	<0.001	0.035
Valine, leucine and isoleucine degradation	-1.69	0.002	0.036
Pertussis	-1.70	0.002	0.036
Nitrogen metabolism	-1.70	0.016	0.036
Chemical carcinogenesis	-1.72	<0.001	0.031
Sphingolipid metabolism	-1.73	0.002	0.028
Other glycan degradation	-1.74	0.006	0.031
Small cell lung cancer	-1.75	<0.001	0.029
Biosynthesis of amino acids	-1.81	0.002	0.014
Metabolism of xenobiotics by cytochrome P450	-1.85	<0.001	0.010
Glycosaminoglycan degradation	-1.91	<0.001	0.005
Lysosome	-1.98	<0.001	0.002
Pyrimidine metabolism	-2.00	<0.001	0.003
Complement and coagulation cascades	-2.01	<0.001	0.002
Staphylococcus aureus infection	-2.13	<0.001	0.001
RNA polymerase	-2.14	0.002	0.001
Glutathione metabolism	-2.38	<0.001	<0.001

7 References

Aarts, M., Iihara, K., Wei, W.-L., Xiong, Z.-G., Arundine, M., Cerwinski, W., MacDonald, J.F., and Tymianski, M. (2003). A key role for TRPM7 channels in anoxic neuronal death. Cell *115*, 863–877.

Adams, R.H., Wilkinson, G. a., Weiss, C., Diella, F., Gale, N.W., Deutsch, U., Risau, W., and Klein, R. (1999). Roles of ephrinB ligands and EphB receptors in cardiovascular development: Demarcation of arterial/venous domains, vascular morphogenesis, and sprouting angiogenesis. Genes Dev. *13*, 295–306.

Aloisi, F. (2001). Immune function of microglia. Glia *36*, 165–179.

Antion, M.D., Christie, L.A., Bond, A.M., Dalva, M.B., and Contractor, A. (2010). Ephrin-B3 regulates glutamate receptor signaling at hippocampal synapses. Mol. Cell. Neurosci. *45*, 378–388.

Bading, H. (2017). Therapeutic targeting of the pathological triad of extrasynaptic NMDA receptor signaling in neurodegenerations. J. Exp. Med. jem.20161673.

Bading, H., and Greenberg, M.E. (1991). Stimulation of protein tyrosine phosphorylation by NMDA receptor activation. Science *253*, 912–914.

Bading, H., Ginty, D.D., and Greenberg, M.E. (1993). Regulation of gene expression in hippocampal neurons by distinct calcium signaling pathways. Science *260*, 181–186.

Baeten, K.M., and Akassoglou, K. (2011). Extracellular matrix and matrix receptors in blood-brain barrier formation and stroke. Dev. Neurobiol. *71*, 1018–1039.

Baracca, A., Sgarbi, G., Solaini, G., and Lenaz, G. (2003). Rhodamine 123 as a probe of mitochondrial membrane potential: evaluation of proton flux through F(0) during ATP synthesis. Biochim. Biophys. Acta *1606*, 137–146.

Barber, P.A., Hoyte, L., Kirk, D., Foniok, T., Buchan, A., and Tuor, U. (2005). Early T1- and T2-weighted MRI signatures of transient and permanent middle cerebral artery occlusion in a murine stroke model studied at 9.4T. Neurosci. Lett. *388*, 54–59.

Barteczek, P., Li, L., Ernst, A.S., Böhler, L.I., Marti, H.H., and Kunze, R. (2017). Neuronal HIF-1α and HIF-2α deficiency improves neuronal survival and sensorimotor function in the early acute phase after ischemic stroke. J. Cereb. Blood Flow Metab. *37*, 291–306.

Becker, N., Seitanidou, T., Murphy, P., Mattéi, M.-G., Topilko, P., Nieto, M.A., Wilkinson, D.G., Charnay, P., and Gilardi-Hebenstreit, P. (1994). Several receptor tyrosine kinase genes of the Eph family are segmentally expressed in the developing hindbrain. Mech. Dev. *47*, 3–17.

Bellot-Saez, A., Kékesi, O., Morley, J.W., and Buskila, Y. (2017). Astrocytic modulation of neuronal excitability through K+ spatial buffering. Neurosci. Biobehav. Rev. *77*, 87–97.

Bochenek, M.L., Dickinson, S., Astin, J.W., Adams, R.H., and Nobes, C.D. (2010). Ephrin-B2 regulates endothelial cell morphology and motility independently of Eph-receptor binding. J. Cell Sci. *123*, 1235–1246.

Borsello, T., Clarke, P.G.H., Hirt, L., Vercelli, A., Repici, M., Schorderet, D.F., Bogousslavsky, J., and Bonny, C. (2003). A peptide inhibitor of c-Jun N-terminal kinase protects against excitotoxicity and cerebral ischemia. Nat. Med. *9*, 1180–1186.

Braun, J., Hoffmann, S.C., Feldner, A., Ludwig, T., Henning, R., Hecker, M., and Korff, T. (2011). Endothelial cell EphrinB2-dependent activation of monocytes in arteriosclerosis. Arterioscler. Thromb. Vasc. Biol. *31*, 297–305.

Brouns, R., and De Deyn, P.P. (2009). The complexity of neurobiological processes in acute ischemic stroke. Clin. Neurol. Neurosurg. *111*, 483–495.

Brückner, K., and Klein, R. (1998). Signaling by Eph receptors and their ephrin ligands.

Curr. Opin. Neurobiol. *8*, 375–382.

Bundesen, L.Q., Scheel, T.A., Bregman, B.S., and Kromer, L.F. (2003). Ephrin-B2 and EphB2 regulation of astrocyte-meningeal fibroblast interactions in response to spinal cord lesions in adult rats. J. Neurosci. *23*, 7789–7800.

Carmichael, S.T. (2005). Rodent models of focal stroke: size, mechanism, and purpose. NeuroRx *2*, 396–409.

Choi, D.W., and Rothman, S.M. (1990). The Role of Glutamate Neurotoxicity in Hypoxic-Ischemic Neuronal Death. Annu. Rev. Neurosci. *13*, 171–182.

Chukkapalli, S., Amessou, M., Dilly, A.K., Dekhil, H., Zhao, J., Liu, Q., Bejna, A., Thomas, R.D., Bandyopadhyay, S., Bismar, T.A., et al. (2014). Role of the EphB2 receptor in autophagy, apoptosis and invasion in human breast cancer cells. Exp. Cell Res. *320*, 233–246.

Chung, J.-Y., Kim, M.-W., Im, W., Hwang, I.K., Bang, M.-S., and Kim, M. (2017). Expression of Neurotrophin-3 and trkC following Focal Cerebral Ischemia in Adult Rat Brain with Treadmill Exercise. Biomed Res. Int. *2017*, 9248542.

Cipolla, M.J. (2009). Control of Cerebral Blood Flow.

Cissé, M., Halabisky, B., Harris, J., Devidze, N., Dubal, D.B., Sun, B., Orr, A., Lotz, G., Kim, D.H., Hamto, P., et al. (2011). Reversing EphB2 depletion rescues cognitive functions in Alzheimer model. Nature *469*, 47–52.

Clemens, J.A., Stephenson, D.T., Yin, T., Smalstig, E.B., Panetta, J.A., and Little, S.P. (1998). Drug-induced neuroprotection from global ischemia is associated with prevention of persistent but not transient activation of nuclear factor-kappaB in rats. Stroke *29*, 677–682.

Conover, J.C., Doetsch, F., Garcia-Verdugo, J.M., Gale, N.W., Yancopoulos, G.D., and Alvarez-Buylla, A. (2000). Disruption of Eph/ephrin signaling affects migration and proliferation in the adult subventricular zone. Nat. Neurosci. *3*, 1091–1097.

Cooke, J.E., Kemp, H.A., and Moens, C.B. (2005). EphA4 is required for cell adhesion and rhombomere-boundary formation in the zebrafish. Curr. Biol. *15*, 536–542.

Cowan, C.A., and Henkemeyer, M. (2001). The SH2/SH3 adaptor Grb4 transduces B-ephrin reverse signals. Nature *413*, 174–179.

Cull-Candy, S., Brickley, S., and Farrant, M. (2001). NMDA receptor subunits: diversity, development and disease. Curr. Opin. Neurobiol. *11*, 327–335.

Daar, I.O. (2012). Non-SH2/PDZ reverse signaling by ephrins. Semin. Cell Dev. Biol. *23*, 65–74.

Dalva, M.B. (2010). Ephecting excitatory synapse development. Cell *143*, 341–342.

Dalva, M.B., Takasu, M. a, Lin, M.Z., Shamah, S.M., Hu, L., Gale, N.W., and Greenberg, M.E. (2000). EphB receptors interact with NMDA receptors and regulate excitatory synapse formation. Cell *103*, 945–956.

Dick, O., and Bading, H. (2010). Synaptic activity and nuclear calcium signaling protect hippocampal neurons from death signal-associated nuclear translocation of FoxO3a induced by extrasynaptic N-methyl-D-aspartate receptors. J. Biol. Chem. *285*, 19354–19361.

Dingledine, R., Borges, K., Bowie, D., and Traynelis, S.F. (1999). The glutamate receptor ion channels. Pharmacol.Rev. *51*, 7–61.

Dirnagl, U., Iadecola, C., and Moskowitz, M. a (1999). Pathobiology of ischaemic stroke: an integrated view. 4441. Trends Neurosci. *22*, 391–397.

Doeppner, T.R., Bretschneider, E., Doehring, M., Segura, I., Sentürk, A., Acker-Palmer, A., Hasan, M.R., Elali, A., Hermann, D.M., and Bähr, M. (2011). Enhancement of endogenous neurogenesis in ephrin-B3 deficient mice after transient focal cerebral ischemia. Acta

Neuropathol. *122*, 429–442.

Doyle, K.P., Simon, R.P., and Stenzel-Poore, M.P. (2008). Mechanisms of ischemic brain damage. Neuropharmacology *55*, 310–318.

Duchen, M.R. (2000). Mitochondria and calcium: from cell signalling to cell death. J. Physiol. *529 Pt 1*, 57–68.

Dugan, L.L., Sensi, S.L., Canzoniero, L.M., Handran, S.D., Rothman, S.M., Lin, T.S., Goldberg, M.P., and Choi, D.W. (1995). Mitochondrial production of reactive oxygen species in cortical neurons following exposure to N-methyl-D-aspartate. J. Neurosci. *15*, 6377–6388.

Esneault, E., Castagne, V., Moser, P., Bonny, C., and Bernaudin, M. (2008). D-JNKi, a peptide inhibitor of c-Jun N-terminal kinase, promotes functional recovery after transient focal cerebral ischemia in rats. Neuroscience *152*, 308–320.

Ethell, I.M., Irie, F., Kalo, M.S., Couchman, J.R., Pasquale, E.B., and Yamaguchi, Y. (2001). EphB/syndecan-2 signaling in dendritic spine morphogenesis. Neuron *31*, 1001–1013.

Fogal, B., Trettel, J., Uliasz, T.F., Levine, E.S., and Hewett, S.J. (2005). Changes in secondary glutamate release underlie the developmental regulation of excitotoxic neuronal cell death. Neuroscience *132*, 929–942.

Foo, S.S., Turner, C.J., Adams, S., Compagni, A., Aubyn, D., Kogata, N., Lindblom, P., Shani, M., Zicha, D., and Adams, R.H. (2006). Ephrin-B2 controls cell motility and adhesion during blood-vessel-wall assembly. Cell *124*, 161–173.

Fujikawa, D.G. (2015). The Role of Excitotoxic Programmed Necrosis in Acute Brain Injury. Comput. Struct. Biotechnol. J. *13*, 212–221.

Gelderblom, M., Leypoldt, F., Steinbach, K., Behrens, D., Choe, C.U., Siler, D. a., Arumugam, T. V., Orthey, E., Gerloff, C., Tolosa, E., et al. (2009). Temporal and spatial dynamics of cerebral immune cell accumulation in stroke. Stroke *40*, 1849–1857.

Gerety, S.S., and Anderson, D.J. (2002). Cardiovascular ephrinB2 function is essential for embryonic angiogenesis. Development *129*, 1397–1410.

Gerety, S.S., Wang, H.U., Chen, Z.F., and Anderson, D.J. (1999). Symmetrical mutant phenotypes of the receptor EphB4 and its specific transmembrane ligand ephrin-B2 in cardiovascular development. Mol. Cell *4*, 403–414.

Gerriets, T., Walberer, M., Ritschel, N., Tschernatsch, M., Mueller, C., Bachmann, G., Schoenburg, M., Kaps, M., and Nedelmann, M. (2009). Edema formation in the hyperacute phase of ischemic stroke. J. Neurosurg. *111*, 1036–1042.

Gerrow, K. (2006). Cell adhesion molecules at the synapse. Front. Biosci. *11*, 2400.

Ghori, A., Freimann, F.B., Nieminen-Kehl??, M., Kremenetskaia, I., Gertz, K., Endres, M., and Vajkoczy, P. (2017). EphrinB2 Activation Enhances Vascular Repair Mechanisms and Reduces Brain Swelling After Mild Cerebral Ischemia. Arterioscler. Thromb. Vasc. Biol.

Ginhoux, F., Lim, S., Hoeffel, G., Low, D., and Huber, T. (2013). Origin and differentiation of microglia. Front. Cell. Neurosci. *7*, 45.

Gonzalez, F.F., McQuillen, P., Mu, D., Chang, Y., Wendland, M., Vexler, Z., and Ferriero, D.M. (2007). Erythropoietin enhances long-term neuroprotection and neurogenesis in neonatal stroke. Dev. Neurosci. *29*, 321–330.

Greenberg, D.A., and Jin, K. (2013). Vascular endothelial growth factors (VEGFs) and stroke. Cell. Mol. Life Sci. *70*, 1753–1761.

Greer, P.L., and Greenberg, M.E. (2008). From synapse to nucleus: calcium-dependent gene transcription in the control of synapse development and function. Neuron *59*, 846–860.

Grunwald, I.C., Korte, M., Wolfer, D., Wilkinson, G. a., Unsicker, K., Lipp, H.P., Bonhoeffer, T., and Klein, R. (2001). Kinase-independent requirement of EphB2 receptors in

hippocampal synaptic plasticity. Neuron *32*, 1027–1040.

Guan, Y.-F., Wu, C.-Y., Fang, Y.-Y., Zeng, Y.-N., Luo, Z.-Y., Li, S.-J., Li, X.-W., Zhu, X.-H., Mei, L., and Gao, T.-M. (2015). Neuregulin 1 protects against ischemic brain injury via ErbB4 receptors by increasing GABAergic transmission. Neuroscience *307*, 151–159.

Guruswamy, R., and ElAli, A. (2017). Complex Roles of Microglial Cells in Ischemic Stroke Pathobiology: New Insights and Future Directions. Int. J. Mol. Sci. *18*.

Hardingham, G.E., and Bading, H. (2010). Synaptic versus extrasynaptic NMDA receptor signalling: implications for neurodegenerative disorders. Nat. Rev. Neurosci. *11*, 682–696.

Hardingham, G.E., Arnold, F.J.L., and Bading, H. (2001). Nuclear calcium signaling controls CREB-mediated gene expression triggered by synaptic activity. Nat. Neurosci. *4*, 261–267.

Hardingham, G.E., Fukunaga, Y., and Bading, H. (2002). Extrasynaptic NMDARs oppose synaptic NMDARs by triggering CREB shut-off and cell death pathways. Nat. Neurosci. *5*, 405–414.

Henderson, J.T., Georgiou, J., Jia, Z., Robertson, J., Elowe, S., Roder, J.C., and Pawson, T. (2001). The receptor tyrosine kinase EphB2 regulates NMDA-dependent synaptic function. Neuron *32*, 1041–1056.

Henkemeyer, M., Orioli, D., Henderson, J.T., Saxton, T.M., Roder, J., Pawson, T., and Klein, R. (1996). Nuk controls pathfinding of commissural axons in the mammalian central nervous system. Cell *86*, 35–46.

Henkemeyer, M., Itkis, O.S., Ngo, M., Hickmott, P.W., and Ethell, I.M. (2003). Multiple EphB receptor tyrosine kinases shape dendritic spines in the hippocampus. J. Cell Biol. *163*, 1313–1326.

Henninger, N., Küppers-Tiedt, L., Sicard, K.M., Günther, A., Schneider, D., and Schwab, S. (2006). Neuroprotective effect of hyperbaric oxygen therapy monitored by MR-imaging after embolic stroke in rats. Exp. Neurol. *201*, 316–323.

Hindges, R., McLaughlin, T., Genoud, N., Henkemeyer, M., and O'Leary, D.D.M. (2002). EphB forward signaling controls directional branch extension and arborization required for dorsal-ventral retinotopic mapping. Neuron *35*, 475–487.

Holen, H.L., Shadidi, M., Narvhus, K., Kjøsnes, O., Tierens, A., and Aasheim, H.-C. (2008). Signaling through ephrin-A ligand leads to activation of Src-family kinases, Akt phosphorylation, and inhibition of antigen receptor-induced apoptosis. J. Leukoc. Biol. *84*, 1183–1191.

Hruska, M., and Dalva, M.B. (2012). Ephrin regulation of synapse formation, function and plasticity. Mol. Cell. Neurosci. *50*, 35–44.

Husa, A.-M., Magić, Ž., Larsson, M., Fornander, T., and Pérez-Tenorio, G. (2016). EPH/ephrin profile and EPHB2 expression predicts patient survival in breast cancer. Oncotarget *7*, 21362–21380.

Irie, F., Okuno, M., Pasquale, E.B., and Yamaguchi, Y. (2005). EphrinB–EphB signalling regulates clathrin-mediated endocytosis through tyrosine phosphorylation of synaptojanin 1. Nat. Cell Biol. *7*, 501–509.

Ishibashi, S., Kuroiwa, T., Sakaguchi, M., Sun, L., Kadoya, T., Okano, H., and Mizusawa, H. (2007). Galectin-1 regulates neurogenesis in the subventricular zone and promotes functional recovery after stroke. Exp. Neurol. *207*, 302–313.

Jahn, R., and Scheller, R.H. (2006). SNAREs — engines for membrane fusion. Nat. Rev. Mol. Cell Biol. *7*, 631–643.

Jain, V., Langham, M.C., and Wehrli, F.W. (2010). MRI estimation of global brain oxygen consumption rate. J. Cereb. Blood Flow Metab. *30*, 1598–1607.

Jin, X. (2016). The role of neurogenesis during development and in the adult brain. Eur. J.

Neurosci. *44*, 2291–2299.

Kalia, L. V., Kalia, S.K., and Salter, M.W. (2008a). NMDA receptors in clinical neurology: excitatory times ahead. Lancet Neurol. *7*, 742–755.

Kalia, L. V, Kalia, S.K., Salter, M.W., Pinheiro, P., Mulle, C., Dingledine, R., Borges, K., Bowie, D., Traynelis, S., Paoletti, P., et al. (2008b). NMDA receptors in clinical neurology: excitatory times ahead. Lancet. Neurol. *7*, 742–755.

Kania, A., and Klein, R. (2016). Mechanisms of ephrin–Eph signalling in development, physiology and disease. Nat. Rev. Mol. Cell Biol.

Kayser, M.S., McClelland, A.C., Hughes, E.G., and Dalva, M.B. (2006). Intracellular and trans-synaptic regulation of glutamatergic synaptogenesis by EphB receptors. J. Neurosci. *26*, 12152–12164.

Klein, R. (2009). Bidirectional modulation of synaptic functions by Eph/ephrin signaling. Nat. Neurosci. *12*, 15–20.

Klein, R. (2012). Eph/ephrin signalling during development. Development *139*, 4105–4109.

Knox, R., and Jiang, X. (2015). Fyn in Neurodevelopment and Ischemic Brain Injury. Dev. Neurosci. *37*, 311–320.

Korff, T., Braun, J., Pfaff, D., Augustin, H.G., and Hecker, M. (2008). Role of ephrinB2 expression in endothelial cells during arteriogenesis: Impact on smooth muscle cell migration and monocyte recruitment. Blood *112*, 73–81.

Kullander, K., and Klein, R. (2002). Mechanisms and functions of Eph and ephrin signalling. Nat. Rev. Mol. Cell Biol. *3*, 475–486.

Kunze, R., Urrutia, A., Hoffmann, A., Liu, H., Helluy, X., Pham, M., Reischl, S., Korff, T., and Marti, H.H. (2015). Dimethyl fumarate attenuates cerebral edema formation by protecting the blood-brain barrier integrity. Exp. Neurol. *266*, 99–111.

Lai, T.W., Shyu, W.C., and Wang, Y.T. (2011). Stroke intervention pathways: NMDA receptors and beyond. Trends Mol. Med. *17*, 266–275.

Lai, T.W., Zhang, S., and Wang, Y.T. (2014). Excitotoxicity and stroke: Identifying novel targets for neuroprotection. Prog. Neurobiol. *115*, 157–188.

Lau, D., Bengtson, C.P., Buchthal, B., and Bading, H. (2015). BDNF Reduces Toxic Extrasynaptic NMDA Receptor Signaling via Synaptic NMDA Receptors and Nuclear-Calcium-Induced Transcription of inhba/Activin A. Cell Rep. *12*, 1353–1366.

Lee, J.M., Grabb, M.C., Zipfel, G.J., and Choi, D.W. (2000). Brain tissue responses to ischemia. J. Clin. Invest. *106*, 723–731.

Lee, T.H., Kato, H., Chen, S.T., Kogure, K., and Itoyama, Y. (1998). Expression of nerve growth factor and trkA after transient focal cerebral ischemia in rats. Stroke *29*, 1687–96; discussion 1697.

Li, L., Saliba, P., Reischl, S., Marti, H.H., and Kunze, R. (2016). Neuronal deficiency of HIF prolyl 4-hydroxylase 2 in mice improves ischemic stroke recovery in an HIF dependent manner. Neurobiol. Dis. *91*, 221–235.

Liang, D., Bhatta, S., Gerzanich, V., and Simard, J.M. (2007). Cytotoxic edema: mechanisms of pathological cell swelling. Neurosurg. Focus *22*, 1–9.

Lisabeth, E.M., Falivelli, G., and Pasquale, E.B. (2013). Eph receptor signaling and ephrins. Cold Spring Harb. Perspect. Biol. *5*.

Liu, F., Schafer, D.P., and McCullough, L.D. (2009). TTC, Fluoro-Jade B and NeuN staining confirm evolving phases of infarction induced by middle cerebral artery occlusion. J. Neurosci. Methods *179*, 1–8.

Liu, H., Devraj, K., Möller, K., Liebner, S., Hecker, M., and Korff, T. (2014). EphrinB-mediated reverse signalling controls junctional integrity and pro-inflammatory differentiation

of endothelial cells. Thromb. Haemost. *112*, 151–163.

Liu, X., Hawkes, E., Ishimaru, T., Tran, T., and Sretavan, D.W. (2006). EphB3: an endogenous mediator of adult axonal plasticity and regrowth after CNS injury. J. Neurosci. *26*, 3087–3101.

Liu, Y., Wong, T.P., Aarts, M., Rooyakkers, A., Liu, L., Lai, T.W., Wu, D.C., Lu, J., Tymianski, M., Craig, A.M., et al. (2007). Neurobiology of Disease NMDA Receptor Subunits Have Differential Roles in Mediating Excitotoxic Neuronal Death Both In Vitro and In Vivo. *27*, 2846–2857.

Lucas, F.R., and Salinas, P.C. (1997). WNT-7a Induces Axonal Remodeling and Increases Synapsin I Levels in Cerebellar Neurons. Dev. Biol. *192*, 31–44.

Luo, H., Yu, G., Tremblay, J., and Wu, J. (2004). EphB6-null mutation results in compromised T cell function. J. Clin. Invest. *114*, 1762–1773.

Ma, Q., Huang, B., Khatibi, N., Rolland, W., Suzuki, H., Zhang, J.H., Tang, J., and Tang, J. (2011). PDGFR-α inhibition preserves blood-brain barrier after intracerebral hemorrhage. Ann. Neurol. *70*, 920–931.

Mabuchi, T., Kitagawa, K., Kuwabara, K., Takasawa, K., Ohtsuki, T., Xia, Z., Storm, D., Yanagihara, T., Hori, M., and Matsumoto, M. (2001). Phosphorylation of cAMP response element-binding protein in hippocampal neurons as a protective response after exposure to glutamate in vitro and ischemia in vivo. J. Neurosci. *21*, 9204–9213.

Marti, H.J., Bernaudin, M., Bellail, a, Schoch, H., Euler, M., Petit, E., and Risau, W. (2000). Hypoxia-induced vascular endothelial growth factor expression precedes neovascularization after cerebral ischemia. Am. J. Pathol. *156*, 965–976.

Martin, H.G.S., and Wang, Y.T. (2010). Blocking the Deadly Effects of the NMDA Receptor in Stroke. Cell *140*, 174–176.

Martorell-Riera, A., Segarra-Mondejar, M., Muñoz, J.P., Ginet, V., Olloquequi, J., Pérez-Clausell, J., Palacín, M., Reina, M., Puyal, J., Zorzano, A., et al. (2014). Mfn2 downregulation in excitotoxicity causes mitochondrial dysfunction and delayed neuronal death. EMBO J. *33*, 2388–2407.

Meyer, L.A.T., Kaselis, A., Satkauskas, S., and Bagnard, D. (2017). Analysis of Semaphorin-Induced Growth Cone Collapse and Axon Growth Inhibition. (Humana Press, New York, NY), pp. 171–183.

Nakayama, M., Nakayama, A., van Lessen, M., Yamamoto, H., Hoffmann, S., Drexler, H.C.A., Itoh, N., Hirose, T., Breier, G., Vestweber, D., et al. (2013). Spatial regulation of VEGF receptor endocytosis in angiogenesis. Nat. Cell Biol. *15*, 249–260.

Nakazawa, T., Komai, S., Tezuka, T., Hisatsune, C., Umemori, H., Semba, K., Mishina, M., Manabe, T., and Yamamoto, T. (2001). Characterization of Fyn-mediated Tyrosine Phosphorylation Sites on GluRε2 (NR2B) Subunit of the *N* -Methyl-d-aspartate Receptor. J. Biol. Chem. *276*, 693–699.

Nave, K.-A. (2010). Myelination and support of axonal integrity by glia. Nature *468*, 244–252.

Niizuma, K., Yoshioka, H., Chen, H., Kim, G.S., Jung, J.E., Katsu, M., Okami, N., and Chan, P.H. (2010). Mitochondrial and apoptotic neuronal death signaling pathways in cerebral ischemia. Biochim. Biophys. Acta *1802*, 92–99.

Nikolakopoulou, A.M., Koeppen, J., Garcia, M., Leish, J., Obenaus, A., and Ethell, I.M. (2016). Astrocytic Ephrin-B1 Regulates Synapse Remodeling Following Traumatic Brain Injury. ASN Neuro *8*.

Nolt, M.J., Lin, Y., Hruska, M., Murphy, J., Sheffler-Colins, S.I., Kayser, M.S., Passer, J., Bennett, M.V.L., Zukin, R.S., and Dalva, M.B. (2011). EphB Controls NMDA Receptor Function and Synaptic Targeting in a Subunit-Specific Manner. J. Neurosci. *31*, 5353–5364.

Nomenclature, U., and Ligands, T. (1997). Unified nomenclature for Eph family receptors and their ligands, the ephrins. Eph Nomenclature Committee. Cell *90*, 403–404.

Nour, M., Scalzo, F., and Liebeskind, D.S. (2013). Ischemia-reperfusion injury in stroke. Interv. Neurol. *1*, 185–199.

Orioli, D., Henkemeyer, M., Lemke, G., Klein, R., and Pawson, T. (1996). Sek4 and Nuk receptors cooperate in guidance of commissural axons and in palate formation. EMBO J. *15*, 6035–6049.

Ota, Y., Zanetti, A.T., and Hallock, R.M. (2013). The role of astrocytes in the regulation of synaptic plasticity and memory formation. Neural Plast. *2013*, 185463.

Pál, B. (2015). Astrocytic Actions on Extrasynaptic Neuronal Currents. Front. Cell. Neurosci. *9*, 474.

Palma-Tortosa, S., García-Culebras, A., Moraga, A., Hurtado, O., Perez-Ruiz, A., Durán-Laforet, V., Parra, J. de la, Cuartero, M.I., Pradillo, J.M., Moro, M.A., et al. (2017). Specific Features of SVZ Neurogenesis After Cortical Ischemia: a Longitudinal Study. Sci. Rep. *7*, 16343.

Palmer, A.E., and Tsien, R.Y. (2006). Measuring calcium signaling using genetically targetable fluorescent indicators. Nat. Protoc. *1*, 1057–1065.

Palmer, A., Zimmer, M., Erdmann, K.S., Eulenburg, V., Porthin, A., Heumann, R., Deutsch, U., and Klein, R. (2002). EphrinB phosphorylation and reverse signaling: regulation by Src kinases and PTP-BL phosphatase. Mol. Cell *9*, 725–737.

Papadia, S., Stevenson, P., Hardingham, N.R., Bading, H., and Hardingham, G.E. (2005). Nuclear Ca2+ and the cAMP response element-binding protein family mediate a late phase of activity-dependent neuroprotection. J. Neurosci. *25*, 4279–4287.

Pasquale, E.B. (2008). Eph-Ephrin Bidirectional Signaling in Physiology and Disease. Cell *133*, 38–52.

Paulson, O.B., Strandgaard, S., and Edvinsson, L. (1990). Cerebral autoregulation. Cerebrovasc. Brain Metab. Rev. *2*, 161–192.

Peng, T.I., and Greenamyre, J.T. (1998). Privileged access to mitochondria of calcium influx through N-methyl-D-aspartate receptors. Mol. Pharmacol. *53*, 974–980.

Pfaff, D., Héroult, M., Riedel, M., Reiss, Y., Kirmse, R., Ludwig, T., Korff, T., Hecker, M., and Augustin, H.G. (2008). Involvement of endothelial ephrin-B2 in adhesion and transmigration of EphB-receptor-expressing monocytes. J. Cell Sci. *121*, 3842–3850.

Pirttimaki, T.M., Sims, R.E., Saunders, G., Antonio, S.A., Codadu, N.K., and Parri, H.R. (2017). Astrocyte-Mediated Neuronal Synchronization Properties Revealed by False Gliotransmitter Release. J. Neurosci. *37*, 9859–9870.

Pitulescu, M.E., and Adams, R.H. (2010). Eph/ephrin molecules--a hub for signaling and endocytosis. Genes Dev. *24*, 2480–2492.

Pivovarova, N.B., and Andrews, S.B. (2010). Calcium-dependent mitochondrial function and dysfunction in neurons. FEBS J. *277*, 3622–3636.

Powers, W.J., Rabinstein, A.A., Ackerson, T., Adeoye, O.M., Bambakidis, N.C., Becker, K., Biller, J., Brown, M., Demaerschalk, B.M., Hoh, B., et al. (2018). 2018 Guidelines for the Early Management of Patients With Acute Ischemic Stroke: A Guideline for Healthcare Professionals From the American Heart Association/American Stroke Association. Stroke *49*, e46–e110.

Purves, D., and Williams, S.M. (Stephen M. (2001). Neuroscience (Sinauer Associates).

Qiu, J., Tan, Y.-W., Hagenston, A.M., Martel, M.-A., Kneisel, N., Skehel, P.A., Wyllie, D.J.A., Bading, H., and Hardingham, G.E. (2013). Mitochondrial calcium uniporter Mcu controls excitotoxicity and is transcriptionally repressed by neuroprotective nuclear calcium signals.

Nat. Commun. *4*, 2034.

Reglodi, D., Somogyvari-Vigh, A., Vigh, S., Kozicz, T., and Arimura, A. (2000). Delayed systemic administration of PACAP38 is neuroprotective in transient middle cerebral artery occlusion in the rat. Stroke *31*, 1411–1417.

Reischl, S., Li, L., Walkinshaw, G., Flippin, L.A., Marti, H.H., and Kunze, R. (2014). Inhibition of HIF prolyl-4-hydroxylases by FG-4497 reduces brain tissue injury and edema formation during ischemic stroke. PLoS One *9*.

Renner, O., Tsimpas, A., Kostin, S., Valable, S., Petit, E., Schaper, W., and Marti, H.H. (2003). Time- and cell type-specific induction of platelet-derived growth factor receptor-β during cerebral ischemia. Mol. Brain Res. *113*, 44–51.

Rossi, D.J., Brady, J.D., and Mohr, C. (2007). Astrocyte metabolism and signaling during brain ischemia. Nat. Neurosci. *10*, 1377–1386.

Ruan, L., Wang, B., ZhuGe, Q., and Jin, K. (2015). Coupling of neurogenesis and angiogenesis after ischemic stroke. Brain Res. *1623*, 166–173.

Rumpel, H., Ferrini, B., and Martin, E. (1998). Lasting cytotoxic edema as an indicator of irreversible brain damage: a case of neonatal stroke. AJNR. Am. J. Neuroradiol. *19*, 1636–1638.

Salvucci, O., and Tosato, G. (2012). Essential Roles of EphB Receptors and EphrinB Ligands in Endothelial Cell Function and Angiogenesis.

San Miguel, S., Serrano, M.J., Sachar, A., Henkemeyer, M., Svoboda, K.K.H., and Benson, M.D. (2011). Ephrin reverse signaling controls palate fusion via a PI3 kinase-dependent mechanism. Dev. Dyn. *240*, 357–364.

Sandoval, K.E., and Witt, K. a. (2008). Blood-brain barrier tight junction permeability and ischemic stroke. Neurobiol. Dis. *32*, 200–219.

Sattler, R., and Tymianski, M. (2001). Molecular Mechanisms of Glutamate Receptor-Mediated Excitotoxic Neuronal Cell Death. Mol. Neurobiol. *24*, 107–130.

Sawamiphak, S., Seidel, S., Essmann, C.L., Wilkinson, G. a, Pitulescu, M.E., Acker, T., and Acker-Palmer, A. (2010). Ephrin-B2 regulates VEGFR2 function in developmental and tumour angiogenesis. Nature *465*, 487–491.

Scheiffele, P. (2003). C ELL -C ELL S IGNALING D URING S YNAPSE F ORMATION IN THE CNS. Annu. Rev. Neurosci. *26*, 485–508.

Schmued, L.C., and Hopkins, K.J. (2000). Fluoro-Jade B: A high affinity fluorescent marker for the localization of neuronal degeneration. Brain Res. *874*, 123–130.

Sheffler-Collins, S.I., and Dalva, M.B. (2012). EphBs: an integral link between synaptic function and synaptopathies. Trends Neurosci. *35*, 293–304.

Shi, Y., Zhang, L., Pu, H., Mao, L., Hu, X., Jiang, X., Xu, N., Stetler, R.A., Zhang, F., Liu, X., et al. (2016). Rapid endothelial cytoskeletal reorganization enables early blood–brain barrier disruption and long-term ischaemic reperfusion brain injury. Nat. Commun. *7*, 10523.

Shimada, M., and Langman, J. (1970). Cell proliferation, migration and differentiation in the cerebral cortex of the golden hamster. J. Comp. Neurol. *139*, 227–243.

Shin, Y.-J., Choi, J.-S., Choi, J.-Y., Hou, Y., Cha, J.-H., Chun, M.-H., and Lee, M.-Y. (2010). Induction of vascular endothelial growth factor receptor-3 mRNA in glial cells following focal cerebral ischemia in rats. J. Neuroimmunol. *229*, 81–90.

Shu, S., Pei, L., and Lu, Y. (2014). Promising targets of cell death signaling of NR2B receptor subunit in stroke pathogenesis. Regen. Med. Res. *2*, 8.

Sofroniew, M. V, and Vinters, H. V (2010). Astrocytes: biology and pathology. Acta Neuropathol. *119*, 7–35.

Stanika, R.I., Pivovarova, N.B., Brantner, C.A., Watts, C.A., Winters, C.A., and Andrews,

S.B. (2009a). Coupling diverse routes of calcium entry to mitochondrial dysfunction and glutamate excitotoxicity. Proc. Natl. Acad. Sci. U. S. A. *106*, 9854–9859.

Stanika, R.I., Pivovarova, N.B., Brantner, C.A., Watts, C.A., Winters, C.A., and Andrews, S.B. (2009b). Coupling diverse routes of calcium entry to mitochondrial dysfunction and glutamate excitotoxicity. Proc. Natl. Acad. Sci. U. S. A. *106*, 9854–9859.

Suzuki, Y., Funakoshi, H., Machide, M., Matsumoto, K., and Nakamura, T. (2008). Regulation of cell migration and cytokine production by HGF-like protein (HLP) / macrophage stimulating protein (MSP) in primary microglia. Biomed. Res. *29*, 77–84.

Takasu, M.A. (2002). Modulation of NMDA Receptor- Dependent Calcium Influx and Gene Expression Through EphB Receptors. Science (80-.). *295*, 491–495.

Takasu, M.A., Dalva, M.B., Zigmond, R.E., and Greenberg, M.E. (2002). Modulation of NMDA receptor-dependent calcium influx and gene expression through EphB receptors. Science *295*, 491–495.

Tang, N., Wu, J., Zhu, H., Yan, H., Guo, Y., Cai, Y., Yan, H., Shi, Y., Shu, S., Pei, L., et al. (2018). Genetic Mutation of GluN2B Protects Brain Cells Against Stroke Damages. Mol. Neurobiol. *55*, 2979–2990.

Tang, Z., Li, S., Han, P., Yin, J., Gan, Y., Liu, Q., Wang, J., Wang, C., Li, Y., and Shi, J. (2015). Pertussis toxin reduces calcium influx to protect ischemic stroke in a middle cerebral artery occlusion model. J. Neurochem. *135*, 998–1006.

Thakar, S., Chenaux, G., and Henkemeyer, M. (2011). Critical roles for EphB and ephrin-B bidirectional signalling in retinocollicular mapping. Nat. Commun. *2*, 431.

Thundyil, J., Manzanero, S., Pavlovski, D., Cully, T.R., Lok, K.-Z., Widiapradja, A., Chunduri, P., Jo, D.-G., Naruse, C., Asano, M., et al. (2013). Evidence that the EphA2 receptor exacerbates ischemic brain injury. PLoS One *8*, e53528.

Tu, W., Xu, X., Peng, L., Zhong, X., Zhang, W., Soundarapandian, M.M., Balel, C., Wang, M., Jia, N., Zhang, W., et al. (2010). DAPK1 Interaction with NMDA Receptor NR2B Subunits Mediates Brain Damage in Stroke. Cell *140*, 222–234.

Tyzack, G.E., Hall, C.E., Sibley, C.R., Cymes, T., Forostyak, S., Carlino, G., Meyer, I.F., Schiavo, G., Zhang, S.-C., Gibbons, G.M., et al. (2017). A neuroprotective astrocyte state is induced by neuronal signal EphB1 but fails in ALS models. Nat. Commun. *8*, 1164.

Verderio, C., Coco, S., Pravettoni, E., Bacci, A., and Matteoli, M. (1999). Synaptogenesis in hippocampal cultures. Cell. Mol. Life Sci. C. *55*, 1448–1462.

Vihanto, M.M., Plock, J., Erni, D., Frey, B.M., Frey, F.J., and Huynh-Do, U. (2005). Hypoxia up-regulates expression of Eph receptors and ephrins in mouse skin. FASEB J. *19*, 1689–1691.

Waites, C.L., Craig, A.M., and Garner, C.C. (2005). Mechanisms of Vertebrate Synaptogenesis. 251–276.

Wang, Y.-F., and Parpura, V. (2016). Central Role of Maladapted Astrocytic Plasticity in Ischemic Brain Edema Formation. Front. Cell. Neurosci. *10*, 129.

Wang, C., Liu, M., Pan, Y., Bai, B., and Chen, J. (2017). Global gene expression profile of cerebral ischemia-reperfusion injury in rat MCAO model. Oncotarget *8*, 74607–74622.

Wang, Y., Nakayama, M., Pitulescu, M.E., Schmidt, T.S., Bochenek, M.L., Sakakibara, A., Adams, S., Davy, A., Deutsch, U., Lüthi, U., et al. (2010). Ephrin-B2 controls VEGF-induced angiogenesis and lymphangiogenesis. Nature *465*, 483–486.

Won, S.-J., Kim, D.-Y., and Gwag, B.-J. (2002). Cellular and Molecular Pathways of Ischemic Neuronal Death. J. Biochem. Mol. Biol. *35*, 67–86.

Xing, S., He, Y., Ling, L., Hou, Q., Yu, J., Zeng, J., and Pei, Z. (2008). Blockade of EphB2 enhances neurogenesis in the subventricular zone and improves neurological function after

cerebral cortical infarction in hypertensive rats. Brain Res. *1230*, 237–246.

Xiong, Y., Mahmood, A., and Chopp, M. (2010). Angiogenesis, neurogenesis and brain recovery of function following injury. Curr. Opin. Investig. Drugs *11*, 298–308.

Xu, Z., Lai, K.-O., Zhou, H.-M., Lin, S.-C., and Ip, N.Y. (2003). Ephrin-B1 reverse signaling activates JNK through a novel mechanism that is independent of tyrosine phosphorylation. J. Biol. Chem. *278*, 24767–24775.

Yan, G., Dai, Z., Xuan, Y., and Wu, R. (2015). Early metabolic changes following ischemia onset in rats: an in vivo diffusion-weighted imaging and 1H-magnetic resonance spectroscopy study at 7.0 T. Mol. Med. Rep. *11*, 4109–4114.

Yilmaz, G., and Granger, D.N. (2010). Leukocyte recruitment and ischemic brain injury. Neuromolecular Med. *12*, 193–204.

Yuferov, V., Ho, A., Morgello, S., Yang, Y., Ott, J., and Kreek, M.J. (2013). Expression of ephrin receptors and ligands in postmortem brains of HIV-infected subjects with and without cognitive impairment. J. Neuroimmune Pharmacol. *8*, 333–344.

Zhan, R.-Z., Wu, C., Fujihara, H., Taga, K., Qi, S., Naito, M., and Shimoji, K. (2001). Both Caspase-Dependent and Caspase-Independent Pathways May Be Involved in Hippocampal CA1 Neuronal Death Because of Loss of Cytochrome c from Mitochondria in a Rat Forebrain Ischemia Model. J. Cereb. Blood Flow Metab. *21*, 529–540.

Zhang, R.L., Zhang, Z.G., and Chopp, M. (2008). Ischemic stroke and neurogenesis in the subventricular zone. Neuropharmacology *55*, 345–352.

Zhang, S., Yao, Y., Shi, J., Tang, X., Zhao, L., and Zhu, W. (2016). The temporal evolution of diffusional kurtosis imaging in an experimental middle cerebral artery occlusion (MCAO) model. Magn. Reson. Imaging *34*, 889–895.

Zhou, L., Li, F., Xu, H.-B., Luo, C.-X., Wu, H.-Y., Zhu, M.-M., Lu, W., Ji, X., Zhou, Q.-G., and Zhu, D.-Y. (2010). Treatment of cerebral ischemia by disrupting ischemia-induced interaction of nNOS with PSD-95. Nat. Med. *16*, 1439–1443.

Zhou, X., Hollern, D., Liao, J., Andrechek, E., and Wang, H. (2013). NMDA receptor-mediated excitotoxicity depends on the coactivation of synaptic and extrasynaptic receptors. Cell Death Dis. *4*, e560.

8 Acknowledgement

First and foremost, I would like to thank Prof. Dr. Markus Hecker for giving me the opportunity to undertake my PhD study in the Institute of Physiology and Pathophysiology. I appreciate his support, guidance and time he spent to realize this project.

I would like to express my sincere gratitude to Prof. Dr. Thomas Korff, my direct thesis supervisor. Thank you for your support and mentorship, your advices and criticism, for helping me to learn the diverse and fascinating aspects about science, and maybe even more important, thank you for the trust and space you gave me to accomplish my research.

I also want to thank Prof. Dr. Hugo Marti for providing me the opportunity to join his team and who gave access to the laboratory as well as the whole AG Marti for welcoming me.

Besides my advisor, I would like to thank the rest of my thesis committee: Prof. Dr. Peter Angel, Dr. Carmen Ruiz de Almodóvar, and Prof. Dr. Hilmar Bading for their insightful comments and encouragement, but also for the hard questions which incented me to widen my research from various perspectives.

Special thanks go to our collaboration partners, Prof. Dr. Hilmar Bading and Dr. Anna M. Hertle, Dr. Angelika Hoffmann and Manuel Fischer, Dr. Carsten Sticht, Dr. Holger Lorenz, and. Dr. Dorde Komljenovic, who not only helped me to conduct experiments, but who spent also a lot of time and patience to support me. Further, I would like to thank Prof- Dr. Johannes Schenkel for providing me access to the facilities of the DKFZ:

Many thanks to Maria, Inge and Nadine for excellent technical support.

I thank my fellow labmates and colleagues at the institute, and especially the members of the AG Korff Anja, Caro, Eda, Hanna and Yvonne for all the pep talks and coffee breaks.

Thanks are also directed to Anja, Caro and my dear friend Hana for the time they spent for proofreading and critical revision.

During my PhD study, I had the fortune to meet many great persons, however, there is this one, special, lovely person who was much more than a colleague to me: Laura, without you there would never have been so much fun and so many happy hours in the lab, and I am deeply thankful for your support and help, for your solace and loyalty. But most of all thank you for your friendship (*Lab partner has no end*.).

Saving the most important for the last, I wish to give my heartfelt thanks to my dearest husband, Marcel, who is my rock and without his love, never ending encouragement and understanding it wouldn't have been possible. Marcel, you mean the world to me.